Nonadiabatic Dynamics with Spin-orbit couplings

THÈSE N^{O} 7439 (2017)

PRÉSENTÉE LE 24 FÉVRIER 2017

À LA FACULTÉ DES SCIENCES DE BASE
CENTRE EUROPÉEN DE CALCUL ATOMIQUE ET MOLÉCULAIRE
PROGRAMME DOCTORAL EN CHIMIE ET GÉNIE CHIMIQUE

ÉCOLE POLYTECHNIQUE FÉDÉRALE DE LAUSANNE

POUR L'OBTENTION DU GRADE DE DOCTEUR ÈS SCIENCES

PAR

Felipe MIRAGLIA FRANCO DE CARVALHO

acceptée sur proposition du jury:

Prof. L. Helm, président du jury
Prof. D. J. Tildesley, Dr I. Tavernelli, directeurs de thèse
Dr T. Penfold, rapporteur
Prof. J. Hutter, rapporteur
Prof. C. Corminboeuf, rapporteuse

ÉCOLE POLYTECHNIQUE
FÉDÉRALE DE LAUSANNE
Suisse
2017

Acknowledgements

I would like to thank Ivano Tavarnelli for giving my the opportunity to carry out this thesis work under his supervision. It is in great part because of his lectures on quantum chemistry and molecular dynamics that I decided to pursue a doctorate degree in this domain. In a world of specialists, he is one of the few people I know who understands and – perhaps more importantly – is truly interested in both physics and chemistry. He has been sharing this knowledge and his enthusiasm for science since the day I met him, and it has been a pleasure working with him.

I would also like to thank Basile Curchod, who also did his PhD under Ivano's supervision and who guided me through my first computational chemistry research projects. He is truly passionate about science, a great teacher and has an extraordinary work discipline. He went from being my supervisor to a true friend.

I started out my PhD project in the LCBC lab and I want to thank all of its members, in particular Karin Pasche who was always extremely helpful and kind. The second part of my PhD was carried out at CECAM, whose members welcomed to the lab with open arms. I would especially like to thank Dominic Tildesley, who became my thesis director and who has always been extremely kind. I would also like to thank Sara Bonella, for whom I was a teacher's assistant; an experience that made me learn great deal of physics. My thanks go to the CECAM staff as well: Catarina Merdonça, Nathalie Carminatti, Guy Byron Catherine Wannier, Bogdan Nichita and Marianne Robinson for their support. The post-docs Nick Miller, Alexander Muratov and Momir Mallis working at CECAM made feel at home on the second of floor of the lab. In particular, Nick Miller became a good friend of mine.

My life on campus was made very pleasurable thanks to many friends, especially Nick Browning, Elisa Liberatore (and later on, her son Matteo) and Gloria Capano, who also did me the great favor of proof-reading my thesis. I would like to thank my friends of the LPI lab who I had lunch with on a daily basis and with whom I had lots of fun over the past two years.

I cannot forget my "off-campus" friends: Lucius, Vivien, Dups, Marc, Céline, Lara, Yanouk, Maël, Basile, Cyril, Malik and Niko who I have been friends with for almost a decade (more for some) and who were always supportive while I was doing my thesis.

One of my favorite pastimes in the past few years were rock and mountain climbing, something I learned from or practiced with my friends Pascal Miéville, Manuel Dömer (the two people who taught me climbing), Davide Bertoldo (who taught me mountaineering) and Amandine Masson.

Last I want to thank my brother, my father and my mother simply for being a great family.

Acknowledgements

Felipe,
Lausanne, December 2016

Abstract

This thesis deals with the excited-states dynamics of molecules beyond the Bon-Oppenheimer approximation (nonadiabatic dynamics). The nuclei were always treated with classical mechanics while the electrons were treated quantum mechanically, using linear-response time-dependent density functional theory for the calculation of electronic excited states. The focus of the work is the treatment of intersystem crossing through the use of auxiliary wavefunctions to calculate spin-orbit coupling.
The text includes a review of the necessary theoretical concepts, an description of the method used to calculate spin-orbit coupling and applications to static calculations and dynamics simulations of small molecules and large carbon nanostructures.

Key words: TDDFT, nonadiabatic dynamics, intersystem crossing, spin-orbit coupling

Résumé

La présente thèse concerne la dynamique des molécules dans leurs états excités électroniques, au-delà de l'approximation de Born-Oppenheimer (dynamique non-adiabatique). Les noyaux des molécules sont toujours traités avec la mécanique classique et les électrons de façon quantique, en utilisant la théorie de la fonctionelle de la densité dépendente du temps pour le calcul des états éxcités électroniques. Le travail de recherche fut centré sur la description du phénomène de croisement intersystèmes en utilisant des fonctions d'onde auxiliaires pour le calcul du couplage spin-orbite.
Le texte comprend une révision des concepts théoriques nécessaires, un description de la méthode pour le calcul du couplage spin-orbite et des applications aux calculs statiques et des simulations de dynamique de petites molécules et de nanostructures de carbone.

Mots clefs : TDDFT, dynamique non-adiabatique, croisement intersystèmes , couplage spin-orbite

Contents

Note about the text

It is important that I make a few remarks about the text before starting. The first one concerns the style of the text, which may seem to go from very pedagogical to very specialized (and possibly obscure to non-specialists). Were it possible, I would have tried to make every step of every derivation explicit, starting from the most fundamental principles; and every term as well defined as possible. Unfortunately both my time and my understanding of the subjects required to achieve anything of the sort are limited, so I did what I could.

I think it all comes down to whom I am writing this for. Clearly I am writing this for whoever is interested in computational chemistry or molecular physics and for whoever wants (or has) to read this thesis. I think, however, that I am writing this thesis for myself as well. I hope that in the future, whenever I pick up this document, I can find in it whatever insights I managed to have during these four years of work, especially because I feel that in a lot of specialized texts authors tend to skip steps that seem to be obvious, but are not (they might be obvious to the authors themselves, but they sometimes are not to me). Clearly, what was an insight to me, might be trivial to others, and I think this might help to explain the inhomogeneity of the text.

The second remark is about the use of the pronoun "we". When I use it, I either mean the reader and myself, or the other people who did the work with me because, even though I was alone in writing the thesis itself, I certainly did not do all the required research alone. Moreover, chapters 3, 4 and 5 are part of work that has been, or will (hopefully) be published in the near future. In fact these chapters are modified versions of articles which were co-written with Ivano Tavernelli (chapters 3, 4 and 5) and Basile Curchod (3).

List of symbols and acronyms

0.1 Acronyms

LHS	left-hand side	
RHS	right-hand side	
IC	internal conversion	p. 2
ISC	intersystem crossing	p. 2
GS	ground-state	p. 2
SOC	spin-orbit coupling	p. 2
BO	Born-Oppenheimer	p. 3
LR-TDDFT	linear-response time-dependent density functional theory	p. 4
TISE	time-independent Schrödinger equation	p. 5
PES	potential energy surface	p. 9
SE	Schrödinger equation	p. 9
TDSE	time-dependent Schrödinger equation	p. 11
TSH	trajectory surface-hopping	p. 12
HF	Hartree-Fock	p. 15
CI	configuration interaction	p. 19
CC	coupled-cluster	p. 19
DFT	density functional theory	p. 19
HK	Hohenberg-Kohn	p. 20
TDF	Thomas-Dirac-Fermi	p. 23
KS	Kohn-Sham	p. 23
xc	exchange-correlation	p. 25
RG	Runge-Gross	p. 26
TDA	Tamm-Dancoff approximation	p. 33
LR	linear-reponse	p. 33
AMEW	auxiliary many-electron wavefunction	p. 33

List of Figures

List of Tables

1 Introduction

In a nutshell, chemistry is concerned with how atoms bind to each other to form molecules. These molecules make up virtually all matter that surrounds humans in their day-to-day lives. The particular way in which these atoms form bonds and how these molecules move around in space determine the properties of common matter, such as temperature, pressure, elasticity, friction, boiling point, just to name a few.

Theoretical and computational chemistry have the hefty goal of explaining these properties solely through the fundamental laws of physics (semiempirical methods notwithstanding). This particularly challenging because even though the laws that govern atoms and molecules have been known for at least a century – be them the laws of classical mechanics, thermodynamics or quantum mechanics – solving them for any realistic molecular system is extremely complicated. In fact, there are no exact solutions to these equations, and hence the obligatory use of computers to solve them numerically.

A particular class of properties of matter determined by the physics of atoms and molecules is its interaction with light, and the sciences that study this interaction are photophysics and photochemistry. Different kinds of atoms and molecules absorb and emit light of different frequencies – microwave, infrared, visible, UV and beyond – depending on how their energy levels are spaced, which is in turn determined by the laws of quantum mechanics, namely, Schrödinger's equation.

The photophysics and photochemistry of molecules influence human vision, the biology of cancer, climate science, solar-panel energy generation, lighting and literally hundreds of other domains. These sciences are therefore worth being studied, not only because they deal with fundamental physical phenomena – which is reason enough — but also because they underlie phenomena and technologies of importance to people in general (even to those not interested in chemistry or physics).

1.0.1 The processes of photochemistry

Even though the fundamental phenomena of molecular photophysics and photochemistry generate a world of complexity, they can be subdivided in two main categories, which can then be subdivided in only a few other categories.
The first broad category is that of **radiative phenomena**. These processes involve the direct interaction of light with atoms or molecules. If a molecule receives energy in the form of electromagnetic radiation (light), then the process is named **absorption**. The spacing between the energy levels of the molecule corresponds to the energy and to the frequency of the light absorbed through Planck's formula $E = h\nu$ where h is Planck's constant and ν is the frequency. **Emission** of light by the molecule is the opposite of absorption; the molecules gives up energy in the form of light. The frequency of the emitted light is also determined by the spacing between the energy levels of the molecule. Furthermore, emission is usually subdivided in two types; **fluorescence** and **phosphorescence**, depending on the type of energy levels which they involve. In fluorescence the two energy levels involved are of same spin-multiplicity (equivalently, the total spin), whereas in phosphorescence they are different.
The second main category of photophysical phenomena are the nonradiative phenomena. As the name suggests, these do not involve direct interaction of the molecule with light, but rather processes in which the molecule goes from one energy level to another, without the emission of radiation. The first type of nonradiative process is **internal conversion** (IC), in which there is no change of spin-multiplicity (just like fluorescence). The second type is **intersystem crossing**, in which there is change of spin-multiplicity (just like phosphorescence).
These processes are pictorially summarized in the Jablonski diagram, such as the one shown in Fig. 1.1, where GS stands for the ground-state of the molecule, S_1 is the first singlet (spin-multiplicity of 1) excited state and S_2 is the second one. T_1 is the first triplet state (spin-multiplicity of 3). These two spin-multiplicites are those commonly encountered in molecules with an even number of electrons (most molecules without transition metals).
GS, S_1, S_2 and T_1 are actually electronic states, as they correspond to the energy of the electrons, and they are represented by thick black lines. The thin grey lines represent the vibrational sublevels of the electronic states, and they arise because of nuclear motion in the presence of the electrons.The wavy arrows represent light and radiative processes - pink corresponding to absorption, green to fluorescence and blue to phosphorescence.
Phosphorescence and intersystem crossing –which involve a change of spin-multiplicity of the electronic state of the molecule – do not respect spectroscopic selection rules and as such they are termed "spin-forbidden" processes. These processes do occur however, because of a quantum relativistic effect called spin-orbit coupling (SOC). Thanks to these effects phospohrescence and ISC become "weakly-allowed", that is, they will be less likely to occur – or equivalently, they will be slower – than fluorescence and IC. The term "weakly-allowed" is relative however, since in certain molecules ISC and phosphorescence will compete with IC and fluorescence. This is especially likely in molecules with heavy atoms, which enhance spin-orbit coupling. Nonetheless, it is known that these effects, especially ISC, can be important even in very simple organic and inorganic molecules.

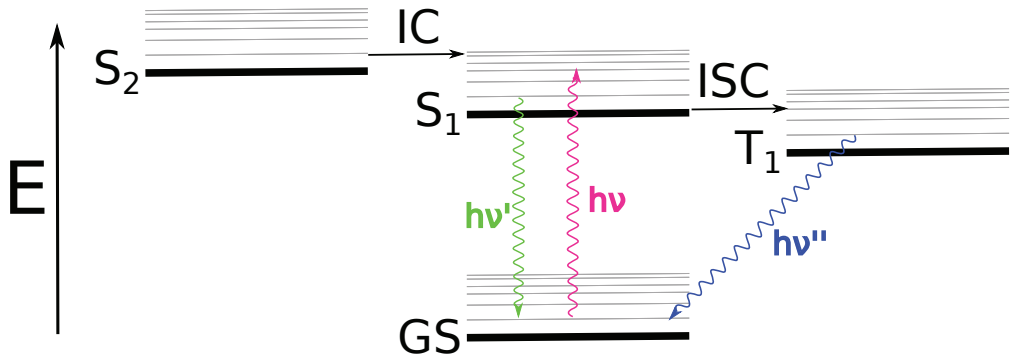

Figure 1.1 – Jablonski diagram.

Examples of the importance of spin-forbidden processes in chemistry and molecular physics abound. A theoretical study [1] has explored a possible mechanism for the base hydrolysis reaction of $Co(NH_3)_5Cl^{2+}$ (a ligand substitution reaction) involving the transition from a singlet state to a triplet state and then back to the singlet state.
ISC is also known to be important in the photochemistry of molecules containing a carbonyl group, since the reactivity of excited triplet states differs markedly from that of singlet states. Photochemical hydrogen abstraction reactions involving ketones, for example, often involve the particularly reactive triplet state, which can only be reached through intersystem crossing [2]. In fact, the triplet states of most molecules have in general different reactivity to that of singlet states and there is a technique in organic photochemistry, called "triplet sensitization", whose goal is to populate triplet states of molecules, so as to obtain different chemical reactions [2, 3].
Another use of SOC, is exemplified by the use of heavy-metal organometallic complexes in organic light-emitting diodes (OLEDs) to increase their efficiency through a process named "triplet-harvesting" [4, 5].

1.0.2 Object and structure of the thesis

This thesis is concerned with description of some of the phenomena in the Jablonski diagram. To be more precise, it will focus on the description of SOC and ISC. The nonradiative processes of photochemistry are (i) dynamical in nature, as they can only occur if the nuclei move in the presence of the electrons, and (ii) nonadiabatic because they go beyond the Born-Oppenheimer approximation (BO). This approximation, in which the electrons and the nuclei can be treated separately and in which the nuclei move in a "field" generated by the electrons, is both accurate and widely used in chemistry, but encounters its limits in excited state dynamics. In fact it would be more accurate to say that there are no electronic or nuclear energy levels, but only molecular levels that arise because of the inseparable interaction of nuclei and electrons. Nonetheless, the BO approximation will not be abandoned completely,

since the picture of the interaction between electrons and nuclei that it paints is very useful, and completely ingrained in the heads of chemists. In fact, the Jablosnki diagram is based on the BO approximation even though it depicts processes that go beyond it. This is possible because nonadiabatic effects are relatively small, and can be added *post-hoc* to the picture after the BO approximation has been used to calculate electronic energy levels.
The description of internal conversion will also be included, since this thesis builds on work that has already been done by Ivano Tavernelli and Basile Curchod to describe nonadiabatic effects other than spin-orbit coupling [6, 7, 8, 9].
The interaction with light will not be treated explicitly, but rather it will be assumed that a given molecule is in an excited state (as a consequence of its interaction with light). The method that will be used to calculate the excited states of molecules and its properties is linear-response time-dependent density functional theory (LR-TDDFT), which combines good accuracy with a relatively low computational cost.
The first chapter of this thesis is this general introduction, and it will be followed by a chapter on the theoretical concepts that are necessary for the understanding of the rest of the thesis. Some of these concepts have already been mentioned in this introduction, but will be described more precisely in chapter 2.
The three following chapters describe original research work done during this thesis, with the aim of describing SOC and ISC in the framework of LR-TDDFT. The results contained in the first two chapters have been published in peer-reviewed journals. The contents of the third will be submitted for publication very soon. The final, very brief chapter, contains a conclusion and a short discussion on the outlook of the research.

2 Theoretical Concepts

This chapter is a review of theoretical concepts that were important in the scientific research presented in this thesis. The main subjects approached in this chapter will be the Born-Oppenheimer approximation and nonadiabatic couplings, trajectory-based solutions of the time-dependent Schrödinger equation and spin-orbit coupling.
Atomic units will be used throughout the text, except when we wish to make the appearance of a certain constant explict (the reduced Planck's constant $\hbar$ or the fine-structure constant α might appear, for example).
Part of this chapter is based on Ref. [10]. It also draws inspiration from Ivano Tavernelli's lecture on computational chemistry, which used to be given in EPFL's chemistry Master's program. Most of my knowledge of quantum mechanics comes from Refs. [11, 12].

2.1 Molecular Hamiltonians and the Born-Oppenheimer approximation

2.1.1 The molecular Hamiltonian

The time-independent Schrödinger equation (TISE) is

$$\hat{H}|\Psi\rangle = E|\Psi\rangle \,. \tag{2.1}$$

Here E is the energy of the system, $|\Psi\rangle$ is its state and $\hat{H}$ is the Hamiltonian operator that describes it.The state $|\Psi\rangle$ vectors belong to a Hilbert space that we will refer to as the state space. All operators – such as $\hat{H}$ – that we will deal with map a state vector $|\Psi\rangle$ to another state vector $|\Phi\rangle$ and are linear.

In the case of the hydrogen atom, composed of a proton and an electron, the Hamiltonian is:

$$\hat{H} = \frac{1}{2m_p}\hat{\mathbf{P}}^2 + \frac{1}{2m_e}\hat{\mathbf{p}}^2 + \hat{V}(\mathbf{R},\mathbf{r})\,, \tag{2.2}$$

where $\hat{\mathbf{R}}$ and $\hat{\mathbf{r}}$ are three-dimensional vector operators that represent the positions of the proton and the electron, respectively; $\hat{\mathbf{P}}$ and $\hat{\mathbf{p}}$ are the momenta and m_p and are m_e the masses. In the position representation the potential energy $\hat{V}(\hat{\mathbf{R}},\hat{\mathbf{r}})$) is the attractive Coulomb potential

$$\hat{V}(\hat{\mathbf{R}},\hat{\mathbf{r}}) = \hat{V}(\hat{\mathbf{R}}-\hat{\mathbf{r}}) = \frac{-1}{||\hat{\mathbf{R}}-\hat{\mathbf{r}}||}\,, \tag{2.3}$$

and we can see that it is only a function of the distance between the proton and the electron. Thus, if we let $\hat{\mathbf{r}} = \hat{\mathbf{R}} - \hat{\mathbf{r}}_e$ and $\hat{\mathbf{R}}_{COM} = \frac{m_e\hat{\mathbf{r}}+m_p\hat{\mathbf{R}}}{m_e+m_p}$, the Hamiltonian can be re-written as

$$\hat{H} = \frac{1}{2(m_e+m_p)}\hat{\mathbf{P}}^2_{COM} + \frac{1}{2\mu}\hat{\mathbf{p}}^2 + \hat{V}(\hat{\mathbf{r}})\,. \tag{2.4}$$

Furthermore, if we place ourselves in the center-of-mass frame of reference, the first term on the right-hand side of Eq. (2.4) is zero and we obtain

$$\hat{H} = \frac{1}{2\mu}\hat{\mathbf{p}}^2 + \hat{V}(\hat{\mathbf{r}})\,, \tag{2.5}$$

In the position representation the Hamiltonian reads

$$H = \frac{1}{2\mu}\nabla^2_{\mathbf{r}} + V(\mathbf{r})\,, \tag{2.6}$$

where the position operators are now simple three-dimensional vectors, $V(\mathbf{r})$ is a now a function of $\mathbf{r}$, the state vector $|\Psi(\boldsymbol{r})\rangle$ becomes a wavefunction $\Psi(\boldsymbol{r})$ and $\nabla^2_{\mathbf{r}}$ is the laplacian operator with respect to $\boldsymbol{r}$.
In Eqns. (2.5) and (2.6) $\mu = \frac{m_p m_e}{m_p+m_e}$ is the reduced mass. Since the proton has a mass much larger than that of the electron ($m_p/m_e \approx 1836$), the center-of-mass is practically on top of the proton and $\mathbf{r}$ is practically the position of the electron. For this reason $\mathbf{r}$ is usually referred to

as the position of the electron and μ is replaced by m_e.
We have therefore reduced a two-body problem to the problem of a particle in a central potential and the Schrödinger equation can now be solved analytically.
In chemistry, however, we are usually interested in molecules, and the general form of the molecular Hamiltonian is:

$$\begin{aligned}\hat{H} &= \sum_{\gamma}^{N_n} \frac{\hat{\mathbf{P}}_\gamma^2}{2M_\gamma} + \sum_{i}^{N_{el}} \frac{\hat{\mathbf{p}}_i^2}{2m_e} + \sum_{i}^{N_{el}}\sum_{j}^{N_{el}} \frac{1}{||\hat{\mathbf{r}}_j - \hat{\mathbf{r}}_j||} - \sum_{\gamma}^{N_n}\sum_{i}^{N_{el}} \frac{Z_\gamma}{||\hat{\mathbf{R}}_\gamma - \hat{\mathbf{r}}_i||} + \sum_{\gamma}^{N_n}\sum_{\zeta}^{N_n} \frac{Z_\gamma Z_\zeta}{||\hat{\mathbf{R}}_\gamma - \hat{\mathbf{R}}_\zeta||} \\ &= \hat{T}_\mathrm{n} + \hat{T}_\mathrm{e} + V_\mathrm{e-e} + V_\mathrm{e-n} + V_\mathrm{n-n}\,,\end{aligned} \tag{2.7}$$

where the last three terms on the RHS of (2.7) are the electron-electron, nucleus-nucleus and nucleus-electron potential energy term, respectively. Because of the extra potential energy term V_{e-e}, the Hamiltonian is not separable and the SE cannot be solved analytically anymore. In order to (numerically) solve the SE with the Hamiltonian (2.7) it is necessary to make several approximations. Arguably, the most important of these approximations is the Born-Oppenheimer approximation, which will be explored in further detail in the next section.

2.1.2 The Born-Oppenheimer approximation

In order to obtain the molecular Schrödinger equation with the Born-Oppenheimer approximation we will start with the Born-Huang ansatz for the molecular wavefunction. This is not the original approach of Born and Oppenheimer, however it is simpler. The Born-Huang ansatz is:

$$\Psi(\mathbf{r}_e, \mathbf{R}) = \sum_{I}^{+\infty} \Omega_I(\mathbf{R})\psi_I(\mathbf{r}_e; \mathbf{R})\,, \tag{2.8}$$

where $\Psi(\mathbf{r}_e, \mathbf{R})$ is the molecular wavefunction, $\psi_I(\mathbf{r}_e; \mathbf{R})$ are the electronic wavefunctions and $\Omega_I(\mathbf{R})$ are $\mathbf{R}$-dependent coefficients. What we have done is develop $\Psi(\mathbf{r}_e, \mathbf{R})$ in terms of the eigenstates of the electronic Hamiltonian $\hat{H}_{el}$

$$\hat{H}_{el} = \hat{T}_\mathrm{e} + V_\mathrm{e-e} + V_\mathrm{e-n} + V_\mathrm{n-n} \tag{2.9}$$

which includes every term in $\hat{H}$ except for the nuclear kinetic energy. We know that the $\psi_I(\mathbf{r}_e; \mathbf{R})$ form a complete basis for the electronic degrees of freedom $\mathbf{r_e}$, at least at a fixed

position **R** for the nuclei. The idea is that for each value of **R** we can develop the molecular wavefunction in the form shown in Eq. (2.8). This means that the electronic wavefunctions will depend on the parameter **R**, and this parametric dependence is indicated by the semicolon in $\psi_I(\mathbf{r}_e;\mathbf{R})$. Despite **R**-dependence of $\psi_I(\mathbf{r}_e;\mathbf{R})$, they do not form a complete basis for the nuclear degrees of freedom, so the coefficients $\Omega_I(\mathbf{R})$ must depend on **R** as well. Notice that we have also included the nucleus-to-nucleus Coulomb potential in the definition of $\hat{H}_{el}$; we can this because we have fixed the nuclear positions and $V_{\mathrm{n-n}}$ is then a constant (and will modify the states $\{\psi_I(\mathbf{r}_e;\mathbf{R})\}$ only up to a complex phase).
The physical motivation for fixing the nuclear positions is the fact that electrons are much lighter than nuclei. Notice however, that there have been no approximations up to this point and we could have chosen to fix the positions of the electrons instead of those of the nuclei; this possibility has in fact, been recently explored by Abedi *et al.*. [13, 14].

The next step in obtaining the BO approximation is to insert the RHS of (2.8) into the molecular Schrödinger equation,

$$\begin{aligned}\hat{H}\sum_I^{+\infty}\Omega_I(\mathbf{R})\psi_I(\mathbf{r}_e;\mathbf{R}) &= E\sum_I^{+\infty}\Omega_I(\mathbf{R})\psi_I(\mathbf{r}_e;\mathbf{R}) \\ =\sum_I^{+\infty}(\hat{T}_{\mathrm{n}}+\hat{H}_{el})\Omega_I(\mathbf{R})\psi_I(\mathbf{r}_e;\mathbf{R}) &= E\sum_I^{+\infty}\Omega_I(\mathbf{R})\psi_I(\mathbf{r}_e;\mathbf{R})\end{aligned} \tag{2.10}$$

and the multiply from the left by $\psi_J^*(\mathbf{r}_e;\mathbf{R})$ and integrate over the electronic coordinates **r**. We obtain

$$\left[\sum_I^{+\infty}\int d\mathbf{r}\,\psi_J^*(\mathbf{r}_e;\mathbf{R})\,\hat{T}_{\mathrm{n}}\Omega_I(\mathbf{R})\psi_I(\mathbf{r}_e;\mathbf{R})\right]+\epsilon_J(\mathbf{R})\Omega_J(\mathbf{R}) = E\Omega_J(\mathbf{R})\,, \tag{2.11}$$

where $\epsilon_J(\mathbf{R})$ is the J^{th} eigenvalue of $\hat{H}_{el}$, that is to say, the electronic energy of the J^{th} electronic state, which has a parametric dependence on **R** since we have only integrated over $\boldsymbol{r}_e$.
If we take a closer look at the term in brackets on the LHS of the previous equation, and write out the explicit form of the nuclear kinetic energy operator

$$\hat{T}_{\mathrm{n}} = \sum_\gamma^{N_n}\frac{\hat{\mathbf{P}}_\gamma^2}{2M_\gamma} = \sum_\gamma^{N_n}\frac{\nabla_\gamma^2}{2M_\gamma}\,, \tag{2.12}$$

we notice that we can use the vector calculus identity

$$\nabla^2(\Omega\psi) = \Omega\nabla^2\psi + 2\nabla\Omega\cdot\nabla\psi + \psi\nabla^2\Omega \tag{2.13}$$

in Eq. (2.11) to obtain

$$\begin{aligned}
&\left[\sum_I^{+\infty}\sum_\gamma^{N_n}\frac{1}{2M_\gamma}\int d\mathbf{r}\,\psi_J^*(\mathbf{r}_e;\mathbf{R})\nabla_\gamma^2\left(\Omega_I(\mathbf{R})\psi_I(\mathbf{r}_e;\mathbf{R})\right)\right] + \epsilon_J(\mathbf{R})\Omega_J(\mathbf{R}) \\
&= \left[\sum_I^{+\infty}\sum_\gamma^{N_n}\frac{1}{2M_\gamma}\int d\mathbf{r}\,\psi_J^*(\mathbf{r}_e;\mathbf{R})\big(\Omega_I(\mathbf{R})\nabla_\gamma^2\psi_I(\mathbf{r}_e;\mathbf{R}) + \right. \\
&\left. 2\nabla_\gamma\Omega_I(\mathbf{R})\cdot\nabla_\gamma\psi_I(\mathbf{r}_e;\mathbf{R}) + \psi_I(\mathbf{r}_e;\mathbf{R})\nabla_\gamma^2\Omega_I(\mathbf{R})\big)\right] + \epsilon_J(\mathbf{R})\Omega_J(\mathbf{R}) \\
&= \left[\sum_I^{+\infty}\sum_\gamma^{N_n}\frac{1}{2M_\gamma}\int d\mathbf{r}\,\psi_J^*(\mathbf{r}_e;\mathbf{R})\big(\Omega_I(\mathbf{R})\nabla_\gamma^2\psi_I(\mathbf{r}_e;\mathbf{R}) + \right. \\
&\left. 2\nabla_\gamma\Omega_I(\mathbf{R})\cdot\nabla_\gamma\psi_I(\mathbf{r}_e;\mathbf{R}) + \psi_I(\mathbf{r}_e;\mathbf{R})\nabla_\gamma^2\Omega_I(\mathbf{R})\big)\right] + \\
&\left[\sum_I^{+\infty}\delta_{IJ}\left(\sum_\gamma^{N_n}\frac{1}{2M_\gamma}\nabla_\gamma^2\Omega_I(\mathbf{R})\right)\right] + \epsilon_J(\mathbf{R})\Omega_J(\mathbf{R}) = E\Omega_J(\mathbf{R})\,,
\end{aligned} \tag{2.14}$$

which we write as

$$\left[\sum_I^{+\infty}\mathscr{F}_{JI}\Omega_I(\mathbf{R})\right] + \left(\hat{T}_\mathrm{n} + \epsilon_J(\mathbf{R})\right)\Omega_J(\mathbf{R}) = E\Omega_J(\mathbf{R})\,. \tag{2.15}$$

The terms $\mathscr{F}_{JI}$ are elements of what is called the nonadiabatic coupling matrix. By inspecting Eq. (2.15) we can see that if the $\mathscr{F}_{JI}$ are all zero then Eq. (2.15) becomes the Schrödinger equation

$$\left(\hat{T}_\mathrm{n} + \epsilon_J(\mathbf{R})\right)\Omega_J(\mathbf{R}) = E\Omega_J(\mathbf{R})\,. \tag{2.16}$$

The Hamiltonian for this SE comprises the nuclear kinetic energy operator and a function of the nuclear coordinates $\mathbf{R}$, and it is interpreted as being the nuclear Schrödinger equation, with $\Omega_J(\mathbf{R})$ the nuclear wavefunctions. $\epsilon_J(\mathbf{R})$ plays the role of the potential energy acting on the nuclei (it includes internuclear repulsion) and is called the potential energy surface (PES).

The Born-Oppenheimer approximation simply constitutes in setting the elements $\mathscr{F}_{JI}$ to zero. In other words, the molecular Schrödinger equation can be separated into the electronic SE and the nuclear SE

$$\begin{cases} \hat{H}_{el}\psi_J(\mathbf{r}_e;\mathbf{R}) = \epsilon_J(\mathbf{R})\psi_J(\mathbf{r}_e;\mathbf{R}) & (2.17) \\ \hat{H}_n\Omega(\mathbf{R}) = E\Omega(\mathbf{R})\,. & (2.18) \end{cases}$$

Equations (2.17) and (2.18) are connected via the term $\epsilon(\mathbf{R})$ which is simultaneously the eigenvalue of H_{el}, obtained by solving Eq. (2.17), and the potential energy term in the nuclear Hamiltonian $\hat{H}_n = \left(\hat{T}_\mathrm{n} + \epsilon(\mathbf{R})\right)$. If we multiply Eq. (2.17) by $\Omega(\mathbf{R})$ and Eq. (2.18) by $\psi_J(\mathbf{r}_e;\mathbf{R})$ from the right, then add the two resulting equations we obtain

$$\left(\hat{H}_n + \hat{H}_{el}\right)\Omega(\boldsymbol{R})\psi_J(\boldsymbol{r}_e;\boldsymbol{R}) = \left(E + \epsilon_J(\boldsymbol{R})\right)\Omega(\mathbf{R})\psi_J(\mathbf{r}_e;\mathbf{R})\,, \tag{2.19}$$

we then subtract $\epsilon_J(\boldsymbol{R})\Omega(\mathbf{R})\psi_J(\mathbf{r}_e;\mathbf{R})$ from both sides to obtain

$$\left(\hat{T}_n + \hat{H}_{el}\right)\Omega(\mathbf{R})\psi_J(\mathbf{r}_e;\mathbf{R}) = E\Omega(\mathbf{R})\psi_J(\mathbf{r}_e;\mathbf{R})\,, \tag{2.20}$$

which can be re-written as

$$\hat{H}\Psi(\mathbf{r}_e,\mathbf{R}) = E\Psi(\mathbf{r}_e,\mathbf{R})\,. \tag{2.21}$$

In the above equation we have recovered a molecular SE in which the molecular wavefunction is a simple product of a nuclear wavefunction with an electronic wavefunction.

How can the nonadiabatic coupling matrix $\mathscr{F}$ be interpreted if we do not set all its elements to zero? We see that its elements act on the nuclear wavefunction $\Omega_I(\mathbf{R})$

$$\mathscr{F}_{JI}\Omega_I(\mathbf{R}) = -\hbar^2 \sum_{\gamma}^{N_n} \frac{1}{2M_\gamma} \int d\mathbf{r}\, \psi_I^*(\mathbf{r}_e;\mathbf{R}) \left[2\nabla_\gamma \Omega_J(\mathbf{R}) \cdot \nabla_\gamma \psi_J(\mathbf{r}_e;\mathbf{R}) + \Omega_I(\mathbf{R}) \nabla_\gamma^2 \psi_J(\mathbf{r}_e;\mathbf{R}) \right] \Omega_I(\mathbf{R}) \tag{2.22}$$

$$= \left\{ \int d\mathbf{r}\, \psi_I^*(\mathbf{r}_e;\mathbf{R}) \left[-\sum_{\gamma}^{N_n} \frac{\hbar^2}{2M_\gamma} \nabla_\gamma^2 \right] \psi_J(\mathbf{r}_e;\mathbf{R}) \right.$$
$$\left. + \sum_{\gamma}^{N_n} \frac{1}{M_\gamma} \left\{ \int d\mathbf{r}\, \psi_I^*(\mathbf{r}_e;\mathbf{R}) \left[-i\hbar\nabla_\gamma \right] \psi_J(\mathbf{r}_e;\mathbf{R}) \right\} \cdot \left[-i\hbar\nabla_\gamma \right] \right\} \Omega_I(\mathbf{R}) \,,$$

and couple different electronic states (I and J) depending on the values of $\boldsymbol{R}$. If the $\mathscr{F}_{JI}$ are not all zero, then the molecular wavefunction of Eq. (2.8) will have more than one nonzero term in the sum. Since the expansion is made in terms of the electronic states $\psi_I(\mathbf{r}_e;\mathbf{R})$, more than one $\psi_I(\mathbf{r}_e;\mathbf{R})$ will contribute to the total wavefunction. Moreover, since the coefficients $\Omega_I(\boldsymbol{R})$ for each electronic state I are functions of $\boldsymbol{R}$, the molecular geometry will determine which electronic states contribute the most to the total molecular wavefunction.
For example, picture a system with only the ground state $\psi_0(\mathbf{r}_e;\mathbf{R})$ and a first excited state $\psi_1(\mathbf{r}_e;\mathbf{R})$, and that the $\psi_I(\mathbf{r}_e;\mathbf{R})$ for two states are known for every possible value of $\boldsymbol{R}$. The molecular wavefunction would then be given by

$$\Psi(\mathbf{r}_e,\mathbf{R}) = \Omega_0(\mathbf{R})\psi_0(\mathbf{r}_e;\mathbf{R}) + \Omega_1(\mathbf{R})\psi_1(\mathbf{r}_e;\mathbf{R}) \,, \tag{2.23}$$

and the $\Omega_I(\mathbf{R})$ would be determined by the system of equations

$$\begin{cases} \mathscr{F}_{00}(\boldsymbol{R})\Omega_0(\boldsymbol{R}) + \mathscr{F}_{01}(\boldsymbol{R})\Omega_1(\boldsymbol{R}) + \left(\hat{T}_\mathrm{n} + \epsilon_0(\mathbf{R})\right)\Omega_0(\mathbf{R}) = E\Omega_0(\mathbf{R}) \\ \mathscr{F}_{10}(\boldsymbol{R})\Omega_0(\boldsymbol{R}) + \mathscr{F}_{11}(\boldsymbol{R})\Omega_1(\boldsymbol{R}) + \left(\hat{T}_\mathrm{n} + \epsilon_1(\mathbf{R})\right)\Omega_1(\mathbf{R}) = E\Omega_1(\mathbf{R}) \,. \end{cases} \tag{2.24}$$

First of all we notice that the matrix $\mathscr{F}$ has diagonal terms which can induce an isotopic shift in the electronic energy [15, 16]. The non-diagonal terms, however, are more interesting. If we imagine that the system is in the ground-state, with a value of $\boldsymbol{R}$ for which the non-diagonal terms of $\mathscr{F}$ are negligible. The BO picture is then valid, and the total wavefunction is only $\Omega_0(\mathbf{R})\psi_0(\mathbf{r}_e;\mathbf{R})$. If we then imagine that the molecule starts moving along a direction of the nuclear configuration space in which elements $\mathscr{F}_{01}(\boldsymbol{R})$ and $\mathscr{F}_{10}(\boldsymbol{R})$ increase, then the states start to mix, due to the form of Eq. (2.24), and the BO approximation starts to break down. At this point, which electronic state is the molecule in? Different ways of approaching this question lead to different approximate nonadiabatic dynamics methods, such as Born-Oppenheimer dynamics [17], surface hopping dynamics [17, 18, 19] and Ehrenfest dynamics [17, 18, 19]. We

will see the former two in more detail in the next section.

2.2 Molecular Dynamics

In the previous section we discussed the Born-Oppenheimer approximation and the separation of the molecular Schrödinger equation into the electronic and nuclear equation (separate, but connected through the potential energy surface).
Now that this is done, a couple of remarks are in order. The first one is that we only talked about the time-independent SEs, but the word dynamics implies that an equation of motion should have appeared; the time-dependent Schrödinger equation (TDSE). We know, however, that in quantum mechanics the TISE and the TDSE are two sides of the same problem (although the TDSE is indeed more general than the TISE). This is because once we have solved the TISE, we can expand the time-dependent wavefunction $|\Psi(t)\rangle$ (the solution to the TDSE) into term of the eigenstates of the TISE,

$$|\Psi(t)\rangle = \sum_{I}^{+\infty} C_I(t)|\psi_I\rangle \,. \tag{2.25}$$

Given a set of initial conditions (the values of $C_I(0)$), there are several methods to integrate the TDSE and find the $C_I(t)$. We will not discuss these methods here, but what is important is that solving the TISE is a necessary step in solving the TDSE. More information on the methods used to integrate the TDSE can be found in references [20, 21].
The second remark is that in most molecular dynamics methods, the nuclei are assumed to behave classically. This is because they are relatively massive particles, and Newton's equations can describe their movement accurately. We therefore use Newton's equations to describe the movement of the nuclei and the SE to describe the electrons, which are too small to be described classically:

$$\begin{cases} \hat{H}_{el}\psi(\mathbf{r}_e;\mathbf{R}) = \epsilon(\mathbf{R})\psi(\mathbf{r}_e;\mathbf{R}) & (2.26) \\ M_\gamma \dfrac{d^2\mathbf{R}_\gamma}{dt^2} = -\nabla_\gamma \epsilon_I(\mathbf{R}) \,. & (2.27) \end{cases}$$

Where we have replaced the nuclear SE by Newton's equation of motion, but kept the electronic SE. This is called the *quantum classical approximation* or *semiclassical approximation*[1].
Notice that the forces $\mathbf{F}_\gamma = -\nabla_\gamma \epsilon_I(\mathbf{R})$ acting on the nuclei are derived from the potential energy surface of a particular electronic state I. These forces are evaluated numerically (using finite differences) or, if possible analytically, through the Hellman-Feynmann theorem [17, 22, 23].

[1] The term *semiclassical* can have different, very specific meanings in different contexts.

Equations (2.26) and (2.27) are the essence of the Born-Oppenheimer molecular dynamics method, in which one starts by solving (2.26). This equation can be solved by one of several different *electronic structure methods*, be they wavefunction methods such as Hartree-Fock or Configuration Interaction, or by Density Functional Theory methods. Once the electronic part of the problem is solved, the classical equation of motion (2.27) is then integrated for on time-step, usually with the velocity Verlet algorithm, and the nuclei are made to move in the direction of $\mathbf{F}_\gamma$. These steps are repeated until the desired total propagation time is reached. One important characteristic of this method is that the forces are determined by a single potential energy surface $\epsilon_I(\mathbf{R})$ since nonadiabatic couplings are not taken into account.

2.2.1 The Trajectory Surface Hopping method

As we stated in the last section, Born-Oppenheimer dynamics does not include nonadiabatic effects, and is thus confined to a single potential energy surface. In order to include nonadiabatic effects in the dynamics we turn to the surface hopping method, more specifically to Tully's surface hopping (TSH) [24, 25]. There are several other nondiabatic molecular dynamics methods, but TSH is arguably the most successful, and the only one we used in this work. The main idea behind TSH and any other surface hopping method is to have the classically described nuclei 'hop' from one potential energy surface to another, depending on the strength of the nondiabatic couplings and therefore the nuclear configuration. If several trajectories are run, then it is possible to collect statistics about the populations on different electronic states during the dynamics, so as to simulate the evolution of a nuclear wavepacket. However, the population of different electronic states is the only quantum nuclear effect included in surface hopping methods and they do not replace a full quantum dynamics simulation.
The different types of surface hopping differ in the way in which the trajectory is made to hop and we will go into the details of how Tully's surface hopping works. In his paper, Tully starts by remarking that if the motion of the nuclei are described by a trajectory $\boldsymbol{R}(t)$, then the electronic wavefunction $|\psi(\boldsymbol{r}_e;\boldsymbol{R})\rangle$ is also time-dependent, since it depends parametrically on $\boldsymbol{R}$. The electronic wavefunction is then expressed as

$$|\psi(\boldsymbol{r}_e, t;\boldsymbol{R})\rangle = \sum_i^\infty C_I(t)|\varphi_I(\boldsymbol{r}_e;\boldsymbol{R})\rangle \,, \tag{2.28}$$

where the $C_I(t)$ are time-dependent, complex-valued expansion coefficients and the $|\varphi_I(\boldsymbol{r}_e;\boldsymbol{R})\rangle$ are a complete orthonormal basis set for the electronic degrees of freedom $\boldsymbol{r}$. If we now insert

(2.28) into the TDSE, multiply by $\langle\varphi_J(\boldsymbol{r}_e;\boldsymbol{R})|$ (integrating only over $\boldsymbol{r}_e$) we obtain

$$i\hbar\dot{C}_J(t) = \sum_I^{\infty} C_I(t)\left(H_{JI}(\boldsymbol{R}) - i\hbar\sum_{\gamma}^{N_n}\boldsymbol{d}_{JI}^{\gamma}(\boldsymbol{R})\cdot\dot{\boldsymbol{R}}_{\gamma}\right). \tag{2.29}$$

In the above equation, $\boldsymbol{d}_{JI}^{\gamma}(\boldsymbol{R}) = \int d\boldsymbol{r}\,\varphi_J^*(\boldsymbol{r};\boldsymbol{R})\nabla_{\gamma}\varphi_I(\boldsymbol{r};\boldsymbol{R})$ are the nonadiabatic coupling vectors appearing in the last term of Eq. (2.22). Notice that in Eq. (2.22) there is a dot product between the $\boldsymbol{d}_{JI}^{\gamma}(\boldsymbol{R})$ and the operator $\left[-i\hbar\nabla_{\gamma}\right]$. In Eq. (2.29), the dot product is between $\boldsymbol{d}_{JI}^{\gamma}(\boldsymbol{R})$ and $\dot{\boldsymbol{R}}(t)$. This is because the nuclei are now treated classically. One can see that to get to Eq. (2.29) it is necessary to use the correspondence principle

$$\mathbf{P}_{\gamma} \rightarrow -i\hbar\frac{\nabla_{\gamma}}{M_{\gamma}}, \tag{2.30}$$

and interpret $|\Omega_i(\mathbf{R})|^2$ as being proportional to the quantum mechanical probability of finding the nuclei at position $\mathbf{R}$. By taking the classical limit one can then arrive at Eq. (2.29). This is just a sketch on how to get to Eq. (2.29) and for more details on this see Refs. [17, 26].
The term $H_{JI}(\boldsymbol{R})$ in Eq. (2.29) is the matrix element

$$H_{JI}(\boldsymbol{R}) = \langle\varphi_J(\boldsymbol{r}_e;\boldsymbol{R})|\hat{H}_{el}|\varphi_I(\boldsymbol{r}_e;\boldsymbol{R})\rangle, \tag{2.31}$$

resulting from the integration over $\boldsymbol{r}_e$. The probability $p_{JI}(t, t+dt)$ for the trajectory $\boldsymbol{R}(t)$ to jump from state J to state I during the time interval $[t, t+dt]$ is given by:

$$p_{KI}(t, t+\delta t) = -2\int_t^{t+\delta t}\frac{Re\left[C_J(\tau)C_I^*(\tau)\Xi_{JI}(\tau)\right] - Im\left[C_J(\tau)C^*(\tau)_I H_{IJ}\right]}{C_I(\tau)C_I^*(\tau)}d\tau\,. \tag{2.32}$$

where

$$\Xi_{IJ}(\tau) = \sum_{\gamma}^{N_n}\boldsymbol{d}_{IJ}^{\gamma}(\boldsymbol{R})\cdot\dot{\boldsymbol{R}}_{\gamma}\,. \tag{2.33}$$

If the basis set used to express $H_{JI}(\boldsymbol{R})$ are the eigenvectors of $\hat{H}_{el}$ (called the adiabatic basis),

then Eq. (2.29) becomes

$$i\hbar\dot{C}_J(t) = \sum_I^{\infty} C_I(t)\left(\epsilon_J(\boldsymbol{R}) - i\hbar\sum_{\gamma}^{N_n} \boldsymbol{d}_{JI}^{\gamma}(\boldsymbol{R})\cdot\dot{\boldsymbol{R}}_{\gamma}\right). \tag{2.34}$$

These coupled equations will be solved along a classical trajectory evolving *adiabatically* in a given electronic state J. The probability p_{JI} now becomes

$$p_{JI}(t, t+\delta t) = 2\int_t^{t+\delta t} d\tau \frac{-Re[C_i(\tau)C_J^*(\tau)\Xi_{IJ}(\tau)]}{C_J(\tau)C_J^*(\tau)}, \tag{2.35}$$

The algorithm also generates a random number $\zeta \in [0,1]$, and the hop occurs only if:

$$\sum_{k\leq I-1} p_{JK} < \zeta < \sum_{K\leq I} p_{JK}\,. \tag{2.36}$$

this guarantees that a minimum amount of hops is performed for each trajectory. For this reason it is also referred to as the "fewest switches" algorithm.

2.3 The electronic energy

2.3.1 A short description of the Hartree-Fock approximation.

In the previous sections we discussed molecular dynamics without making any specific mention on how to obtain the electronic energies $\epsilon_I(\boldsymbol{R})$. There are several electronic structure methods to do this, the most basic of which is Hartree-Fock (HF) theory.
The main approximation behind this theory is that the electronic wavefunction $|\psi\rangle$ is assumed to be a Slater determinant $|\upsilon_1\cdots\upsilon_{N_{el}}\rangle$, whose columns and rows are single-electron wavefunctions $\upsilon_i(\boldsymbol{x}_i)$. These single-electron wavefunctions are spin-orbitals or spinors, depending on the context, as they depend on both spatial and spin angular momentum degrees of freedom:

$$\upsilon_i(\boldsymbol{x}_i) = \varphi_{i\alpha}(\boldsymbol{r}_i)\alpha(\boldsymbol{s}_i) + \varphi_{i\beta}(\boldsymbol{r}_i)\beta(\boldsymbol{s}_i) \tag{2.37}$$

where $\boldsymbol{x}_i = (\boldsymbol{r}_i, \boldsymbol{s}_i)$ represents a collective variable for the spatial and spin degrees of freedom

of electron i. Alternatively v_i can be written as a two-component spinor in the $\{\alpha, \beta\}$ basis:

$$v_i(\boldsymbol{r}_i) = \begin{pmatrix} \varphi_{i\alpha}(\boldsymbol{r}_i) \\ \varphi_{i\beta}(\boldsymbol{r}_i) \end{pmatrix}. \tag{2.38}$$

Notice that in the above equation we have dropped the dependence on $\boldsymbol{s}$ because $\boldsymbol{s}$ has no real physical meaning and is used solely to represent the scalar products

$$\begin{aligned} \langle\alpha|\alpha\rangle &= \int d\boldsymbol{s}\alpha(\boldsymbol{s})\alpha(\boldsymbol{s}) = 1 \\ \langle\beta|\beta\rangle &= \int d\boldsymbol{s}\beta(\boldsymbol{s})\beta(\boldsymbol{s}) = 1 \\ \langle\alpha|\beta\rangle &= \langle\beta|\alpha\rangle = \int d\boldsymbol{s}\alpha(\boldsymbol{s})\beta(\boldsymbol{s}) = 0\,. \end{aligned} \tag{2.39}$$

Both α and β are eigenvectors of the spin operators $\hat{S}_i^2$:

$$\hat{S}_i^2\alpha(\boldsymbol{s}_i) = \frac{3}{4}\hbar^2\alpha(\boldsymbol{s}_i)\,, \tag{2.40}$$

$$\hat{S}_i^2\beta(\boldsymbol{s}_i) = \frac{3}{4}\hbar^2\beta(\boldsymbol{s}_i)\,, \tag{2.41}$$

and of the the projection of the spin angular momentum on the z-axis S_z:

$$\hat{S}_{iz}\alpha(\boldsymbol{s}_i) = \frac{\hbar}{2}\alpha(\boldsymbol{s}_i)\,, \tag{2.42}$$

$$\hat{S}_{iz}\beta(\boldsymbol{s}_i) = -\frac{\hbar}{2}\beta(\boldsymbol{s}_i)\,. \tag{2.43}$$

The spin multiplicity of a system is given by $S(S+1)$, where S is the expectation value of $\hat{S}^2$. In the absence of a magnetic-field or relativistic terms in the Hamiltonian of the system, it is possible to use spinors that are either only α or only β:

$$v_i(\boldsymbol{x}_i) = \begin{cases} \varphi_{i\alpha}(\boldsymbol{r}_i)\alpha(\boldsymbol{s}_i) & \text{if electron } i \text{ is spin up} \\ \varphi_{i\beta}(\boldsymbol{r}_i)\beta(\boldsymbol{s}_i) & \text{if electron } i \text{ is spin down} \end{cases}, \tag{2.44, 2.45}$$

or in the two-component notation this becomes

$$v_i(\boldsymbol{r}_i) = \begin{pmatrix} \varphi_{i\alpha}(\boldsymbol{r}_i) \\ 0 \end{pmatrix} \text{or} \begin{pmatrix} 0 \\ \varphi_{i\beta}(\boldsymbol{r}_i) \end{pmatrix}. \tag{2.46}$$

The number of α and β electrons in a system is given by N_α and N_β, respectively. If $N_\alpha = N_\beta$, the system is said to be closed shell and a spin-restricted formalism, in which $\varphi_{i\alpha}(\boldsymbol{r}_i) = \varphi_{i\beta}(\boldsymbol{r}_i)$ can be used. In what immediately follows however, we will keep using the spin-orbitals v_i, as this makes the equations more compact and general. It is always possible to derive the spin-restricted and spin-unrestricted equations from their general form, and this is often done because are they computationally more advantageous.
The Slater determinant for an N_{el} system is

$$|v_1 \cdots v_{N_{el}}\rangle = \frac{1}{\sqrt{N_{el}!}} \begin{vmatrix} v_1(\boldsymbol{x}_1) & \cdots & v_1(\boldsymbol{x}_{N_{el}}) \\ v_2(\boldsymbol{x}_1) & \cdots & v_2(\boldsymbol{x}_{N_{el}}) \\ \vdots & \ddots & \vdots \\ v_{N_{el}}(\boldsymbol{x}_1) & \cdots & v_{N_{el}}(\boldsymbol{x}_{N_{el}}) \end{vmatrix}. \tag{2.47}$$

A determinant has the property that if two of its rows are swapped, the opposite of that same determinant is obtained, i.e.

$$\begin{aligned} |\psi\rangle = |v_1 \cdots v_{N_{el}}\rangle &= \frac{1}{\sqrt{N_{el}!}} \begin{vmatrix} v_1(\boldsymbol{x}_1) & \cdots & v_1(\boldsymbol{x}_{N_{el}}) \\ v_2(\boldsymbol{x}_1) & \cdots & v_2(\boldsymbol{x}_{N_{el}}) \\ \vdots & \ddots & \vdots \\ v_{N_{el}}(\boldsymbol{x}_1) & \cdots & v_{N_{el}}(\boldsymbol{x}_{N_{el}}) \end{vmatrix} \\ &= \frac{-1}{\sqrt{N_{el}!}} \begin{vmatrix} v_2(\boldsymbol{x}_1) & \cdots & v_2(\boldsymbol{x}_{N_{el}}) \\ v_1(\boldsymbol{x}_1) & \cdots & v_1(\boldsymbol{x}_{N_{el}}) \\ \vdots & \ddots & \vdots \\ v_{N_{el}}(\boldsymbol{x}_1) & \cdots & v_{N_{el}}(\boldsymbol{x}_{N_{el}}) \end{vmatrix}, \end{aligned} \tag{2.48}$$

and the same holds for the swapping of columns. We therefore have that $|\psi\rangle$ is antisymmetric with respect to particle exchange; a requirement for a wavefunction describing a system of fermions (such as electrons).
In order to obtain the HF equation, it is also necessary to use the variational principle. This principle states that, out of all possible N-electron wavefunctions for an N-electron system, the ground-state wavefunction is the one which minimizes the energy. More accurately stated,

let $|\psi\rangle$ be a N-electron wavefunction, E_0 the ground-state energy of the system and $|\psi_0\rangle$ the ground-state wavefunction. The energy

$$E = \langle\psi|\hat{H}_{el}|\psi\rangle = E_0 \,, \tag{2.49}$$

if and only if $|\psi\rangle = |\psi_0\rangle$. Moreover, if $|\psi\rangle \neq |\psi_0\rangle$, then $E > E_0$. So if we have two different N-electron wavefunctions $|\psi_1\rangle$ and $|\psi_2\rangle$ and that

$$\langle\psi_1|\hat{H}_{el}|\psi_1\rangle > \langle\psi_2|\hat{H}_{el}|\psi_2\rangle \,, \tag{2.50}$$

then we know that $|\psi_2\rangle$ is closer to the true ground-state wavefunction.

We will not go into the details of how the HF equation is derived, but the starting point is to express the energy of the system using $|\upsilon_1 \cdots \upsilon_{N_{el}}\rangle$:

$$\begin{aligned} E^{HF} &= \langle\psi|\hat{H}_{el}|\psi\rangle \\ &= \sum_i^{N_{el}} H_i + \frac{1}{2}\sum_i^{N_{el}}\sum_j^{N_{el}} \left[J_{ij} - K_{ij}\right] \,, \end{aligned} \tag{2.51}$$

where

$$\begin{aligned} H_i &= \int d\boldsymbol{x}\upsilon_i^*(\boldsymbol{x}) \left[-\frac{1}{2}\nabla_{\boldsymbol{r}}^2 + V_{e-n}(\boldsymbol{x})\right] \upsilon_i(\boldsymbol{x}) \\ J_{ij} &= \int d\boldsymbol{x} \int d\boldsymbol{x}' \upsilon_i^*(\boldsymbol{x})\upsilon_i(\boldsymbol{x}) \frac{1}{||\boldsymbol{r}-\boldsymbol{r}'||} \upsilon_j^*(\boldsymbol{x}')\upsilon_j(\boldsymbol{x}') \\ K_{ij} &= \int d\boldsymbol{x} \int d\boldsymbol{x}' \upsilon_i^*(\boldsymbol{x})\upsilon_j(\boldsymbol{x}) \frac{1}{||\boldsymbol{r}-\boldsymbol{r}'||} \upsilon_i(\boldsymbol{x}')\upsilon_j^*(\boldsymbol{x}') \,. \end{aligned} \tag{2.52}$$

The next step in the derivation of the Hartree-Fock equation is to use the techniques of the calculus of variations in order to find which $\upsilon_i(\boldsymbol{x})$ minimize the expression (2.51) (because of the variational principle). The details of the derivation are shown in Ref. [27]. The resulting

Hartree-Fock equation is as follows:

$$\left\{-\frac{1}{2m}\nabla^2_{\boldsymbol{r}} + V_{e-n}(\boldsymbol{r}) + \frac{1}{2}\sum_j \left[2\hat{J}_j - \hat{K}_j\right]\right\} v_i(\boldsymbol{x}) = \epsilon_i^{HF} v_i(\boldsymbol{x})\,. \tag{2.53}$$

In the above equation[2], the ϵ_i^{HF} are the eigenvalues of the operator in the curly brackets (called the Fock operator), each one corresponding to a $v_i(\boldsymbol{x})$. The operators J_j and K_j are the Coulomb and exchange operators, respectively. They are defined as:

$$\hat{J}_j v_i(\boldsymbol{x}) = v_i(\boldsymbol{x}) \int d\boldsymbol{x}' \frac{|v_j(\boldsymbol{x}')|^2}{||\boldsymbol{r} - \boldsymbol{r}'||} \tag{2.54}$$

$$\hat{K}_j v_i(\boldsymbol{x}) = v_j(\boldsymbol{x}) \int d\boldsymbol{x}' \frac{v_i^*(\boldsymbol{x}') v_j^*(\boldsymbol{x}')}{||\boldsymbol{r} - \boldsymbol{r}'||} \tag{2.55}$$

Both J_j and K_j are one-body operators, that is to say, they act on a single degree of freedom $\boldsymbol{r} = (x, y, z)$ at a time. Notice that we have dropped the index i from $\boldsymbol{x}_i$ in (2.53). This is because Eq. (2.53) is a one-body equation and $\boldsymbol{r}$ is not a $3N_{el}$-dimensional vector anymore, as it was in the previous section.

Despite being a one-body equation, Eq. (2.53) cannot be solved analytically because the operators J_j and K_j depend on the $v_i(\boldsymbol{x})$. This means that the equation has to be solved iteratively, or "self-consistently".
One starts with an initial guess for the $v_i(\boldsymbol{x})$, constructs the operators J_j and K_j and solves Eq. (2.53) for the $v_i(\boldsymbol{x})$ and ϵ_i^{HF}. After this is done, the operators J_j and K_j are built once again, with the new $v_i(\boldsymbol{x})$ and equation (2.53) is solved a second time. This cycle is repeated until the $v_i(\boldsymbol{x})$ and the ϵ_i^{HF} do not change anymore, or – if the solving of the equation is done numerically – until the change is under a defined threshold value[3].
Once Eq. (2.53) has been solved, the wavefunction $|\psi\rangle$ is known and the energy, as well as other observables, can be calculated (since the Hamiltonian, i.e. the total energy, determines all the properties of the system).
In practice, the $v_i(\boldsymbol{x})$ are expressed as a linear combination of a finite basis set of functions. These could be atomic orbitals or plane waves, for example. In this case equation (2.53) becomes a linear algebra problem (a system of linear equations) called the Roothaan-Hall equation.

[2] This form of the HF equation is called the canonical HF equation. The form of the HF equation obtained through this kind of derivation is actually a set of N_{el} coupled equations, which can however, be brought to the canonical form via a unitary transformation. For more details see Ref. [27].

[3] Most codes use several parameters, including differences between density matrices. For more information see Ref. [27]

2.3.2 Density Functional Theory

The electronic density $\rho(\boldsymbol{r})$

Methods that go beyond HF are, by definition, methods that try to recover electron correlation. Configuration Interaction (CI), Møller-Plesset perturbation theory, Coupled-cluster theory (CC) are examples of post-HF methods and try to capture electron correlation by improving upon the HF wavefunction.
We will not go into a discussion about electronic correlation, since it goes beyond the scope of this work and the subject is discussed in-depth in references [27, 28]. We will just say that the correlation energy for a system E_{corr} is defined as the difference between the true electronic energy and the HF energy $E_{corr} = E_{el} - E^{HF}$. We will however, discuss Density Functional Theory (DFT) in some detail, since it is the main electronic-structure method we used in this work.
DFT is very different from other electronic-structure methods in that it does not focus on improving upon the Hartre-Fock wavefunction in order to recover electron correlation. In DFT the electronic density ρ substitutes the electronic wavefunction ψ in the central role of the theory. $\rho(\boldsymbol{r})$ is a real-valued function that depends on a single three-dimensional vector $\boldsymbol{r} = (x, y, z)$ representing a point in space;

$$\begin{aligned} &\mathbb{R}^3 \longrightarrow \mathbb{R} \\ &\boldsymbol{r} \longmapsto \rho(\boldsymbol{r})\,. \end{aligned} \tag{2.56}$$

Compare this to the N-electron wavefunction, a complex valued function of a $3N_{el}$-dimensional vector $\boldsymbol{r} = (\boldsymbol{r}_1, \boldsymbol{r}_2, \ldots, r_{N_{el}})$ containing the positions of each electron in space;

$$\begin{aligned} &\mathbb{R}^{3N_{el}} \to \mathbb{C} \\ &\boldsymbol{r}_e \longmapsto \psi(\boldsymbol{r}_e) \end{aligned} \tag{2.57}$$

The electronic density can be defined as

$$\rho(\boldsymbol{r}_1) = \int d\boldsymbol{s}_1 \int d\boldsymbol{x}_2 \cdots \int d\boldsymbol{x}_{N_{el}}\, \psi^*(\boldsymbol{x}_1, \ldots, \boldsymbol{x}_{N_{el}})\psi(\boldsymbol{x}_1, \ldots, \boldsymbol{x}_{N_{el}})\,. \tag{2.58}$$

In HF theory, it has a particularly simple expression:

$$\rho(\boldsymbol{r}) = \sum_{i}^{N_\alpha} |\varphi_{i\alpha}(\boldsymbol{r})|^2 + \sum_{i}^{N_\beta} |\varphi_{i\beta}(\boldsymbol{r})|^2 \tag{2.59}$$

$$= \rho_\alpha(\boldsymbol{r}) + \rho_\beta(\boldsymbol{r}) \tag{2.60}$$

Where $\rho^\alpha(\boldsymbol{r})$ are $\rho^\beta(\boldsymbol{r})$ the α and β electronic-densities, respectively. In a closed-shell system and in the absence of operators that act explicitly on the spin degrees of freedom, these should be equal.
Clearly, ρ is a much simpler object than ψ, and if we can extract the same information from ρ and ψ, it's preferable to work with ρ. This is the motivation behind DFT.
The justification for this approach comes from the Hohenberg-Kohn (HK) theorem [29], which states that there is a one-to-one correspondence between an electronic Hamiltonian H_{el} and an electronic density ρ.
More specifically, the first part of the theorem states that an external (time-independent) potential acting on a system of electrons is an unique functional of ρ, up to a constant. In other words, the electronic density ρ of the system determines the external potential, up to a constant.
The external potential V_{ext} is the potential energy term in the Hamiltonian that is not the electron-electron interaction (we omit V_{n-n}):

$$\hat{H}_{el} = \hat{T}_e + V_{e-e} + V_{ext} \,. \tag{2.61}$$

V_{ext} is almost always the electron-nuclear interaction, i.e. $V_{ext} = V_{e-n}$ (but it could be any electrostatic field, for example). From another viewpoint V_{ext} is a potential that only acts on one electronic degree of freedom at a time

$$V_{ext}(\boldsymbol{r}_e) = \sum_{i}^{N_{el}} v(\boldsymbol{r}_i) \,. \tag{2.62}$$

The term $\hat{T}_e + V_{e-e}$ of Eq. (2.61) is universal, because it is the same for any electronic system of N_{el} electrons. The external potential, on the other hand, is not universal because it depends on the type of nuclei composing the molecule, and their respective positions.
Knowing the external potential therefore determines the electronic Hamiltonian, which is, by the Hohenberg-Kohn theorem, determined by the electronic density. This also means that all other observables are determined by ρ.
A functional is, in simple terms, a function of a function. In HK theory, the electronic energy of the system is a (unique) functional of ρ and can be written as

$$E_{el}[\rho] = T_e[\rho] + U_{e-e}[\rho] + U_{e-n}[\rho] \\ = T_e[\rho] + U_{e-e}[\rho] + \int d\boldsymbol{r}\,\rho(\boldsymbol{r}) V_{e-n}(\boldsymbol{r})\,. \tag{2.63}$$

The square brackets in $E_{el}[\rho]$ mean that the energy is a functional of ρ. We have subdivided the energy in its three contributions; the kinetic energy, the electron-electron interaction and the electron-nuclear interaction. These three terms are all functionals of ρ, but only the explicit form of U_{e-n} is known. U_{e-e} contains all energy contributions arising from electron-electron interactions (including quantum effects such as correlation and exchange). Notice that we have used the letter U instead V to emphasize that these are functionals of ρ and not functions of $\boldsymbol{r}$.
The second part of the Hohenberg-Kohn theorem states that for a given system of N_{el} electrons under the influence of V_{ext}, the minimal value of $E_{el}[\rho]$ is obtained if and only if $\rho = \rho_0$, where ρ_0 is the ground-state density of the system. Furthermore, if $\rho \neq \rho_0$, then $E_{el}[\rho] > E_{el}[\rho_o]$. In other words, it gives a variational principle for the energy as a functional of the density.
In fact it is possible to apply – just as in the case of HF – the calculus of variations to Eq. (2.63) in order to obtain an equation that actually gives us the energy of the system. This leads to the equation

$$\frac{\delta T_e[\rho]}{\delta\rho} + \frac{\delta U_{e-e}[\rho]}{\delta\rho} + \frac{\delta U_{e-n}[\rho]}{\delta\rho} - \mu = 0 \tag{2.64}$$

whee $\frac{\delta}{\delta\rho}$ denotes the functional derivative and $\mu = \frac{\delta E_{el}}{\delta\rho}$ is the chemical potential[4]. It is only possible to solve Eq. (2.64) if the forms of $T_e[\rho]$ and $U_{e-e}[\rho]$ are known. Unfortunately there are only approximations for these terms. The form of $U_{e-n}[\rho]$ is

$$U_{e-n}[\rho] = \int d\boldsymbol{r}\,\rho(\boldsymbol{r}) V_{e-n}(\boldsymbol{r}) \tag{2.65}$$

and its functional derivative is

$$\frac{\delta U_{e-n}[\rho]}{\delta\rho} = V_{e-n}(\boldsymbol{r})\,. \tag{2.66}$$

This holds for any kind of external potential. Moreover, we can let $U_{e-e}[\rho]$ be a sum of a

[4]This arises from the requirement that the number of electrons N_{el} be conserved in the minimization. That is, that the density that minimize the energy integrate to N_{el}.

part $J[\rho]$, which describes the "classical" repulsion between the electrons and an unknown quantum contribution:

$$U_{e-e}[\rho] = J[\rho] + quantum \tag{2.67}$$

where

$$J[\rho] = \frac{1}{2}\int d\boldsymbol{r}' \int d\boldsymbol{r} \frac{\rho(\boldsymbol{r})\rho(\boldsymbol{r}')}{||\boldsymbol{r}-\boldsymbol{r}'||}\,, \tag{2.68}$$

with functional derivative

$$\frac{\delta J[\rho]}{\delta \rho} = \int d\boldsymbol{r}' \frac{\rho(\boldsymbol{r}')}{||\boldsymbol{r}-\boldsymbol{r}'||}\,. \tag{2.69}$$

$J[\rho]$ describes the total energy arising from the Coulomb repulsion between every infinitesimal charge volume $\rho(\boldsymbol{r})d\boldsymbol{r}$ with every other infinitesimal charge volume $\rho(\boldsymbol{r}')d\boldsymbol{r}'$.
If we have a system of electrons that interact only classically, we can neglect the quantum contribution of $U_{e-e}[\rho]$ and write Eq. (2.64) as

$$\frac{\delta T_e[\rho]}{\delta \rho} + V_{e-n}(\boldsymbol{r}) + \frac{1}{2}\int d\boldsymbol{r}' \frac{\rho(\boldsymbol{r}')}{||\boldsymbol{r}-\boldsymbol{r}'||} - \mu = 0 \tag{2.70}$$

where we have also used (2.66) and (2.69). This will be important in the next section, where we discuss Kohn-Sham DFT.

Kohn-Sham DFT

The HK theorems are existence theorems and as such do not provide a practical route to obtain the ground-state density or the energy functional. As mentioned in the previous section it is necessary to make approximations in order to obtain expressions for $T_e[\rho]$ and $U_{e-e}[\rho]$ so that all the functional derivatives in Eq. (2.64) can be evaluated. One of the first and better known expressions for the energy functional is the Thomas-Dirac-Fermi (TDF) functional [28, 30, 31], which is based on the idea that electrons are locally uniformly distributed in phase-space, that is to say, they are uniformly distributed if we consider a small volume element of phase space. Using this assumption and the Fermi-Dirac distribution it is possible to derive an expression

for the kinetic energy functional:

$$T_{TDF}[\rho] = C_F \int d\boldsymbol{r}\rho^{5/3}(\boldsymbol{r})\,. \tag{2.71}$$

with $C_F = \frac{3}{10}(3\pi^2)^{2/3}$. This approach is called the "local density approximation".
The TDF energy functional is built by using (2.71) as well as by neglecting exchange-correlation energy and considering only classical electrostatic interactions:

$$E_{TDF}[\rho] = C_F \int d\boldsymbol{r}\rho^{5/3}(\boldsymbol{r}) + \int d\boldsymbol{r}\rho(\boldsymbol{r})V_{e-n}(\boldsymbol{r}) + \frac{1}{2}\int d\boldsymbol{r}' \int d\boldsymbol{r}\frac{\rho(\boldsymbol{r})\rho(\boldsymbol{r}')}{||\boldsymbol{r}-\boldsymbol{r}'||}\,. \tag{2.72}$$

Unfortunately $E_{TDF}[\rho]$ leads to inaccurate results for molecular systems, mostly because the TDF approximation to the kinetic energy is poor for realistic systems.
Although there is ongoing research in wavefunction-free DFT (of which TDF is an example), the overwhelming majority of DFT calculations use the framework of the Kohn-Sham (KS) equations [32].
The essential idea behind the KS theory is that the kinetic energy of a system of N_{el} interacting electrons can be well approximated by the kinetic energy of a system of N_{el} "non-interacting" fermions. It can be shown that for such a non-interacting system the electronic density can be expressed as

$$\rho(\boldsymbol{r}) = \sum_{i}^{N_{el}}\sum_{\varsigma}|\varphi_{i\varsigma}(\boldsymbol{r})|^2 \tag{2.73}$$

where the $\varphi_{i\varsigma}(\boldsymbol{r})$ are one-electron wavefunctions. Notice we now keep track of the spins of the wavefunctions via the index ς because this will be useful in expressions that will appear later on. It is unnecessary however, to keep using the $v_i(\boldsymbol{x})$ as the spin-orbitals are either only α or only β (see Eqns. (2.45)). The summations over spin indices (such as ς) will always run over $\{\alpha,\beta\}$.
The kinetic energy for a non-interacting system system is

$$\sum_{i}^{N_{el}}\sum_{\varsigma}\langle\varphi_{i\varsigma}|\frac{-1}{2m}\nabla_r^2|\varphi_{i\varsigma}\rangle\,. \tag{2.74}$$

The advantage of a dealing with this non-interacting system of fermions is clear; the equations for a system of non-interacting fermions are well known and easy to solve.

As we saw in Eq. (2.63), HK showed that energy of a system of electrons can expressed as a functional of the density as

$$E[\rho] = T_e[\rho] + U_{e-e}[\rho] + U_{e-n}[\rho] \,. \tag{2.75}$$

Kohn and Sham proposed that $E[\rho]$ be written as

$$E_{el}^{KS}[\rho] = T_e^s[\rho] + U_{e-n}[\rho] + J[\rho] + E_{xc}[\rho] \tag{2.76}$$

$T_e^s[\rho]$ is the kinetic energy of the electrons of the non-interacting system. Its form in terms of ρ is not known, but it can be written in terms of the $\varphi_{i\varsigma}(\boldsymbol{r})$, as see in in Eq. (2.74). The kinetic energy of the system has therefore been approximated by the kinetic energy of a system of non-interacting electrons. The term $E_{xc}[\rho]$ – the exchange-correlation energy –appears exactly as a correction to the fact that $T_e[\rho]$ was approximated and that the non-classical electron-electron interaction was excluded from $U_{e-e}[\rho]$ in the expression (2.74). $E_{xc}[\rho]$ is then necessarily written as

$$E_{xc}[\rho] = U_{e-e} - J[\rho] + T_e[\rho] - T_e^s[\rho] \,. \tag{2.77}$$

By applying the calculus of variations to Eq. (2.76), just as it was applied to Eq. (2.63), we obtain:

$$\frac{\delta T_e^s[\rho]}{\delta \rho} + V_{e-n}(\boldsymbol{r}) + V_{xc}(\boldsymbol{r}) + \frac{1}{2}\int d\boldsymbol{r}' \frac{\rho(\boldsymbol{r}')}{||\boldsymbol{r} - \boldsymbol{r}'||} - \mu = 0 \tag{2.78}$$

If we inspect Eq. (2.70) and compare it to Eq. (2.78), we notice that the two equations are analogous, and Eq. (2.78) therefore describes a system of non-interacting electrons. The Schrödinger equation for such a system is well-known:

$$\left(-\frac{1}{2m}\nabla_{\boldsymbol{r}}^2 + V_{ext}^{eff}(\boldsymbol{r})\right)\varphi_{i\varsigma}(\boldsymbol{r}) = \epsilon_{i\varsigma}^{KS}\varphi_{i\varsigma}(\boldsymbol{r}) \tag{2.79}$$

where we have set

$$V_{eff}^{\varsigma}(\boldsymbol{r}) = V_{e-n}(\boldsymbol{r}) + J(\boldsymbol{r}) + V_{xc}^{\varsigma}(\boldsymbol{r}). \tag{2.80}$$

Notice that this can only be true if $V_{xc}^{\varsigma}(\boldsymbol{r})$ has the form of an external potential, and therefore

$$E_{xc}[\rho] = \int d\boldsymbol{r}\, V_{xc}^{\varsigma}(\boldsymbol{r})\rho^{\varsigma}(\boldsymbol{r}) \tag{2.81}$$

and

$$V_{xc}^{\varsigma}(\boldsymbol{r}) = \frac{\delta E_{xc}[\rho]}{\delta \rho_{\varsigma}(\boldsymbol{r})}\,, \tag{2.82}$$

which is admittedly strange, since it is supposed to account for all many-electron effects.
By solving Eq. (2.79) it is thus possible to find an electronic density that satisfies Eq. (2.78), via the use of Eq. (2.73). Furthermore, the energy of the system is found by inserting this density into Eq. (2.76) and using Eq. (2.74).
Equation (2.79) is known as the Kohn-Sham equation, and the single-particle functions $\varphi_i(\boldsymbol{r})$ appearing in it are known as the Kohn-Sham orbitals. This equation is very similar to the HF equation (it is even simpler, since there is no exchange term) and has to be solved iteratively too, since $V_{eff}^{\varsigma}(\boldsymbol{r})$ depends on the $\varphi_{i\varsigma}(\boldsymbol{r})$.

The precise form of $E_{xc}[\rho]$ – and therefore of $V_{xc}^{\varsigma}(\boldsymbol{r})$ – is not known (or else the many-electron problem would be solved). There are however, a whole range of approximations for $E_{xc}[\rho]$. For very many of these approximations the computational cost of solving the KS equation is of the same order of HF, but more accurate. It turns out that the approximation to $T_e[\rho]$ made by KS is very good, and a lot of the inaccuracy of the TDF energy functional came from a poor approximation of this term. DFT has thus become an extremely successful electronic structure method because of its relative accuracy, low computational cost and ease of use.
For more details about the DFT, including discussions on $E_{xc}[\rho]$, the derivation of theorems and equations and the meaning of μ, see Refs. [28, 33].

2.3.3 Time-dependent Density Functional Theory

In this section we are going to discuss Time-dependent DFT (TDDFT). This is the time-dependent analogue of Kohn-Sham theory in which $\rho(\boldsymbol{r})$ becomes time-dependent $\rho(\boldsymbol{r}, t)$. We turn to TDDFT because it allows for the calculation of electronic excited-states of molecules and atoms. The excitation of an electron to a higher energy state is caused by light; an

electromagnetic field that varies with time. Light will be treated classically (as a wave, not as photons) and as a perturbation. The resulting equations will actually be time-independent and we will refer to the theory as linear-response TDDFT (LR-TDDFT). TDDFT can also be used to simulate the evolution of a density, but most numerical implementations of TDDFT are actually LR-TDDFT, even though they are referred to simply as TDDFT.
We start by mentioning the Runge-Gross (RG) theorem [34]; the time-dependent analogue of the Hohenberg-Kohn theorem. The RG theorem is a statement about a system of N-electrons described by the time-dependent Scrödinger equation

$$i\frac{d}{dt}|\psi(t)\rangle = \hat{H}_{el}(t)|\psi(t)\rangle\,, \tag{2.83}$$

where the electronic Hamiltonian $\hat{H}_{el}(t)$

$$\hat{H}_{el}(t) = \hat{T}_e + \hat{V}_{e-e} + \hat{V}_{ext}(t)\,, \tag{2.84}$$

now contains a time-dependent external potential

$$V_{ext}(t) = \sum_{i}^{N_{el}} V(\boldsymbol{r}_i, t)\,. \tag{2.85}$$

Where the $\boldsymbol{r}_i$ are the coordinates of each electron, $V_{ext}(t)$, for example, can be the result of a time-varying electric field. It can also certainly include a time-independent part such as V_{e-n}. The first part of the RG theorem states that, for a system such as the one described, $\rho(\boldsymbol{r}, t)$ determines $V_{ext}(\boldsymbol{r}, t)$ up to a time-dependent constant $c(t)$ (independent of $\boldsymbol{r}$). The time-dependent electronic wavefunction $|\psi(t)\rangle$ is therefore also determined, up to a time-dependent phase factor. Another way of stating this is that there is a one-to-one correspondence between $\rho(\boldsymbol{r}, t)$ and $|\psi(t)\rangle$, up to a constant $c(t)$.
In the RG theorem, instead of an energy functional $E_{el}[\rho]$, we have an action functional

$$A[\rho] = \int_{t_0}^{t} dt' \langle\psi(t)|i\frac{d}{dt'} - \hat{H}_{el}(t')|\psi(t')\rangle\,. \tag{2.86}$$

The action functional $A[\rho]$ is a unique functional of $\rho(\boldsymbol{r}, t)$, up to an additive time-dependent constant. The true, time-dependent density $\rho(\boldsymbol{r}, t)$ of the system is a stationary point of the

action:

$$\frac{\delta A[\rho]}{\delta \rho(\boldsymbol{r},t)} = 0\,. \tag{2.87}$$

This last statement is the equivalent of the second part of the HK theorem, since the minimization[5] of $A[\rho]$ can be used to obtain the equations of motion for the system.
In fact it is also possible to arrive at the time-dependent Kohn-Sham equation, by following a reasoning similar to that of section 2.3.2, but by using the action instead of the energy. The time-dependent KS equation is

$$\left[-\frac{1}{2}\nabla^2 + V^{\varsigma}_{eff}(\mathbf{r},t)\right]\varphi_{i\varsigma}(\mathbf{r},t) = H^{KS}\varphi_{i\varsigma}(\mathbf{r},t) = i\frac{\partial}{\partial t}\varphi_{i\varsigma}(\mathbf{r},t)\,, \tag{2.88}$$

the time-dependent Kohn-Sham orbitals $\varphi_{i\varsigma}$, which respect the following initial conditions

$$\varphi_{i\varsigma}(\mathbf{r},0) = \varphi_{i\varsigma}(\mathbf{r})\,, \tag{2.89}$$

can be used to recover $\rho(\boldsymbol{r},t)$ through

$$\rho(\mathbf{r},t) = \rho_\alpha(\mathbf{r},t) + \rho_\beta(\mathbf{r},t) = \sum_i^{N_\alpha} |\varphi_{i\alpha}(\mathbf{r},t)|^2 + \sum_i^{N_\beta} |\varphi_{i\beta}(\mathbf{r},t)|^2 = \sum_i^{N}\sum_{\varsigma} |\varphi_{i\varsigma}(\mathbf{r},t)|^2\,. \tag{2.90}$$

The effective potential is now

$$V^{\varsigma}_{eff}(\mathbf{r},t) = V^{\varsigma}_{ext}(\mathbf{r},t) + \int d\mathbf{r}'\,\frac{\rho(\mathbf{r},t)}{|\mathbf{r}-\mathbf{r}'|} + V^{\varsigma}_{xc}(\mathbf{r},t) \tag{2.91}$$

$$= V^{\varsigma}_{ext}(\mathbf{r},t) + V^{\varsigma}_{SCF}(\mathbf{r},t)\,, \tag{2.92}$$

where V_{SCF} is dubbed the "self-consistent field" part of the potential because it depends on

[5] More precisely, it is enough to find a stationary point of $A[\rho]$.

the $\varphi_{i\varsigma}$. The exchange correlation potential $V_{xc}^{\varsigma}(\boldsymbol{r},t)$ is defined as

$$V_{xc}^{\varsigma}(\boldsymbol{r},t) = \frac{\delta A_{xc}[\rho]}{\delta\rho(\boldsymbol{r},t)}\,. \tag{2.93}$$

In practice, $V_{xc}^{\varsigma}(\boldsymbol{r},t)$ is almost always approximated by

$$V_{xc}^{\varsigma}(\boldsymbol{r},t) = \left.\frac{\delta E_{xc}[\rho]}{\delta\rho(\boldsymbol{r})}\right|_{\rho(\boldsymbol{r})=\rho(\boldsymbol{r},t)} \tag{2.94}$$

which is called the adiabatic approximation. Eq. (2.94) implies that we simply take the exchange-correlation energy functional E_{xc} as a replacement for the exchange-correlation action functional A_{xc}, and evaluate it at the density ρ at time t. This approximation is made because the time-dependence of A_{xc} is not known, and in this way it is possible to directly exploit approximations for E_{xc} – developed for ground-state DFT – in TDDFT. For more information about the adiabatic approximation see Refs. [35, 36].

Linear-response TDDFT

In linear-response theory one measures how a physical observable $O(t)$ responds to a perturbation $H^{(1)}(t)$, assuming that the response of $O(t)$ is only linear. Suppose that at $t > t_0$ the system is in its ground-state, then the expectation value of O is

$$\langle\psi_0|\hat{O}|\psi_0\rangle \tag{2.95}$$

at t_0 a time-dependent perturbation is turned on. This perturbation is

$$\hat{H}^{(1)}(t) = f(t)\hat{O}'\,, \tag{2.96}$$

and it couples O to another observable O' through a time-dependent applied field or external agent $f(t)$. The expectation value of O thus becomes time-dependent for $t \geq t_0$:

$$\langle\psi(t)|\hat{O}|\psi(t)\rangle\,. \tag{2.97}$$

The difference between the expectation value of O when the system is in its ground-state and its expectation value at $t \geq t_0$ is called the response of O (to the perturbation). By assuming that this response is linear in $f(t)$ and by using a first-order approximation to the quantum evolution operator [35, 20] one arrives at the following equation:

$$O^{(1)}(t) = \int_{t_0}^{t_f} dt' \chi(t,t') f(t') \,, \tag{2.98}$$

where $O^{(1)}$ is the linear (or first-order) response of O and $\chi(t,t')$ is the linear-response function. The response function is an intrinsic property of the system and does not depend on the form of the perturbation. Moreover, since $\chi(t,t')$ is zero for $t < t_0$ and $t > t_f$, Eq. (2.99) is often written as

$$O^{(1)}(t) = \int_{-\infty}^{+\infty} dt' \chi(t-t') f(t') \,. \tag{2.99}$$

Eq. (2.99) will often be Fourier-transformed to bring it to the frequency domain:

$$O^{(1)}(\omega) = \chi(\omega) f(\omega) \,. \tag{2.100}$$

In LR-TDDFT, our interest will turn to the density-density response function $\chi_{\rho\rho}(t-t')$. The electron density operator is

$$\hat{\rho}(\boldsymbol{r}) = \sum_{i}^{N_{el}} \delta(\boldsymbol{r} - \boldsymbol{r}_i). \tag{2.101}$$

The perturbation $H^{(1)}(t)$ can be therefore be written as

$$H^{(1)}(t) = \int d\boldsymbol{r}' V^{(1)}(\boldsymbol{r}', t) \hat{\rho}(\boldsymbol{r}') = \sum_{i}^{N_{el}} V^{(1)}(\boldsymbol{r}_i, t) \,, \tag{2.102}$$

and the first-order density response becomes

$$\rho^{(1)}(\mathbf{r},t) = \int dr' \int dt' \chi_{\rho\rho}(\mathbf{r},\mathbf{r}',t-t')V^{(1)}(\mathbf{r}',t') \,. \tag{2.103}$$

The above equation describes how the electronic density responds to an applied potential $V^{(1)}(t)$ resulting from the interaction with light, taken to be an oscillating electric field. Notice that $\chi_{\rho\rho}(\mathbf{r},\mathbf{r}',t-t')$ can be expressed as a functional derivative

$$\chi_{\rho\rho}(\mathbf{r},\mathbf{r}',t-t') = \frac{\delta O(\mathbf{r}',t')}{\delta V^{(1)}(\mathbf{r}',t')} \,. \tag{2.104}$$

Since our system is now acted upon by $V^{(1)}(\boldsymbol{r},t)$, this term has to be added to the Kohn-Sham Hamiltonian as well[6], namely

$$V^{\varsigma}_{eff}(\mathbf{r},t) = V^{\varsigma}_{ext}(\mathbf{r},t) + V^{(1)}(\boldsymbol{r},t) + V^{\varsigma}_{SCF}(\mathbf{r},t) \,. \tag{2.105}$$

Since a change in the density implies a change in $V^{\varsigma}_{SCF}(\mathbf{r},t)$, the effective perturbation will be $V^{(1)}_{KS}(\boldsymbol{r},t)$,

$$V^{(1)}_{KS}(\boldsymbol{r},t) \neq V^{(1)}(\boldsymbol{r},t) \,. \tag{2.106}$$

The response of the density, written in term of Kohn-Sham quantities is

$$\rho^{(1)}(\mathbf{r},t) = \int dr' \int dt' \chi^{KS}_{\rho\rho}(\mathbf{r},\mathbf{r}',t-t')V^{(1)}_{KS}(\mathbf{r}',t') \,. \tag{2.107}$$

Since both (2.103) and (2.107) equal $\rho^{(1)}(\mathbf{r},t)$[7], and since that $\chi_{\rho\rho}(\mathbf{r},\mathbf{r}',t-t')$ is an intrinsic property of the system that does not depend on the form of $V^{KS}_{app}(\mathbf{r}',t')$, after a few steps (see Ref. [35]), one can find that

$$\chi_{\rho\rho}(\mathbf{r},\mathbf{r}',\omega) = \chi^{KS}_{\rho\rho}(\mathbf{r},\mathbf{r}',\omega) + \int d\boldsymbol{r}'' \int d\boldsymbol{r}''' \chi^{KS}_{\rho\rho}(\mathbf{r}'',\mathbf{r}''',\omega) \left[\frac{1}{||\boldsymbol{r}''-\boldsymbol{r}'''||} + f_{xc}(\mathbf{r},\mathbf{r}',\omega) \right] \chi_{\rho\rho}(\mathbf{r}'',\mathbf{r}''',\omega) \,.$$

[6] $H^{(1)}(\boldsymbol{r}_e,t)$ will be added to the Hamiltonian of the actual, interacting system.

[7] the density of the non-interacting system is the same as that of the non-interacting system, by construction.

(2.108)

Eq. (2.108) is written in the frequency domain and $f_{xc}(\mathbf{r},\mathbf{r}',\omega)$ is the frequency-dependent exchange-correlation kernel. In the time-domain

$$f_{xc}^{\varsigma\tau}(\mathbf{r},\mathbf{r}',t,t') = \frac{\delta^2 A_{xc}[\rho]}{\delta\rho_\varsigma(\boldsymbol{r},t)\delta\rho_\tau(\boldsymbol{r}',t')}\,. \tag{2.109}$$

Within the adiabatic approximation f_{xc} becomes

$$f_{xc}^{\varsigma\tau}(\mathbf{r},\mathbf{r}',t,t') = \delta(t-t')\frac{\delta^2 E_{xc}[\rho]}{\delta\rho_\varsigma(\boldsymbol{r})\delta\rho_\tau(\boldsymbol{r}')} \tag{2.110}$$

where $\rho(\boldsymbol{r})$ is the ground state density. In the frequency domain f_{xc} becomes frequency-independent because of the adiabatic-approximation.
Equation (2.108) can be compactly re-written as

$$\chi^{-1}(\mathbf{r},\mathbf{r}',\omega) = \chi_{KS}^{-1}(\mathbf{r},\mathbf{r}',\omega) - \frac{1}{||\boldsymbol{r}-\boldsymbol{r}'||} - f_{xc}(\mathbf{r},\mathbf{r}',\omega) \tag{2.111}$$

where $\chi^{-1}(\mathbf{r},\mathbf{r}',\omega)$ and $\chi_{KS}^{-1}(\mathbf{r},\mathbf{r}',\omega)$ are the inverses of $\chi(\mathbf{r},\mathbf{r}',\omega)$ and $\chi_{KS}(\mathbf{r},\mathbf{r}',\omega)$, respectively. We have dropped the $\rho\rho$ subscripts since we will only deal with the density-density response from now on.
It is worth noting that the adiabatic approximation for the xc-kernel precludes the description of some correlation effects, and as a consequence certain molecular electronic states cannot be described within this approximation. Namely, charge-transfer states and states with so-called "double excitation character" are missed in the adiabatic approximation.

Casida's method

In the section above we saw how $\chi^{-1}(\mathbf{r},\mathbf{r}',\omega)$ and $\chi_{KS}^{-1}(\mathbf{r},\mathbf{r}',\omega)$ are linked. The best known method for extracting useful information out of Eq. (2.111) is known as Casida's equation, after M.E. Casida who first derived it [37].
The advantage of dealing with $\chi_{KS}(\mathbf{r},\mathbf{r}',\omega)$ is that it has a well-known form because the KS

system is non-interacting. A matrix element of χ_{KS} expressed in the basis of the KS orbitals is

$$\chi^{KS}_{\rho\rho}(\omega) = \delta_{\varsigma,\tau}\delta_{i,k}\delta_{j,l}\frac{f_{j\varsigma} - f_{i\varsigma}}{\omega - (\epsilon^{KS}_{i,\varsigma} - \epsilon^{KS}_{j,\varsigma})} \tag{2.112}$$

where $f_{i,\varsigma}$ occupations numbers (possibly fractional) of KS orbital $\varphi_{i\varsigma}$. Knowing this, it is possible to express Eq. (2.111) in the basis of the unperturbed KS orbitals (obtained via a simple ground-state DFT calculation) and then to find the conditions for which $\chi_{\rho\rho}$ has poles, which are the transition energies of the system. This condition is given by the pseudo-eigenvalue problem

$$\begin{bmatrix} A & B \\ B^* & A^* \end{bmatrix}\begin{pmatrix}\mathbf{X}\\ \mathbf{Y}\end{pmatrix} = \omega_I \begin{bmatrix} 1 & 0 \\ 0 & -1 \end{bmatrix}\begin{pmatrix}\mathbf{X}\\ \mathbf{Y}\end{pmatrix}. \tag{2.113}$$

Here $\mathbf{X}_I$ and $\mathbf{Y}_I$ make up the eigenvector of the problem and contain information which can be used to calculate oscillator strengths. The eigenvalues ω_I are transition energies that we want to obtain.
Equation (2.113) is a pseudo-eigenvalue equation because the matrices A and B depend on ω. The expression for the elements of these matrices are:

$$A_{ia\varsigma,jb\tau}(\omega) = \delta_{\varsigma,\tau}\delta_{i,j}\delta_{a,b}(\epsilon_{b\tau} - \epsilon_{j\tau}) - K_{ia\varsigma,jb\tau}(\omega)\,, \tag{2.114}$$

$$B_{ia\varsigma,jb\tau}(\omega) = -K_{ia\varsigma,bj\tau}(\omega)\,, \tag{2.115}$$

with $K_{ia\varsigma,jb\tau}(\omega)$ an element of the coupling matrix:

$$\begin{aligned} K_{ia\varsigma,jb\tau}(\omega) = &\int\int \mathrm{d}^3\mathbf{r}\mathrm{d}^3\mathbf{r}'\varphi^*_{i\varsigma}(\mathbf{r})\varphi_{a\varsigma}(\mathbf{r})\frac{1}{|\mathbf{r}-\mathbf{r}'|}\varphi_{j\tau}(\mathbf{r}')\varphi^*_{b\tau}(\mathbf{r}') \\ &+ \int e^{i\omega(t-t')}\mathrm{d}(t-t')\left\{\int\int \mathrm{d}^3\mathbf{r}\mathrm{d}^3\mathbf{r}'\varphi^*_{i\varsigma}(\mathbf{r})\varphi_{a\varsigma}(\mathbf{r})\frac{\delta^2 A_{xc}}{\delta\rho_\varsigma(\mathbf{r},t)\delta\rho_\tau(\mathbf{r}',t')}\varphi_{j\tau}(\mathbf{r}')\varphi^*_{b\tau}(\mathbf{r}')\right\} \end{aligned} \tag{2.116}$$

The problem becomes a true eigenvalue equation when the adiabatic-approximation $\frac{\delta^2 A_{xc}}{\delta\rho_\varsigma\delta\rho_\tau} = \delta(t-t')\frac{\delta^2 E_{xc}}{\delta\rho_\varsigma\delta\rho_\tau}$ is applied, making the A, B matrices become independent of ω. It is then possible to obtain the transition energies ω_I for the system simply by doing a ground-state DFT calculation and then solving a linear-algebra equation.

It also possible to re-write (2.113) if certain conditions for E_{xc} are met:

$$\Omega \mathbf{F^I} = \omega_I^2 \mathbf{F^I} \,, \tag{2.117}$$

with $\Omega = (A-B)^{1/2}(A+B)(A-B)^{1/2}$ and $\mathbf{F^I} = (A-B)^{-1/2}(X+Y)$. Which is how Casida originally wrote the equation.

Besides the adiabatic-approximation, another very common approximation used in LR-TDDFT is the Tamm-Dancoff approximation (TDA) [38, 39, 40], in which $B = 0$. In the TDA (2.113) becomes

$$A\mathbf{X}_I = \omega_I \mathbf{X}_I \,. \tag{2.118}$$

Despite being an approximation, TDA actually often improves the results of LR-TDDFT as reduces the effects of the so-called "triplet instability" problem in which certain triplet states of the molecule have much lower energy than they should, often leading to a wrong ordering of the excited states [41, 42, 43].

In Ref. [37], Casida also discussed the problem of assigning the electronic transitions calculated with LR-TDDFT to known spectroscopic transitions (for example, a $\pi - \pi^*$ or a $n - \pi^*$ in a carboxylic acid). This exercise is relatively straightforward in most electronic structure methods, since the assignments are based on the character of the molecular orbitals that compose the excited state, which are readily available in wavefunction-based methods, but not in TDDFT. In order to overcome this problem, Casida proposed the following wavefunction:

$$|\tilde{\psi}_I\rangle = \sum_{ia\varsigma} c^I_{ia\varsigma} \hat{a}^\dagger_{a\varsigma} \hat{a}_{i\varsigma} |\psi_0\rangle \,, \tag{2.119}$$

where:

$$c^I_{ia\varsigma} = \sqrt{\frac{\epsilon^{KS}_{a\varsigma} - \epsilon^{KS}_{i\varsigma}}{\omega_I}} F^I_{ia\varsigma} \,. \tag{2.120}$$

We will refer to the object defined in (5.9) as the auxiliary "many-electron wavefunction". While it is not the true wavefunction of the excited state $|\psi_I\rangle$, it can be used in order to make the above-mentioned assignments, but also to calculate certain quantities that are difficult to

express as functionals of the electronic density.

The Sternheimer method

A different approach to extracting transition energies from the linear-response equations is called the Sternheimer method. It is based on a power series expansion of the time-dependent Kohn-Sham orbitals

$$\varphi_{k\varsigma}(\mathbf{r},t) = \varphi^{(0)}_{k\varsigma}(\mathbf{r},t) + \lambda\phi^{(1)}_{k\varsigma}(\mathbf{r},t) \tag{2.121}$$

where $\lambda \in [0,1]$ is the perturbation parameter. The electronic density can then be written as

$$\begin{aligned}\rho(\mathbf{r},t) &= \sum_{i}^{N}\sum_{\varsigma}|\varphi^{(0)}_{i\varsigma}(\mathbf{r},t)|^2 + \lambda\left[\phi^{*(1)}_{i}(\mathbf{r},t)\varphi^{(0)}_{i}(\mathbf{r},t) + \varphi^{*(0)}_{i}(\mathbf{r},t)\phi^{(1)}_{i}(\mathbf{r})\right] \\ &= \rho^{(0)}(\mathbf{r},t) + \lambda\rho^{(1)}(\mathbf{r},t)\,,\end{aligned} \tag{2.122}$$

where the $\varphi^{(0)}_{i}(\mathbf{r},\omega)$ are the KS orbitals and the $\phi^{(1)}_{i}(\mathbf{r},\omega)$ are called the linear-response (LR) orbitals. $\rho^{(1)}(\mathbf{r},\omega) = \rho^{(1)}(\mathbf{r},\omega)$ is the frequency-dependent first-order density response, which is therefore given by

$$\rho^{(1)}(\mathbf{r},\omega) = \sum_{i}^{N_{el}}\sum_{\varsigma}\phi^{*(1)}_{i\varsigma}(\mathbf{r},\omega)\varphi^{(0)}_{i\varsigma}(\mathbf{r},\omega) + \varphi^{*(0)}_{i\varsigma}(\mathbf{r},\omega)\phi^{(1)}_{i\varsigma}(\mathbf{r},\omega)\,. \tag{2.123}$$

The above expression can be plugged into Eq. (2.107). This will yield an equation depending on both the $\varphi^{(0)}$ and the $\phi^{(1)}_{i}$. This equation will also involve an infinite sum over the $\varphi^{(0)}$, because of the expression for $\chi^{KS}_{\rho\rho}$. It is however, possible to cleverly re-work this equation in order to obtain

$$x\,, \tag{2.124}$$

where

$$H^{(1)}(\omega) = \int d\boldsymbol{r}'\frac{\rho^{(1)}(\mathbf{r}',t)}{||\boldsymbol{r}-\boldsymbol{r}'||} + \int d\boldsymbol{r}'\, f_{xc}(\boldsymbol{r}\boldsymbol{r}')\rho^{(1)}(\mathbf{r}',t) \tag{2.125}$$

and

$$Q = 1 - \sum_{i=1}^{N_{el}} |\varphi_{i\varsigma}^{(0)}\rangle\langle\varphi_{i\varsigma}^{(0)}| \tag{2.126}$$

is the projector onto the subspace of virtual KS orbitals. Notice that because of the projector Eq. (5.10) is actually a set of N_{el} coupled differential equations. Also notice that Eq. (5.10) does not involve the virtual KS orbitals, and this is its major advantage.
In the adiabatic approximation both the orbitals and f_{xc} in (5.10) lose their frequency dependence. The equations are nonetheless self-consistent since $H^{(1)}$ involves $\rho^{(1)}$. There is a set of N_{el} LR orbitals $\{\phi^I\}$ for each solution I of (5.10) (a set for each electronic state). The LR orbitals are orthogonal to the ground-state KS orbitals (we now drop the superscripts (0) and (1)):

$$\langle\phi_{i\varsigma}^I|\varphi_{j\varsigma}\rangle = 0 \tag{2.127}$$

and can be written as a linear combination of virtual KS orbitals

$$\phi_{i\varsigma}(\mathbf{r}) = \sum_a c_{ia\varsigma}^I \varphi_{a\varsigma}(\mathbf{r})\,, \tag{2.128}$$

with

$$c_{ia\varsigma}^I = \langle\varphi_{a\varsigma}|\phi_{i\varsigma}\rangle \tag{2.129}$$

The AMEW expansion can also be recovered within this formalism [9]:

$$|\psi_I\rangle = \sum_i^N \sum_\varsigma (\hat{r}_{i\varsigma}^I)^\dagger \hat{a}_{i\varsigma}|\psi_0\rangle\,, \tag{2.130}$$

here $(\hat{r}_{i\varsigma}^I)^\dagger$ is the creation operator for LR orbitals. It can be expressed as:

$$(\hat{r}^I_{i\varsigma})^\dagger = \sum_a^N c^I_{ia\varsigma}\hat{a}^\dagger_{a\varsigma}\,. \tag{2.131}$$

The Sternheimer approach has the clear advantage of involving only occupied orbitals – with no sums over virtual orbitals, as is the case in the Casida approach – making it computationally more efficient than Casida's method in most applications.

2.3.4 Spin-Orbit Coupling

In this section we introduce the Spin-orbit coupling operator

$$\begin{aligned} H^{SO}_{1el} &= \frac{\alpha^2}{2}\left[\sum_{\gamma=1}^{N_\gamma}\sum_{i=1}^{N_{el}} Z_\gamma\left(\frac{\mathbf{r}_{i\gamma}}{r^3_{i\gamma}}\times\mathbf{p}_i\right)\cdot\mathbf{s}_i\right] = \frac{\alpha^2}{2}\left[\sum_{\gamma=1}^{N_\gamma}\sum_{i=1}^{N_{el}} Z_\gamma\frac{1}{r^3_{i\gamma}}(\mathbf{l}_{i\gamma}\cdot\mathbf{s}_i)\right] \\ &= \frac{\alpha^2}{2}\sum_{\gamma=1}^{N_\gamma} Z_\gamma\left(\sum_{i=1}^{N_{el}} h_\gamma(i)\right). \end{aligned} \tag{2.132}$$

where α is the fine structure constant, which is defined as $\alpha = \frac{e^2}{4\pi\epsilon_0\hbar c}$ and as $\alpha = c^{-1}$ in atomic units. In this work we will be concerned with the one-electron spin-orbit operator only (see appendix A for information about two-electron SOC operator). This operator is part of a molecular Hamiltonian (it is simply added to the usual, non-relativistic molecular Hamiltonian), so the observable corresponding to it is also energy. SOC, as with other relativistic effects, tends to be larger for atoms and molecules containing heavy atoms. In fact, although this not the only factor determining the magnitude of SOC, it increases with approximately Z^2 in atoms [44].

Spin-orbit coupling is a relativistic effect that can be shown to be present in the Dirac equation for the electron. The Dirac equation describes the electron both quantum-mechanically and relativistically. It has a structure similar to that of the Schrödinger equation, and with the right definitions it can be written exactly like the SE:

$$H\psi = i\hbar\frac{\partial\psi}{\partial t}\,. \tag{2.133}$$

However, ψ is not a scalar, but a four-component "vector"[8] (the Dirac spinor or 4-spinor), instead of a wavefunction. The Hamiltonian for the Dirac equation describes an electron in an

[8] Technically speaking, it is a spinor, a mathematical object that is much like a vector, but that transforms differently under certain operations (such as rotations).

electromagnetic field and is defined as:

$$H^D = c\boldsymbol{\alpha}\cdot(\mathbf{p}+e\mathbf{A})+\beta mc^2 - e\phi\,, \tag{2.134}$$

where:

$$\beta = \begin{pmatrix} I_2 & 0_2 \\ 0_2 & -I_2 \end{pmatrix}, \tag{2.135}$$

with I_2 and 0_2 the 2-by-2 identity and null matrices, respectively. Also:

$$\boldsymbol{\alpha} = (\alpha_x, \alpha_y, \alpha_z),\ \alpha_k = \begin{pmatrix} 0_2 & \sigma_k \\ \sigma_k & 0_2 \end{pmatrix}; \tag{2.136}$$

where σ_k are the Pauli matrices:

$$\sigma_x = \begin{pmatrix} 0 & 1 \\ 1 & 0 \end{pmatrix}, \sigma_y = \begin{pmatrix} 0 & -i \\ i & 0 \end{pmatrix}, \sigma_z = \begin{pmatrix} 1 & 0 \\ 0 & -1 \end{pmatrix}. \tag{2.137}$$

A and ϕ are the vector and scalar electromagnetic potentials respectively, and e is the elementary charge. The canonical momentum **p**, and the Hamiltonian can be quantized using the usual rules:

$$\mathbf{p} \rightarrow -i\hbar\nabla\,, \tag{2.138}$$

$$H \rightarrow i\hbar\frac{\partial}{\partial t}\,, \tag{2.139}$$

notice however, that unlike in the Schrödinger Equation, **p** does not appear as $\mathbf{p}^2$, which means that the Dirac equation features only first-derivatives (with respect to time and space coordinates, a requirement for it to be Lorentz invariant [45, section 4.3]). In the case where

only an electrostatic potential ($V = -\frac{Z}{||\boldsymbol{r}||}$) is present ($\mathbf{A} = \mathbf{0}$), we have:

$$H^D = c\boldsymbol{\alpha} \cdot \mathbf{p} + \beta mc^2 + V \,. \tag{2.140}$$

Moreover, if the Hamiltonian is not time-dependent, a time-independent equation can be defined (through the separation of time and space variables):

$$H^D \psi = E\psi \,. \tag{2.141}$$

The Dirac equation can also be written in terms of large and small components (known as the 2-spinor form). In the time-independent case, with an electrostatic potential only, this gives:

$$\begin{pmatrix} V - E + mc^2 & c(\boldsymbol{\sigma} \cdot \mathbf{p}) \\ c(\boldsymbol{\sigma} \cdot \mathbf{p}) & V - E - mc^2 \end{pmatrix} \begin{pmatrix} \psi^L \\ \psi^S \end{pmatrix} = \begin{pmatrix} 0 \\ 0 \end{pmatrix} , \tag{2.142}$$

a set of two coupled equations. Notice that what makes these equations coupled is the fact that in equation (2.140) the α_k are anti-diagonal matrices[9], whereas β is a diagonal matrix (when both are seen as 2-by-2 matrices), i.e (2.140) is not diagonal. Here ψ_L and ψ_S are both two 2-spinors (2 components each). The labels L and S stand for large and small, respectively. The reason for this is that in many situations (but not all), ψ_S is small compared to ψ_L. It is also possible to define a new Hamiltonian, by subtracting the rest energy (mc^2) from H:

$$H' = H - mc^2 I_4 \,, \tag{2.143}$$

this means the energy levels of the system will be offset, but the new Hamiltonian is no less meaningful than the original one since the differences between energy levels are the observables. The equation defined with H' can also be written in 2-spinor form[10]:

$$\begin{pmatrix} V - E & c(\boldsymbol{\sigma} \cdot \mathbf{p}) \\ c(\boldsymbol{\sigma} \cdot \mathbf{p}) & V - E - 2mc^2 \end{pmatrix} \begin{pmatrix} \psi^L \\ \psi^S \end{pmatrix} = \begin{pmatrix} 0 \\ 0 \end{pmatrix} . \tag{2.144}$$

[9] Here Dirac equation has been written in what is called the "standard representation", and in other representations the α_k matrices need not be diagonal, but these equations are coupled anyway.

[10] In case a magnetic field is also present, we have $(\mathbf{p} + e\mathbf{A}) = \boldsymbol{\pi}$, $\mathbf{A} \neq 0$, such that $\mathbf{p} \neq \boldsymbol{\pi}$; where $\boldsymbol{\pi}$ is the mechanical momentum. Equation (2.144) is written in the same form, except $\mathbf{p}$ is replaced by $\boldsymbol{\pi}$.

It is also worth mentioning that the 2-spinor Dirac equation is strictly equivalent to the 4-spinor form, but it is more compact and it is also the starting point for the derivations of certain important approximations, because the small component tends to zero in the non-relativistic limit (as $c \to \infty$)[45, page 49][46, page 176].

Equation (2.144) can be reworked to give an equation that features ψ^L only, starting with solving for ψ^S in the lower equation:

$$c(\boldsymbol{\sigma}\cdot\mathbf{p})\psi^L + (V - E - 2mc^2)\psi^S = 0 \tag{2.145}$$

$$\Rightarrow \frac{c(\boldsymbol{\sigma}\cdot\mathbf{p})}{(E - V + 2mc^2)}\psi^L = c(\boldsymbol{\sigma}\cdot\mathbf{p})\frac{1}{2mc^2}\frac{1}{\left(1 - \frac{V-E}{2mc^2}\right)}\psi^L = \psi^S\,. \tag{2.146}$$

Notice that we can only do this last step if $(E - V + 2mc^2) \neq 0$; if we admit that $V < 0$ because it corresponds to the Coulomb interaction between a positively charged nucleus and an electron, then the condition is fulfilled for $E > 2mc^2$, in other words no negative energy solutions are admitted. Substituting the expression for ψ_S obtained in equation (2.146) into the top equation of (2.144):

$$(V - E)\psi^L + \frac{1}{2m}(\boldsymbol{\sigma}\cdot\mathbf{p})\left(1 - \frac{V-E}{2mc^2}\right)^{-1}(\boldsymbol{\sigma}\cdot\mathbf{p})\psi^L = 0 \tag{2.147}$$

and defining

$$\left(1 - \frac{V-E}{2mc^2}\right)^{-1} = K(E,\mathbf{r})\,, \tag{2.148}$$

we obtain:

$$(V - E)\psi^L + \frac{1}{2m}(\boldsymbol{\sigma}\cdot\mathbf{p})K(E,\mathbf{r})(\boldsymbol{\sigma}\cdot\mathbf{p})\psi^L = 0\,. \tag{2.149}$$

This is called the "unnormalized elimination of the small component"(UESC). The term "unnormalized" comes from the fact that ψ^L is not normalized. Indeed, the normalization

condition reads: $\int \mathrm{d}\mathbf{r}\ \left|\psi^L\right| \neq \int \mathrm{d}\mathbf{r}\ \left|\psi^L\right| + \left|\psi^S\right| = 1$[11]. Now, recognizing that $K(E,\mathbf{r})$ can be written as a geometric series [12] :

$$\frac{1}{1-\frac{V-E}{2mc^2}} = 1 + \frac{V-E}{2mc^2} + \frac{(V-E)^2}{4m^2c^4} + \dots , \tag{2.151}$$

substituting this into the previous equation leads to:

$$\begin{aligned}\Big[V + \frac{1}{2m}(\boldsymbol{\sigma}\cdot\mathbf{p})(\boldsymbol{\sigma}\cdot\mathbf{p}) + (\boldsymbol{\sigma}\cdot\mathbf{p})\frac{(V-E)}{4m^2c^2}(\boldsymbol{\sigma}\cdot\mathbf{p}) + \\ (\boldsymbol{\sigma}\cdot\mathbf{p})\frac{(V-E)^2}{8m^3c^4}(\boldsymbol{\sigma}\cdot\mathbf{p}) + \dots\Big]\psi^L = H^{UESC}\psi^L = E\psi^L .\end{aligned} \tag{2.152}$$

Where we have defined a new Hamiltonian H^{UESC}, which acts on ψ^L. Notice that the above is not and eigenvalue equation since H^{UESC} contains E. We will need to use the Dirac relation:

$$(\mathbf{a}\cdot\boldsymbol{\sigma})(\mathbf{b}\cdot\boldsymbol{\sigma}) = (\mathbf{a}\cdot\mathbf{b})I + \boldsymbol{\sigma}(\mathbf{a}\times\mathbf{b}) , \tag{2.153}$$

where $\mathbf{a}$ and $\mathbf{b}$ are any given vectors. Let us examine H^{UESC}:

$$\begin{aligned}H^{UESC} &= \left[V + \frac{1}{2m}(\boldsymbol{\sigma}\cdot\mathbf{p})(\boldsymbol{\sigma}\cdot\mathbf{p}) + (\boldsymbol{\sigma}\cdot\mathbf{p})\frac{(V-E)}{4m^2c^2}(\boldsymbol{\sigma}\cdot\mathbf{p}) + (\boldsymbol{\sigma}\cdot\mathbf{p})\frac{(V-E)^2}{8m^3c^4}(\boldsymbol{\sigma}\cdot\mathbf{p}) + \dots\right] \\ &= \left[V + T + (\boldsymbol{\sigma}\cdot\mathbf{p})\frac{(V-E)}{4m^2c^2}(\boldsymbol{\sigma}\cdot\mathbf{p}) + (\boldsymbol{\sigma}\cdot\mathbf{p})\frac{(V-E)^2}{8m^3c^4}(\boldsymbol{\sigma}\cdot\mathbf{p}) + \dots\right] ,\end{aligned} \tag{2.154}$$

(i) if we only take the first term of the expansion of $K(E,\mathbf{r})$ (i.e. $K(E,\mathbf{r}) = 1$, which is exact in the

[11] $\int \mathrm{d}\mathbf{r}$ means we integrate over all space.

[12] This is valid if:

$$\left|\frac{V-E}{2mc^2}\right| = \frac{|V-E|}{2mc^2} < 1 \iff |V-E| < 2mc^2 . \tag{2.150}$$

And this is not necessarily always the case; in the region close to a nucleus, the difference between the E and V might be very big indeed. This is one of the main criticisms made against this kind of approximation [45, page 356].

limit $c \to \infty$), (ii) use the Dirac relation to get:

$$H^{UESC} = (T + V)\,, \tag{2.155}$$

and (iii) then neglect the effects of a renormalization procedure on the Hamiltonian (which is equivalent to saying that $\int \mathrm{d}\mathbf{r}\,\left|\psi^S\right| = 0$) the Schrödinger equation is recovered. However, we do want to include relativistic corrections to the non-relativistic Hamiltonian. The simplest way to proceed is to truncate the series at the linear term [13]:

$$H^{UESC} = T + V + (\boldsymbol{\sigma}\cdot\mathbf{p})\frac{(V-E)}{4m^2c^2}(\boldsymbol{\sigma}\cdot\mathbf{p})\,, \tag{2.156}$$

and then to renormalize ψ_L. This procedure will yield (see appendix A):

$$\left\{T + V - \frac{1}{8m^3c^2}\mathbf{p}^4 + \frac{\hbar^2}{8m^2c^2}(\nabla^2 V) + \frac{\hbar}{4m^2c^2}\boldsymbol{\sigma}\cdot(\nabla V)\times\mathbf{p}\right\}\psi^N = \quad H^{Pauli}\psi^N = E\psi^N\,, \tag{2.157}$$

which is an eigenvalue equation with the Pauli Hamiltonian. The first two terms of H^{Pauli} form the usual, non-relativistic Hamiltonian. The third term is the first relativistic correction to the non-relativistic Hamiltonian and is called the mass-velocity operator. The second correction, containing $\nabla^2 V$ is called the Darwin operator and the third one is the spin-orbit coupling operator. The Pauli operator can therefore be written as:

$$H^{Pauli} = H^{Schrödinger} + H^{mass-velocity} + H^{Darwin} + H^{SO}\,, \tag{2.158}$$

and it is a non-relativistic Hamiltonian with relativistic corrections, or quasi-relativistic Hamiltonian. The spin-orbit coupling operator can also be written as:

$$H^{SO} = \frac{\hbar}{4m^2c^2}\boldsymbol{\sigma}\cdot(\nabla V)\times\mathbf{p} = \frac{\hbar}{4m^2c^2}\boldsymbol{\sigma}\cdot\left(\frac{Z}{r^3}\mathbf{r}\right)\times\mathbf{p}\,, \tag{2.159}$$

making the substitution $\hbar\boldsymbol{\sigma} = 2\mathbf{s}$ and knowing that $\mathbf{r}\times\mathbf{p} = \mathbf{l}$, we have:

[13] Notice that this term is $O(c^{-2})$, but the resulting correction will be called a first-order perturbation since we truncate the series at the first order term.

$$H^{SO} = \frac{Z}{2m^2c^2r^3}\mathbf{s}\cdot\mathbf{l}, \tag{2.160}$$

and we see that H^{SO} is called spin-orbit coupling term because it involves a scalar product of the electron spin angular momentum with its own orbital angular momentum (mixing orbital and spin degrees of freedom). Notice that this is the same operator as the one of Eq. (2.132), except there is no sum over the electrons because we started the derivation from the Dirac Hamiltonian, which refers to one electron only (see appendix B for more on this). We wish to stress that we will not solve the SE corrected with the SOC operator anywhere in this work. SOC will be treated as small perturbation, and therefore, in the spirit of first-order perturbation theory, only states of the original unperturbed Hamiltonian will be used. These states will be obtained via LR-TDDFT, and the KS orbitals will be either pure α-spin ($\langle S_z\rangle = 1/2$) or pure β-spin ($\langle S_z\rangle = -1/2$).
The many-electron version of the SOC operator is

3 Spin-orbit coupling in LR-TDDFT

This chapter is based on work which was published in 2015 [47], and it describes the implementation of particular method to calculate SOC in LR-TDDFT. This work was initiated during my Master's at EPFL and it continued during my PhD.

3.1 Introduction

The relativistic equivalent of the time-dependent Schrödinger equation involves the solution of the Dirac equation and its many-electron extensions. Relativistic quantum chemistry is an active area of research and there have been several recent reviews on the subject [48, 44, 49]. Even though generally small, relativistic corrections can have an important influence on the energy levels, orbital shapes and geometries of molecules [50].

An alternative to fully relativistic calculations is to add relativistic corrections to the standard, non-relativistic electronic structure theories. The best known corrections are the mass-velocity, Darwin and spin-orbit coupling (SOC) terms. The first two are usually called scalar relativistic effects because they do not involve vector operators. On the other hand, spin-orbit coupling acts on both angular momentum and spin, and its defining characteristic is that it mixes orbital and spin degrees of freedom, thus allowing electronic states of different multiplicities to couple. For this reason, SOC has a wide range of important effects in chemistry and physics, such as fine-structure and band splitting in molecules, semiconductors, and metals; molecular magnetism; spin transport in spinotronics and magnetoelectronics; spin quantum dots and qubits dynamics. In particular, SOC can be very important for photochemistry because it turns spin-forbidden processes, such as intersystem crossing and phosphorescence, into weakly-allowed processes.

In this respect, SOC is also particularly important in molecular dynamics because they allow for intersystem crossing (ISC) between electronic states of different spin multiplicies. The description of these processes requires the evaluation of SOC matrix elements between different electronic states, and therefore involves the use of excited states methods such as configura-

tion interaction singles (CIS) or linear-response time-dependent density functional theory (LR-TDDFT). In particular, the use of DFT and LR-TDDFT approaches is particularly well suited for the calculation of SOC in large molecular systems where a good balance between numerical efficiency and accuracy is required.

Within DFT/LR-TDDFT two main routes for the calculation of relativistic spin-orbit effects can be explored, they differ in the way the *density functionalization* of the relativistic Schrödinger equations is performed. When the Dirac equations are directly worked into the Kohn-Sham formalism one obtains the single-particle equations of relativistic DFT (KS-RDFT), which have the form of the Dirac equation with a current-dependent one-particle four-potential $v_s^{\mu}(\mathbf{r})$ [51, 52]. This approach is the starting point for certain approximations such as the quasi-relativistic "Zeroth Order Regular Approximation" (ZORA) Hamiltonian, as implemented in the Amsterdam Density Functional (ADF) program [53]. In this case, a two-component calculation is performed, and all relativistic effects are included variationally to the one-component non-relativistic calculation. As a consequence, relativistic corrections also affect observables such as bond-lengths, angles and other geometrical properties, instead of just the energy, as in the case of the perturbative treatment. However, such two-component calculations are very computationally demanding and for this reason approximate perturbative solutions to these equations have also been proposed [54].

Another option is to compute SOC perturbatively, starting from the one-component matrix element of the Breit-Pauli Hamiltonian in its many-body formulation, and then perform the *density functionalization* of the first-order relativistic corrections to the non-relativistic energies. The major challenge of this approach within TDDFT is that the matrix elements of the SOC Hamiltonian are not a simple functionals of the electronic density (by virtue of coupling two states of a many-electron system). To overcome this difficulty, we apply a method based on the so-called "auxiliary" set of many-electron wavefunctions (named AMEW) derived from LR-TDDFT quantities, which enables the calculation of exact LR-TDDFT matrix elements of any given one-body operator [8, 55, 7]. This formalism has already been successfully applied to the calculation of nonadiabatic coupling vectors (NACVs) [7, 8, 9].

In this work we present a derivation of SOC matrix elements within the AMEW formalism and describe its implementation into the CPMD program [56]. A similar approach to calculate SOCs in molecules based on Casida's [37] "singly excited configurations" has already been proposed by Russo *et al.* [57] and recently by Subotnik and co-workers [58], but these were done in an *ad hoc* fashion, following the analogies with wavefunction theory techniques such as CIS. Here, we base our implementation on the rigorous results presented in references [7, 8, 9], and investigate the use of conventional *collinear* DFT functionals and their functional derivatives in the calculation of collinear and noncollinear (spin-flip) coupling terms. Our formalism can also be easily extended, using the development in ref. [9], to the calculation of SOC between pairs of excited states, which is of paramount importance for the evaluation of ISCs events in nonadiabatic molecular dynamics calculations. In addition, in this capter we derive the working equation for the calculation of the SOC matrix elements within the both

the Casida [37] and Sternheimer [59, 60] formulations of LR-TDDFT, which can be applied to localized as well as plane wave basis set calculations.

Finally, we would like to stress that the implementation of this efficient method for the evaluation of the SOC in any DFT/LR-TDDFT-based molecular dynamics package (together with the calculation of NACVs [8, 55, 7]) will allow the "on-the-fly" calculation of both kinds of nonradiative energy transfer phenomena — internal conversion and intersystem crossing — for large systems (isolated and in condensed phase) at a good level of accuracy. Similar studies based on different electronic structure approaches have already appeared in the literature [61, 62].

3.2 Theory

The relativistic corrections to the conventional Kohn-Sham DFT equations were originally derived by Rajagopal and Callaway from quantum electrodynamics [63]. In the noncollinear case the exchange and correlation functional can be given as a functional of the electron density ρ and of the spin magnetization vector [64]

$$\boldsymbol{m}(\mathbf{r}) = \mu_B \sum_i v_i^\dagger(\mathbf{r}) \bar{\sigma} v_i(\mathbf{r}) \tag{3.1}$$

$v_i(\boldsymbol{r})$ is a two-component KS spinor (see (2.37)) $\mu_B = \hbar q/2m$ is the Bohr magneton and $\bar{\sigma} = (\sigma_x, \sigma_y, \sigma_z)$ is the vector of Pauli matrices (see section 2.3.4 for the explicit form of these matrices) [65, 66].

In the collinear local spin density approximation (LSDA), each electronic spin is oriented along a fixed quantization axis (z-axis) and the spinors can therefore be written in the spin-up (α) and spin-down (β) forms presented in equation (2.46) or in the direct product space spanned by the Hilbert space of the KS-orbitals, H_{KS} and the two-dimensional spin space H_{Spin}, as in Eq. (2.45). The spin magnetization then becomes

$$m_z(\mathbf{r}) = \mu_B \left[\sum_i^{N_\alpha} |\varphi_{i,\alpha}(\mathbf{r})|^2 - \sum_i^{N_\beta} |\varphi_{i,\beta}(\mathbf{r})|^2 \right] \tag{3.2}$$

and $m_x(\mathbf{r}) = m_y(\mathbf{r}) = 0$.

In this work we do not derive a relativistic version of the LR-TDDFT equations, which would include the SOC terms explicitly in the reference relativistic ground state KS Hamiltonian. Instead, starting from nonrelativistic KS-DFT and (standard) *collinear* LR-TDDFT equations we compute, perturbatively, the relativistic effects associated with the SOC Hamiltonian in the Breit-Pauli approximation, H^{SO}. This is achieved by a *density functionalization* of the matrix elements of H^{SO} using a LR-TDDFT-based reconstruction of the many-electron wavefunctions of the ground and excited states according to the formalism derived in [8, 55, 7]. Our approach is general and can be applied to any type of approximate SOC Hamiltonian in the perturbative

approach, including the two-component ZORA Hamiltonian [53].

A noncollinear formulation of TDDFT was developed by Shao *et al.* [67], and Wang and Ziegler [68, 69] for two-component spinors (see also the book of C. A. Ullrich [35]). Unlike collinear LR-TDDFT, noncollinear TDDFT can describe electronic transitions that involve spin-flip. These are important when evaluating SOC between states with different spin quantum number M_S, as in the case of a singlet to triplet transition between states $\frac{1}{\sqrt{2}}(|\alpha\beta\rangle - |\beta\alpha\rangle)$ ($M_S = 0$) and $|\alpha\alpha\rangle$ ($M_S = 1$) in a two-electron system. Despite progress in this field, very little has been done concerning the application of noncollinear TDDFT to molecular systems beyond the LDA approximation of the DFT functional and the TDDFT kernel. This is why we only consider the collinear form of LR-TDDFT, from which we can derive the SOC terms between singlet and triplet states that share the same M_s value (i.e. those excitations that can be reached from the ground state without spin-flip). The approximate extension of this theory to the spin-flip case will be presented and discussed in the following section.

In full, the Breit-Pauli SOC operator is composed of two parts: a one-electron term (which involves spin-own-orbit coupling only) and a two-electron term (which involves spin-own-orbit and spin-other-orbit coupling). Simply put, the one-electron term describes the interaction between the magnetic spin moment, $\boldsymbol{\mu}_{el}^{S} = -g_S \mu_B \boldsymbol{S}/\hbar$, of an electron with the magnetic moment, $\boldsymbol{\mu}_{el}^{L} = -g\mu_B \boldsymbol{L}/\hbar$, induced by its orbiting in the nuclear electrostatic field (where μ_B is the Bohr magneton, and g_S and g are dimensionless factors). Analogously, when the coupling occurs in the electric field generated by another electron we obtained the two-electron (spin-same-orbit) coupling term. Finally, the two-electron spin-other-orbit terms arise from the interaction of the spin magnetic moment of one electron with the orbital magnetic moment of a second one [48]. These two terms provide screening of the one-electron term similarly to the contributions of the nuclear-electron attraction and electron-electron repulsion interactions in the BO Hamiltonian. While for a full quantitative description of the SOC matrix elements, both the one and two matrix elements are required, the one electron contribution increases much faster with nuclear charge [44] than the two electron terms and therefore for many case the one-electron term is dominant.

The one-electron term of the Breit-Pauli Hamiltonian introduced in Eq. (2.132) can be evaluated in a formally exact way within LR-TDDFT using the AMEW method introduced in references [6, 7].

3.2.1 Computation of SOC using the AMEW

Multiplicity of the TDDFT solutions

As shown in Appendix B and in reference [37], the solution to the collinear case of Casida's equations for a closed-shell system and corresponding AMEWs can be associated to spin-adapted configurations (eigenvectors of the $\boldsymbol{S}^2$ operator) with $M_S = 0$ (i.e, the singlet $\frac{1}{\sqrt{2}}(|\alpha\beta\rangle - |\beta\alpha\rangle)$ and triplet $\frac{1}{\sqrt{2}}(|\alpha\beta\rangle + |\beta\alpha\rangle)$ configurations).

This result can be easily extended to the general case of an N-electron system; when $c^I_{ia\alpha} = c^I_{ia\beta}$ the corresponding AMEW describes a singlet, while if $c^I_{ia\alpha} = -c^I_{ia\beta}$ the AMEW represents a triplet state with $M_S = 0$ (see Appendix B).

In the Sternheimer representation (see section 2.3.3), the excited state singlet and triplet AMEW will be given by

$$|S^0_I\rangle = \sum_i^N \sum_{\varsigma=\alpha,\beta} (\hat{r}^S_{i\varsigma})^\dagger \hat{a}_{i\varsigma}|\Psi_0\rangle\,, \tag{3.3}$$

and

$$|T^0_I\rangle = \sum_i^N (\hat{r}^T_{i\alpha})^\dagger \hat{a}_{i\alpha}|\Psi_0\rangle - (\hat{r}^T_{i\beta})^\dagger \hat{a}_{i\beta}|\Psi_0\rangle\,, \tag{3.4}$$

respectively. In the definition of the states, the upper index gives the values of M_s, while the lower one labels the state number (here we used the index 1 for the states, even though the same expressions apply to any other singlet and triplet excited state). In Eq. 3.3 and 3.4 the creation operators $(\hat{r}^S_{i\varsigma})^\dagger$ and $(\hat{r}^T_{i\varsigma})^\dagger$ refer to the creation of LR-KS orbitals for the singlet and triplet calculations, respectively. In general, these two sets of LR orbitals are different. The spin of a given orbital is then assigned by multiplying it by the correct spin function to obtain the corresponding spin-orbital as in Eq. (2.45).

The "spin-flip" solution

In collinear LR-TDDFT, only the $M_S = 0$ component of each triplet state can be obtained, as $M_S = -1$ or $M_S = +1$ states require spin-flip excitations to be described. This means that only excitations that conserve the projection of spin angular momentum are allowed. A rigorous description of the spin-flip configuration would require the noncollinear LR-TDDFT formalism introduced by Ziegler and co-workers in which electrons are described by spinor wavefunctions with different spin orientations [68, 69].

However, in this work we explore a simpler solution which uses the linear-response orbitals (or coefficients in the case of Casida's formalism) obtained from a non-spin-flip triplet state calculation to build the other two triplet configurations. In other words, we represent the triplets $M_S = 1$ and $M_S = -1$ by

$$|T^{+1}_1\rangle = \sum_i^N (\hat{r}^T_{i\alpha})^\dagger \hat{a}_{i\beta}|\Psi_0\rangle \quad \text{and} \tag{3.5}$$

$$|T^{-1}_1\rangle = \sum_i^N (\hat{r}^T_{i\beta})^\dagger \hat{a}_{i\alpha}|\Psi_0\rangle\,, \tag{3.6}$$

respectively. This approach is clearly approximate, however we will leave it without a more formal justification. In the results section will show the level of accuracy of this simple procedure

by means of an application.

Evaluation of the SOC matrix elements

We now outline our strategy for the computation of the SOC matrix elements between a singlet and a triplet excited state $\langle S^0|H^{SO}|T^{M_S}\rangle$. As an example, for a system made of four electrons the matrix element $\langle S^0|H^{SO}|T^0\rangle$ will be given by the sum of sixteen matrix elements involving different AMEW and the ground state Slater determinant, while in the case of $\langle S^0|H^{SO}|T^{-1,+1}\rangle$ this number will reduce to eight.

Casida approach. In this case we have an orthonormal basis of occupied and virtual KS orbitals, and therefore the Slater-Condon rules [70] can be used to compute all of the necessary matrix elements involving AMEWs as in Eq. (5.9).

Within this framework the SOC matrix element becomes

$$\langle S^0|H^{SO}|T^{M_S}\rangle = \langle \Psi_S|H^{SO}|\Psi_T\rangle = \sum_{ij\varsigma}\sum_{ab\varsigma'} (c^S_{ia\varsigma})^* c^T_{jb\varsigma'} \langle \Psi_0|(\hat{a}^S_{i\varsigma})^\dagger \hat{a}^S_{a\varsigma} H^{SO} (\hat{a}^T_{b\varsigma'})^\dagger \hat{a}^T_{j\varsigma'}|\Psi_0\rangle\,, \quad (3.7)$$

where i,j run from 1 to N, a,b from 1 to (in principle) ∞, and $\varsigma,\varsigma' \in \{\alpha,\beta\}$. As shown in ref. [9], this type of matrix elements can be evaluated using reconstructed AMEWs.

Sternheimer approach. In the Sternheimer formalism the set of linear response orbitals for the singlet state $\{\phi^S_r(\mathbf{r})\}$ are not orthogonal to those of the triplet states $\{\phi^T_r(\mathbf{r})\}$ and therefore, in contrast to the Casida's formalism, we cannot use the Slater-Condon rules for calculating matrix elements of Slater Determinants. Instead, we require the more general Löwdin's rule [71]

$$\langle \Psi_S| \sum_{i=1}^{N} \bar{h}^{SO}(i)|\Psi_T\rangle = (D_{SS}D_{TT})^{-1/2} \sum_{i,j}^{N} \langle v^S_i|\bar{h}^{SO}|v^T_j\rangle D_{ST}(v^S_i, v^T_j)\,, \quad (3.8)$$

where $v^S_i(\mathbf{x})$ are the spin-orbitals that generate $|\Psi_S\rangle$ and $v^T_j(\mathbf{x})$ those that generate $|\Psi_T\rangle$, D_{ST} is the determinant of the matrix S_{ST} containing the overlaps between all of the spin-orbitals

$$S_{ST} = \begin{pmatrix} \langle v^S_1|v^T_1\rangle & \langle v^S_1|v^T_2\rangle & \cdots & \langle v^S_1|v^T_N\rangle \\ \langle v^S_2|v^T_1\rangle & \langle v^S_2|v^T_2\rangle & \cdots & \langle v^S_2|v^T_N\rangle \\ \vdots & \vdots & \ddots & \vdots \\ \langle v^S_N|v^T_1\rangle & \langle v^S_N|v^T_2\rangle & \cdots & \langle v^S_N|v^T_N\rangle \end{pmatrix}, \quad (3.9)$$

and $D_{ST}(v^S_i, v^T_j)$ is the cofactor of element $[i,j]$ (i.e. $(-1)^{i+j}$ times the determinant obtained by removing the i-th row and j-th column of S_{ST}). Notice that in our case $D_{SS} = D_{TT} = 1$.

In Eq. 3.8, $\bar{h}^{SO}$ refers to the 3 dimensional vector $\frac{\alpha^2}{2}\left[\sum_{\gamma=1}^{N_\gamma}\sum_{i=1}^{N} Z_\gamma(1/r_{i\gamma}^3)\mathbf{l}_{i\gamma}\right]$ (see Eq. 2.132). More detailed information on the evaluation of Eq. 3.8 is given in Appendix C.

3.3 Numerical implementation

In section 3.2.1 we showed that, by using either the Slater or Löwdin rules, the evaluation of the one-electron SOC matrix elements we only need to compute one-electron integrals of the form

$$\langle\varphi_r|(\mathbf{r}_{i\gamma}\times\mathbf{p}_i)/|\mathbf{r}_{i\gamma}|^3|\varphi_s\rangle\cdot\langle\varsigma_r|\mathbf{s}|\varsigma_s\rangle\,, \tag{3.10}$$

where φ_i represents a generic KS or LR-KS orbital, $\{\mathbf{r}_i,\mathbf{p}_i\}$ are the electron position and momentum, $\mathbf{r}_{i\gamma}=\mathbf{r}_i-\mathbf{R}_\gamma$, $\mathbf{R}_\gamma$ is a nuclear position, and $\varsigma_r,\varsigma_s\in\{\alpha,\beta\}$. The spin part of this matrix element is easy to compute. If we choose our quantization axis to be z, then the one-electron spin operator $\mathbf{s}_i$ is a vector, whose elements act on the spin states $|\alpha\rangle=(1\,0)^T$ and $|\beta\rangle=(0\,1)^T$.

The calculation of the first factor in Eq. (3.10) is numerically more involved since it requires the evaluation of integrals of the form $\langle\varphi_1|\frac{r_y p_z}{r_{\gamma i}^3}|\varphi_2\rangle=\int d\mathbf{r}\;\varphi_1(\mathbf{r})\frac{r_y}{r_{\gamma i}^3}\frac{\partial}{\partial z}\varphi_2(\mathbf{r})$, which exhibit a very sharp divergence at $\mathbf{r}_i=\mathbf{R}_\gamma$. A real-space implementation of these matrix elements is possible, however their numerical evaluation is very inefficient (at least in a plane wave code) because it requires a very large plane wave cutoff or, equivalently, a very small real-space grid, as shown in Fig. 3.2.

A more efficient solution is to evaluate this integral in the Fourier space of the electron orbitals and density. In fact, it is simple to prove that for any (non-singular) function $A(\mathbf{r})$ with Fourier transform $\tilde{A}(\mathbf{r})$, the following transformation holds [72]

$$\boldsymbol{f}(\mathbf{R})=\int\frac{\mathbf{r}-\mathbf{R}}{|\mathbf{r}-\mathbf{R}|^3}\times\boldsymbol{A}(\mathbf{r})d\mathbf{r}\quad\xrightarrow{FT}\quad\tilde{\boldsymbol{f}}(\mathbf{G})=-4\pi i\frac{\mathbf{G}}{G^2}\times\tilde{\boldsymbol{A}}(\mathbf{G})\,. \tag{3.11}$$

Finally, the quantity $\boldsymbol{f}(\mathbf{R})$ can be calculated at the position of the nucleus γ using the relation $\boldsymbol{f}(\mathbf{R}=\mathbf{R}_\gamma)=\sum_{\mathbf{G}}\tilde{\boldsymbol{f}}(\mathbf{G})e^{-i\mathbf{G}\mathbf{R}_\gamma}$.

3.4 Applications: validation and tests

In order to validate our method and its implementation within the CPMD code [56], we have selected two small organic molecules, namely formaldehyde and acetone for which we compute SOC matrix elements for the excited states $^1(n,\pi^*)$, $^3(n,\pi^*)$ and $^3(\pi,\pi^*)$ (see Figs. 3.1). According to El-Sayed's rule [73] any spin angular momentum change must be accompanied by a change in the orbital angular momentum, so that total angular momentum is conserved. Consequently, by considering the coupling between these states we obtain one strong ($^1(n,\pi^*)$ to $^3(\pi,\pi^*)$) and one weak ($^1(n,\pi^*)$ to $^3(n,\pi^*)$) SOC matrix elements, providing a validation of the approach. Our results obtained using Eqs. (3.3), (3.4), and Eq. (3.8) are

compared with those computed with the quantum chemistry program GAMESS [74] using the Spin-Orbit Multi-Configuration Quasi-Degenerate Perturbation Theory method for the one-electron SOC operator[1]. This reference gives a high level of accuracy since it includes both static and dynamic correlation.

Table 3.1 summarizes the results obtained with our implementation using both a real-space (RS) and a reciprocal-space (GS) integration schemes for the matrix elements in Eq. (3.11), together with the GAMESS reference results.

Transitions	$\lvert\langle^1(n,\pi^*)\rvert\rvert^3(\pi,\pi^*)_0\rangle\rvert$	$\lvert\langle^1(n,\pi^*)\rvert\rvert^3(\pi,\pi^*)_{+1}\rangle\rvert$	$\lvert\langle^1(n,\pi^*)\rvert\rvert^3(\pi,\pi^*)_{-1}\rangle\rvert$	Total
Dormaldehyde (strong coupling)				
SO-GMCQDPT2	91.08	0.01	0.01	91.08
LR-TDDFT/PBE (l)	92.96	0.00	0.01	92.97
LR-TDDFT/PBE (h)	101.67	0.01	0.01	101.67
Acetone (strong coupling)				
SO-GMCQDPT2	90.95	0.01	0.01	90.95
LR-TDDFT/PBE (l)	85.46	0.00	0.00	85.42
LR-TDDFT/PBE (h)	97.51	0.00	0.00	97.51
Transitions	$\lvert\langle^1(n,\pi^*)\rvert\rvert^3(n,\pi^*)_0\rangle\rvert$	$\lvert\langle^1(n,\pi^*)\rvert\rvert^3(n,\pi^*)_{+1}\rangle\rvert$	$\lvert\langle^1(n,\pi^*)\rvert\rvert^3(n,\pi^*)_{-1}\rangle\rvert$	Total
Formaldehyde (weak coupling)				
SO-GMCQDPT2	0.00	0.00	0.00	0.00
LR-TDDFT/PBE (l)	0.00	0.00	0.00	0.00
Acetone (weak coupling)				
SO-GMCQDPT2	0.00	0.00	0.00	0.00
LR-TDDFT/PBE (l)	0.01	0.00	0.00	0.00

Table 3.1 – Absolute values of SOCs for formaldehyde and acetone

Absolute values of SOCs for formaldehyde and acetone computed for two pairs of weakly and strongly coupled states. All quantities are in units of cm^{-1}.The total SOC coupling (last column) is given by the squared root of the sum of the squared components. The LR-TDDFT/PBE are performed with the CPMD software using plane wave cutoff of 70 Ry (l) and 300 Ry (h). $\langle^1(S)\rvert\rvert^3(T)_0\rangle$ stands for $\langle^1(S)\rvert H^{SO}\rvert^3(T)_n\rangle$, with $n \in \{-1,0,1\}$.

All the spin-restricted CPMD calculations were performed in gas phase with a plane-wave cutoff of 300 Ry, a box of 12 Å × 12 Å × 12 Å, the PBE exchange-correlation functional, and norm-conserving Martins-Troullier pseudopotentials. The GAMESS calculations were performed with a cc-pVDZ basis set and (8/7) active space for formaldehyde and (6/6) for acetone (see Fig. 3.1).

As discussed above, SOC integrals of the form given in Eq. 3.11 can be evaluated either in real space or in reciprocal space. However, due to divergencies at the positions of the nuclei, the calculation in real space requires a real space grid with an ultra-fine mesh, which corresponds to a very large plane wave cutoff value (> 500 Ry). On the other hand, as shown in Fig 3.2 the calculation of the SOCs converges smoothly in reciprocal space, and, for the systems studied

[1] Perturbation theory calculation based on a wavefunction obtained from a complete-active space multi-configuration self-consistent field calculation (CASSCF).

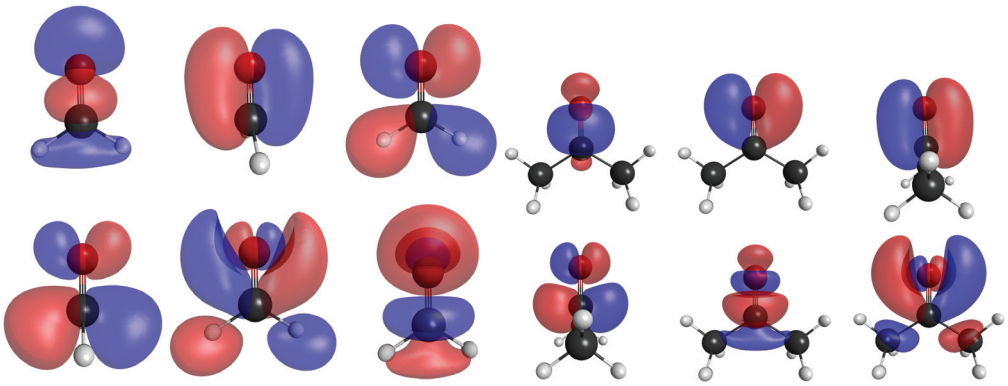

Figure 3.1 – Active space orbitals used in the CASSCF calculation for formaldehyde and acetone.
Formaldehyde, right panel. From the right to left, top to bottom: HOMO-3, HOMO-2, HOMO-1, HOMO; (bottom): LUMO, LUMO+1, LUMO+2. The corresponding DFT orbitals are undistinguishable from the CASSCF ones. **Acetone, left panel**. From the right to left, top to bottom: HOMO-2, HOMO-1, HOMO; (bottom): LUMO, LUMO+1, LUMO+2. The corresponding DFT orbitals are undistinguishable from the CASSCF ones.

in this work, a plane wave cutoff between 90 and 100 Ry is sufficient for achieving convergence; a value which is only slightly larger than the one required to converge the energy.

3.4.1 Validation of the "spin-flip" calculations

To test the accuracy of the SOC calculation for spin-flip configurations using standard collinear LR-TDDFT, we have designed the following numerical experiment. For symmetry reasons, when the principal axis of the formaldehyde molecule is oriented along the z-axis, only the SOC matrix element between the states $|S_1^0\rangle$ and $|T_1^0\rangle$ is non-zero. This transition does not require a spin-flip and therefore we expect our method to be in good agreement with the benchmark results. However, by performing a 90° anticlockwise rotation of the Cartesian reference system around the y-axis (which corresponds to the mapping $x \to z'$, $y \to y'$, $z \to -x'$), while keeping the molecule fixed in space (passive rotation), we achieved a rotation of the spin quantization axis from the z to the $-x$ direction. Introducing the corresponding rotation matrix

$$U_y^{\pi/2} = \exp\left(-i\frac{\bar{\sigma}\cdot\hat{\boldsymbol{n}}(\pi/2)}{2}\right) = \begin{pmatrix} \cos(\pi/4) & \sin(\pi/4) \\ -\sin(\pi/4) & \cos(\pi/4) \end{pmatrix} \tag{3.12}$$

we get $\sigma'_y = U_y^{\pi/2}.\sigma_y.(U_y^{\pi/2})^{-1}$, where $\hat{\boldsymbol{n}} = (0,1,0)$ and $\bar{\sigma} = (\sigma_x, \sigma_y, \sigma_z)$.

The same SOC matrix elements should also arise from a numerical calculation in which it is the molecule that is rotated (in the opposite sense) while keeping the Cartesian axis still (active rotation). However, it is important to note that in this case the spin-flip contributions will results from the direct evaluation of the terms in Eq. (3.5) and Eq. (3.6) and not from simple geometrical arguments as when the passive rotation was applied. From a comparison of the two results, the geometrical (passive rotation) and the numerical (active rotation), we

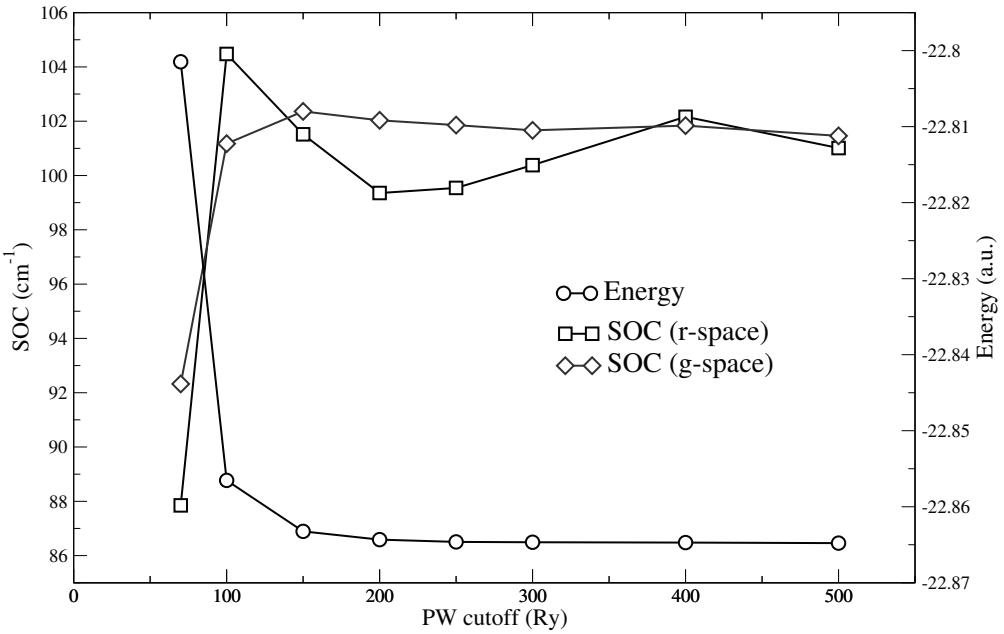

Figure 3.2 – SOC vs. Cutoff.

Graph showing absolute value of $\langle {}^1(n,\pi^*)|H^{SO}|{}^3(\pi,\pi^*)_0\rangle$ for formaldehyde versus plane-wave cutoff in Rydberg. Squares and diamonds represent the results obtained using the real-space and g-space integrator, respectively. The total energy of the system (circles) is also plotted as a function of the cutoff value (righthand side axis).

can assess the quality of the spin-flip calculation using the standard collinear LR-TDDFT approach. The values reported in Table II show the surprisingly good agreement between the two approaches, also when compared with the reference SO-GMCQDPT2 results.

We can therefore conclude that, at least for the case of simple molecular system, the collinear TDDFT formalism provides very good results for SOC matrix elements between states with different M_S values connected by spin-flip transitions. However, if this agreement also holds in the case of more complex compounds, especially those containing heavier elements is not predictable and will require further investigation.

3.4.2 Validation of the PP calculation

In this section we discuss the implications of the use of pseudopotentials (PP) for the calculation of SOCs. In electronic structure calculations with plane waves, it is a common practice to divide electrons into core electrons (with large binding energy) and valence electrons (with low-binding energy). The advantage of this separation is that the core electrons can be “frozen” in their atomic configuration while only valence and virtual orbitals are used to describe chemical modifications, including electronic excitations. In this work we make use of norm-conserving PP generated according to the Martins-Troullier scheme [75], with the possibility to include scalar-relativistic corrections. As shown in Fig. 3.3 for the case of the valence orbitals

Transition	$\lvert\langle^1(n,\pi^*)\rvert\rvert^3(\pi,\pi^*)_0\rangle\rvert$	$\lvert\langle^1(n,\pi^*)\rvert\rvert^3(\pi,\pi^*)_{+1}\rangle\rvert$	$\lvert\langle^1(n,\pi^*)\rvert\rvert^3(\pi,\pi^*)_{-1}\rangle\rvert$	Total
Formaldehyde (strong coupling)				
SO-GMCQDPT2	0.00	64.41	64.41	91.08
LR-TDDFT/PBE-SF (l)	0.12	65.53	65.53	92.68
LR-TDDFT/PBE-SF (h)	0.01	71.85	71.85	101.61
LR-TDDFT/PBE-GE (l)	0.01	65.57	65.57	92.72
LR-TDDFT/PBE-GE (h)	0.01	72.11	72.11	101.97

Table 3.2 – Absolute values of SOCs for formaldehyde

Absolute values of SOCs for formaldehyde computed for a pair of strongly coupled singlet to triplet transitions. All quantities are in units of cm^{-1} (Abbreviations are defined in Table I). The TDDFT/PBE results obtained geometrically through a (passive) rotation of the Cartesian axes are labelled by "-GE", while the ones obtained using the approximated spin-flip approach are labelled with "-SF". ((l) and (h) have the same meaning as in Table I.)

of formaldehyde, these type of PPs reproduce very accurately the KS orbitals of the valence electrons even in the region close to the nuclei. Therefore, when considering SOC matrix elements between singlet and triplet transitions involving valence KS orbitals (like in the case of the (n,π^*) and (π,π^*) transitions in formaldehyde and acetone) we obtained accurate values using the Breit-Pauli Hamiltonian of Eq. (2.132), without empirical reparameterization of the effective nuclear charges [76]. Fig. 3.3 shows cuts along a plane perpendicular to the C=O bond of formaldehyde and passing through the Oxygen atom of the KS-HOMO orbital (right hand side) and the functions $f_{xy}(\boldsymbol{r}';\boldsymbol{R}=\boldsymbol{R}_O)=\psi^*_H(\mathbf{r}')\frac{(\mathbf{r}'_x-\mathbf{R}_x)\mathbf{p}_y}{|\mathbf{R}-\mathbf{r}'|^3}\psi_{\mathbf{H-1}}(\mathbf{r}')$ and $f_{yx}(\boldsymbol{r}';\boldsymbol{R}_O)$. The agreement between the all-electron values (black lines) and the PP values (red lines) is very good especially in the region of the atomic nucleus (at distance equal to zero), where the SOC integrals are evaluated (left hand side of Eq. (3.11)). The SOC interaction between core and valence electrons can also be taken into account using a sum of Coulomb and exchange-type operators [77].

Finally, there may be situations in which SOC matrix elements involving pseudo-orbitals of the core become important. In this case, since their amplitude in the proximity of the nuclei are 'artificially' small, the errors in the evaluation of the matrix elements of the Breit-Pauli Hamiltonian can become very large. To overcome these difficulties in both plane wave but also localized basis set calculations, several model spin-orbit coupling operators were developed [78, 79, 80]. A discussion on these approximate schemes is however beyond the scope of this chapter.

3.4.3 Two-electron SOC

As previously stated, the one-electron SOC term tends to be dominant. This however, is especially true for heavier atoms because the one-electron term scales as $\sim Z^2$ [44]. We used our SO-MCQDPT reference method to calculate the coupling value for the strong-coupling states of formaldehyde including both SOC terms, and obtained a total SOC of $56.85 cm^{-1}$.

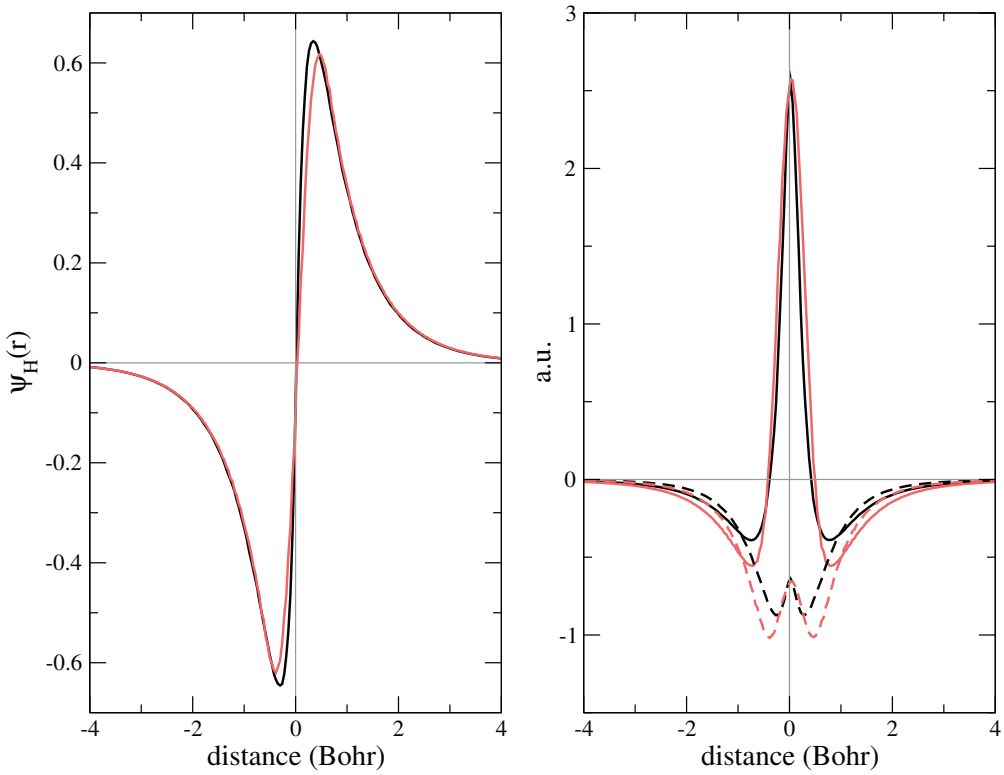

Figure 3.3 – One dimensional cut of the KS-HOMO orbital

Left: One dimensional cut of the KS-HOMO orbital along a line passing through the Oxygen atom of formaldehyde and perpendicular to the *C*=*O* bond. Right: One dimensional cut along the same line for the quantities f_{xy} (solid lines) and f_{yx} (dashed lines) in Eq. (3.11) for $f_{xy}(\boldsymbol{r}';\boldsymbol{R}_O) = \psi^*_H(\mathbf{r}')\frac{(\mathbf{r}'_\mathbf{x}-\mathbf{R_x})\mathbf{p_y}}{|\mathbf{R}-\mathbf{r}'|^3}\psi_{\mathbf{H-1}}(\mathbf{r}')$. The curves obtained from PP-calculation at 100 Ry (red) is in very good agreement with the all-electron calculations at 1800 Ry (black).

This means that the two-electron term has an absolute value of 34.23cm^{-1} (the one-electron and two-electron terms always have opposite signs). Although the two electron term is not negligible, it does show that the one-electron SOC is dominant, even in the case of this organic molecule. It is worth noting that even though the AMEW method does not allows us to calculate matrix elements of two-electron operators, a possible solution in this particular case, would be to use effective one-electron SOC operators (using an effective nuclear charge, for example), as has been done elsewhere [76, **?**]. Alternatively, finding a way to rigorously calculate two-body quantities within LR-TDDFT presents an interesting, if challenging, research path.

We also point out that we used the program ADF [81] in order to obtain the total (ZORA-Hamiltonian) perturbative SOC for the same states of formaldehyde and obtained 57.39cm^{-1}. This shows a reassuring coherence between the methods used to calculate SOC.

3.5 Discussion and conclusions

In this chapter we have described a rigorous derivation of spin-orbit coupling matrix elements within LR-TDDFT. Our approach is based on the use of the Breit-Pauli Hamiltonian as a perturbation to a standard, non-relativistic, LR-TDDFT calculation of the excitation energies and corresponding KS orbital transitions. The Tamm-Dancoff approximation was assumed throughout the derivation (and in the calculations) even if its extension to the full LR-TDDFT framework is straightforward. The SOC matrix elements are evaluated using the AMEWs introduced in references [6, 7], which have already been applied in the calculation of Tully's surface hopping couplings, and nonadiabatic coupling vectors. We presented an implementation of the numerical calculation of the SOCs in both Casida's [37] and Sternheimer's [59] formulation of LR-TDDFT within the framework of pseudopotential-based calculations with a plane wave basis set. However, the same working equations can also be applied in the case of all-electron calculations using localized basis sets.

Our derivation is based on the collinear formulation of DFT and LR-TDDFT, which does not allow for transitions involving spin-flip. To overcome this, a derivation of the SOC matrix elements in the noncollinear formalism of LR-TDDFT is required, but this was beyond the scope of the present work. However we have shown that using the same linear response orbitals computed for a $S_1^0 \rightarrow T_1^0$ transition it is possible to obtain accurate SOC values also for the "missing transitions" ($S_1^0 \rightarrow T_1^{-1}$ and $S_1^0 \rightarrow T_1^1$), using collinear TDDFT and standard (GGA) functionals and corresponding adiabatic TDDFT kernels. The quality of these calculations was assessed using geometrical arguments that allow us to obtain exact values for SOC matrix elements involving spin-flip transitions starting from those allowed in collinear LR-TDDFT. The agreement of our results, also in comparison with SO-GMCQDPT2 benchmark calculations, is in general very good, especially if we consider the fact that we are computing SOC of organic molecules which are of the order of 0.01 eV.

We have implemented the calculation of the SOC matrix elements in the pseudopotential plane wave code CPMD [56] using the Sternheimer representation of LR-TDDFT . However, a full description of the implementation in the Casida formalism is also presented and discussed in the appendices. We found out that a good accuracy is achieved using a reciprocal space integration of the $1/r^3$ term of the Breit-Pauli Hamiltonian. In this case we could obtain converged results for values of the plane wave cutoff that is just slightly larger than the one used in standard calculations using MT-type of PPs (80-90 Ry compared to 70 Ry for systems containing second row elements). We also noticed that, when the transitions taking part in the SOC calculation only involve (energetically) high-lying KS orbitals, the quality of their expansion in the PW basis set close to the position of the nuclei is very good, which is reflected in the accurate values of the corresponding SOCs. This was also confirmed by an all electron calculation with CPMD performed at a cutoff of 1800 Ry.

In conclusion, we have shown a rigorous derivation of the SOC matrix elements within the framework of LR-TDDFT, both in Casida's and Sternheimer's formulations. These calculations

can be easily optimized for plane wave as well as localized basis sets and provide accurate SOC values with a negligible additional computational overhead compared to standard LR-TDDFT energy calculations. This can be applied to study a wide range of interesting phenomena, such as molecular magnetism, spin transport, and spin quantum dots dynamics for quantum computing. Regarding our particular interests, we now have the capability to extend nonadiabatic on-the-fly trajectory based approaches such as Tully's TSH [24, 61, 82] and nonadiabatic Bohmian Dynamics [83, 26, 84] to the dynamical study of intersystem crossing within LR-TDDFT, which are key to understanding many important photochemical and photophysical processes.

3.6 Computational details

All the DFT/LR-TDDFT calculations were performed with the CPMD software package [56] using Martins-Troullier type pseudopontials [85, 75] and within the Tamm-Dancof approximation [38, 39]. The plane-wave energy cutoff value is given in Ry in the relevant sections (several different cutoffs were used). The size of the boxes used were 12x8x12 a.u. for formaldehyde and 12x12x12 a.u fir acetone. All geometries were optimized at the Hartree-Fock level with a 6-31G* basis set using gaussian [86].

The benchmark wavefunction-theory calculations were done with the quantum chemistry program GAMESS [74] using a cc-pVDZ basis set [87]. We began by performing a CASSCF calculation starting from orbitals obtained in a RHF calculation. The active space for the CASSCF was a (6/6) active space with three occupied orbitals and three virtual orbitals (see figures 3.1). This active space was chosen with an eye on the fact that we were looking to describe the excited states of formaldehyde and acetone, that is to say we needed to be able to describe the electronic transitions of the carbonyl group (namely $n \rightarrow \pi^*$, $\pi \rightarrow \pi^*$ and $\sigma \rightarrow \pi^*$). In order to obtain the excited states of these molecules, we performed a state-averaged CASSCF using the CASSCF results. The weights of the states were initially chosen to be equal, but then those of the states which did not interest us ($^1(\sigma,\pi^*)$ and $^3(n,\pi^*)$ and the ground-state) were brought down to a minimum by means of an iterative procedure. In the case of formaldehyde, the final weight of the ground state was 0 and those of the (σ,π^*) states were 8.8% that of any other given state. In the case of acetone the final weights for the ground-state and the (σ,π^*) states were all 0. We subsequently used these state-averaged multi-configurational wavenfunctions to perform a generalized multi-configurational quasi-degenerate second order perturbation theory calculation (G-MCQDPT2) [88] in order to account for "dynamic electronic correlation". Finally, we used these results to obtain the values of the (one-body) spin-orbit coupling matrix elements of the Breit-Pauli Hamiltonian (the last two calculation were actually performed in one run thanks to GAMESS' SO-MCQDPT [89] program, although SOC was not included in the perturbing Hamiltonian).

4 Intersystem crossing dynamics with LR-TDDFT

This chapter is based on Ref. [47].

4.1 Introduction

The interaction of light with molecules is an essential part of natural phenomena such as photosynthesis, DNA damage induced by UV light, animal vision, atmospheric chemistry and bioluminescence. This process also plays a key role in many technological applications ranging from artificial lighting and energy conversion in photovoltaic cells to polymer degradation and color tuning in the dye industry. In addition, spectroscopy is also an essential tool in many areas of the physical sciences, from analytical and physical chemistry to photophysics, photochemistry and more exotic fields like atomic and molecular astrophysics.

The thorough understanding of photophysical and photochemical phenomena requires the elucidation of the excited state structure and dynamics of the molecular system at hand. In particular, excited state dynamics is important for the understanding of the complex non-radiative relaxation that occurs immediately after light absorption. This is especially true for the case of the non-radiative phenomena that cannot be directly observed in experiments.

In photochemistry inter-system crossing (ISC) is the population transfer across electronic states of different spin-multiplicity (e.g. singlet-triplet). Because of spin-conservation rules, ISC is said to be a spin-forbidden process. Nonetheless ISC can occur because of Spin-Orbit Coupling (SOC), a relativistic effect that couples states of different spin-multiplicity. Spin-orbit coupling is large in molecules containing heavy atoms, where it usually induces phosphorescence. Inorganic dopants in organic light-emitting diodes (OLEDs) are examples of molecules where both ISC and phosphorescence are important. In fact, one of the roles of the dopant in the OLED matrix is to enhance SOC and thus make ISC events more likely, which in turn increases the population of the emitting triplet state and therefore the phosphorescence quantum yield (a technique known as triplet harvesting) [90, 91]. In lighter molecules, SOC will usually not be large enough to induce noticeable phosphorescence. Nonetheless, ISC can

play an important role in the photochemistry of such molecules, either by competing with other population transfer processes or by changing the chemical reactivity of the molecules. Examples include the photochemical hydrogen abstraction in ketones, which involves the highly reactive $^3(n,\pi^*)$ state, or the phenomenon known as delayed fluorescence, which is caused by certain molecules undergoing ISC to triplet states, thus precluding immediate fluorescence (and delaying the fluorescence of the ensemble).

The presence of ISC in a wide gamut of molecular photophysical and photochemical systems means that its accurate description is required to obtain a complete simulation of the excited states dynamics of molecular systems. In order to accomplish this, it is necessary to use techniques that go beyond the Born-Oppenheimer approximation and include nonadiabatic and SOC effects. Recently, there have been some interesting developments in this direction. Within the trajectory-based approaches, Persico *et al.* have developed a trajectory surface-hopping (TSH) scheme that includes the possibility to compute ISC transitions using a semi-empirical models for the electronic structure [92], while Rajak and Maiti have explored the possibility of interfacing density functional theory (optimized for different spin states) with a Landau-Zener based surface hopping algorithm [93]. Finally, both the groups of González [82, 94] and Thiel [95] have recently developed interesting wavefunction-based approaches that include the calculation of ISC *on-the-fly*. In the quantum dynamics community, there have also been efforts to include ISC effects into the wavepacket dynamics on pre-computed PESs (singlets and triplets) along a subset of selected vibrational modes [96, 97]. In this case, the SOC matrix elements were computed at DFT/TDDFT level using the perturbative approach developed by Wang and Ziegler [53, 54] and included into the dynamics in the same manner as the nonadiabatic coupling terms [97]. On the other hand, in their study of the photophysics of the SO_2 molecule Xie *et. al.* [98] applied quantum dynamics in the unconstrained nuclear configuration space, restricting however, their investigation to a single electronic triplet state.

Here we report the development, implementation and validation of a Linear-Response TDDFT-based (LR-TDDFT-based) nonadiabatic molecular dynamics method capable of describing ISC processes *on-the-fly* in relatively large molecular systems (made of up to several hundreds of atoms) in both gas and condensed phases exploiting periodic boundary conditions. Our method is fully integrated in the CPMD software package [56], and makes use of the TSH nonadiabatic dynamics module [6] together with the capability of computing SOC within LR-TDDFT [47]. This implementation has the advantage of bringing full consistency to the calculations, since all necessary electronic structure quantities required in the TSH dynamics (including nonadiabatic and spin-orbit couplings) are computed using the same code and at the same level of theory, namely LR-TDDFT. Moreover, this implementation can also be combined with a Quantum Mechanics/Molecular Mechanics (QM/MM) coupling interface [99, 100], which offers the possibility of studying ISC events in a realistic (explicit) solvent environment described at a MM level, opening new opportunities for the understanding of solvent induced effects.

We tested our new TSH scheme on the photophysics of sulfur dioxide (SO_2), which presents

the advantage of being a small molecule while still having a relatively large SOC and, therefore, a rich photophysics with both nonadiabatic transitions (NT) and ISC [101, 102, 103]. Moreover, at high pressure or low temperatures, sulfur dioxide also exists in liquid phase, as it is the case in certain moons of the planet Jupiter (Europa, Ganymede, and Callisto) and in the chemical industry (sulfur dioxide is usually stored and transported as liquid, and is used in the mining industry, in paper mills, in the production of sulfuric acid and as a refrigerant liquid, for example). The principal aim of this study is twofold: first, the validation of our approach through the comparison of our results with data obtained from other *ab-initio* simulations and from experiments, and second, the investigation of the effects induced by the surrounding molecules on the strength of the SOC matrix elements as well as on topology and relative position of the singlet and triplet PESs. Both these effects can clearly have an important influence on the observed ISC rates.

4.2 Theory

4.2.1 Nonadiabatic dynamics with intersystem crossings

Usually, nonadiabatic molecular dynamics simulations deal with transitions among states with the same spin-multiplicity. The most efficient algorithms for the calculation of this dynamics rest on trajectory-based solutions of the time-dependent Schrödinger equation for the molecular Hamiltonian (see section 2.1), in which case potential energy surfaces, nuclear forces, and nonadiabatic couplings are computed *on-the-fly* [25, 104, 105, 106]. Several attempts to combine nonadiabatic dynamics with intersystem crossing (ISC) have recently been made [82, 102, 107, 62]. However, the development of efficient *on-the-fly* algorithms is hampered by the computation costs associated with the calculation of the SOC between different electronic excited states [108].

Here we present an extension of our TDDFT-based trajectory surface hopping approach for the description of nonadiabatic dynamics, which includes the possibility to simulate ISC events *on-the-fly* using the same level of theory (LR-TDDFT).

To describe SOC effects, the definition of the electronic hamiltonian must be extended to include spin-orbit coupling:

$$\hat{H}_{el}^{full} = \hat{H}_{el}^{SF} + \hat{H}^{SO} \tag{4.1}$$

where $\hat{H}_{el}^{SF}$ is the spin-free (SF) electronic Hamiltonian (see Eq. (2.9)) and $\hat{H}^{SO}$ is the Breit-Pauli one-electron SOC operator introduced in equation (2.132).
We would like to stress that the method developed in this work is independent from the level of approximation used for the calculation of the SOC matrix elements, which can be improved beyond the one-electron Breit-Pauli Hamiltonian (by including the two-electron Breit-Pauli

SOC term, or by using another Hamiltonian altogether, such as ZORA [109]).

There are two possible implementations of the TSH/ISC dynamics. In the first case, one considers the electronic states (eigenstates) associated to the full Hamiltonian of Eq. (4.1). Since $\hat{H}^{SO}$ and $\hat{S}^2$ ($\hat{S}$ is the total electronic spin of the system) do not commute, the eigenstates of $\hat{H}_{el}^{full}$ and $\hat{S}^2$ do not have simultaneous eigenstates. In other words, the dynamics would evolve in "mixed-spin" states with S depending on the molecular geometry $\boldsymbol{R}$. In this representation, named the spin-adiabatic representation [61], it would no longer make sense to speak about singlets and triplets (or higher multiplicities) or even inter-system crossing since the electronic states would be a mix between singlets and triplets. Spin-orbit coupling would also have a direct effect on the energies of the PES and therefore on the forces acting on the nuclei.

The second option is to solve for the eigenstates of the spin-free electronic Hamiltonian and to have them be eigenstates of the spin operator S^2 as well (through the use of the so-called spin-adapted configurations). In this case, the nuclear dynamics evolves on PESs with well defined spin-multiplicities and the SOCs are computed perturbatively. This information will then be used to compute the ISC probabilities through the algorithms that we will introduce in the following section. It is also important to mention that since the SOC contributions are evaluated in first-order perturbation theory, their energetic contribution does not explicitly enter in the definition of the PESs and, as a consequence, they will not directly affect the nuclear forces. Finally, the perturbative approach is compatible with the use of an unbound operator for the calculation of the SOC corrections, such as the Breit-Pauli Hamiltonian (Eq. (2.132)). Since SOC tends to be small with respect to the total state energies, this is, in principle, a reasonable approach and the corresponding representation is called spin-diabatic.

There are two main advantages to using the spin-diabatic representation. The first one is that the full electronic Hamiltonian does not need to be diagonalized. Electronic energies not including SOC (and their gradients with respect to the nuclear positions, $\boldsymbol{R}$) are readily available through the solution of the electronic Schrödinger equation as implemented in many electronic structure packages. The second advantage is that the spin-multiplicity of the electronic states are well-defined and independent of $\boldsymbol{R}$, which is useful to interpret results from a spectroscopical viewpoint. For these two reasons, we have chosen to use the spin-diabatic representation.

4.2.2 Surface-hopping dynamics with ISC

In this section we describe an extension of TSH [25] that includes the possibility of ISC between states of different spin-multiplicity. In TSH, a nuclear trajectory, denoted by $\boldsymbol{R}^{[\alpha]}(t)$ and labeled by the index α, propagated on an electronic state I, can hop to a state K of the same spin-multiplicity due to the effect of nonadiabatic couplings Ξ_{IK} (see Eq. (2.33)), as presented in section 2.2.1.
We now explore two possible extensions of TSH for the simulation of ISC, using the method explored in Chapter 3 in order to obtain values of SOC.

The first possibility is obtained through the replacement of the the spin-free Hamiltonian in Eq. (2.29) with the 'full' Hamiltonian defined in Eq. (4.1); in this way we obtain a generalized TSH equation that treats both type of transitions, nonadiabatic (spin-conserving) transitions and ISC, on the same footing. We will call this approach TSH⊗TSH. The second method, which has some numerical advantages, treats the transitions between states of different spin-multiplicities using the Landau-Zener (LZ) formula [110, 111], and we will refer to it as the TSH⊗LZ approach.

The TSH⊗TSH approach. The most straightforward way to include ISC in the nonadiabatic TSH dynamics consists in replacing in Eq. (2.29) the spin-free Hamiltonian $\hat{H}_{el}^{SF}$ with the full Hamiltonian defined in Eq. (4.1)

$$\dot{C}_K(t) = -\sum_I C_I(t)\left(iH_{IK}^{full} + \Xi_{IK}(t)\right). \tag{4.2}$$

The corresponding transition probabilities therefore become

$$p_{KI}(t, t+\delta t) = -2\int_t^{t+\delta t} \frac{Re\left[C_K(\tau)C_I^*(\tau)\Xi_{KI}(\tau)\right] - Im\left[C_K(\tau)C_I^*(\tau)H_{IK}^{full}\right]}{C_I(\tau)C_I^*(\tau)} d\tau\,. \tag{4.3}$$

Again, using the adiabatic basis for H_{el}^{SF}, these equations simplify to

$$\dot{C}_K(t) = -iC_K(t)\omega_K - \sum_I C_I(t)\Xi_{IK}(t) + iH_{IK}^{SO}(t)\,, \tag{4.4}$$

and

$$p_{KI}(t, t+\delta t) = -2\int_t^{t+\delta t} \frac{Re\left[C_K(\tau)C_I^*(\tau)\Xi_{KI}(\tau)\right] - Im\left[C_K(\tau)C^*(\tau)_I H_{IK}^{SO}\right]}{C_I(\tau)C_I^*(\tau)} d\tau\,. \tag{4.5}$$

Note that this approach can also be formulated in the spin-adiabatic representation. In this case, the dynamics of the amplitudes $C_K(t)$ will remain formally identical to the one in Eq. (2.34), with the difference that the state energies ω_K will also include a spin-dependent contribution. As a consequence, the nuclear forces will also acquire an extra term equal to $F^{SO} = -\nabla_{\mathbf{R}}\hat{H}^{SO}$.

The TSH⊗LZ approach. The evaluation of the amplitudes $C_I(t)$ using Eq. (4.4) requires, in principle, the calculation of the SOC matrix elements (SOC-ME) $H_{IK}^{SO} = \langle\psi_I|\hat{H}^{SO}|\psi_K\rangle$ at each time step of the dynamics. However, ISC events occur in the neighborhood of crossing points between surfaces of different spin-multiplicities and therefore it would be computationally advantageous to restrict the calculation of the SOC-ME to a time window centered at the ISC time (for example a crossing point between singlets and triplets, in the spin-diabatic picture). In order to best exploit this, we have designed a TSH⊗LZ scheme, in which the amplitudes

$C_I(t)$ are propagated using the 'standard' differential equation given in Eq. (2.34) (instead of the extended one of Eq. (4.4)), while the transition amplitudes are computed using Eq. (2.35) in the case of transitions between states of same spin-multiplicity, and with the LZ formula

$$p_{IK}^{LZ} = 1 - e^{-2\pi\Gamma_{IK}} , \tag{4.6}$$

with

$$\Gamma_{IK} = \frac{|\langle\psi_I|H^{SO}|\psi_K\rangle|^2}{d\omega_{ST}/dt} , \tag{4.7}$$

when the transition involves states of different spin-multiplicity. In Eq. (4.7) $\omega_{IK} = |\omega_I - \omega_K|$ is the absolute value of the energy gap between the two states evaluated in the spin-diabatic representation. An ISC occurs stochastically when at the crossing point the probability p_{IK}^{LZ} is larger than a random number generated in the interval $[0,1]$.

Finally, a word has to be said about the limitations of the spin-diabatic approach. Persico *et al.* have argued that the spin-diabatic approach, although widely used, can lead to wrong results in certain situations, namely, when a triplet interacts through SOC with more than one singlet state with appreciable (and comparable) coupling strengths. For this reason, they recommend to use, when possible, the spin-adiabatic approach. However, in complex molecular systems events of this type are rare and therefore we believe that the spin-diabatic approach can be used, as long as one is aware of its limitations. In addition, as already explained above, the use of the spin-adiabatic representation has the important drawback of needing the diagonalization of the full electronic Hamiltonian, Eq. (4.1), and the calculation of energy gradients including the SOC interaction, which are computationally very expensive operations.

4.3 Sulfur dioxide: case study

As a demonstrative example of the derived TSH⊗LZ nonadiabatic dynamics we investigate the photophysics of sulfur dioxide (SO_2) in gas and liquid phases. Light absorption by SO_2 in its first allowed state leads to a very rich cascade of processes that involve different excited singlet and triplet states. Several experimental [112] and computational [101, 102, 103, 98] studies on the photophysics of this system are already present in the literature providing us with the possibility to assess the level of accuracy of our approach.

4.3.1 Computational details

For this study we used the PBE functional [113] and a plane-wave basis set with a cutoff of 70 Ry and the Troullier-Martins norm conserving pseudo-potentials [75]. The SO_2 molecule was placed in a cubic box of 9x9x9 $Å^3$. In the gas phase calculations, periodic images were screened using the Martyna/Tuckerman algorithm [114]. For the excited-state LR-TDDFT

calculations, the Tamm-Dancoff (TDA) approximation was used [40, 60] together with the adiabatic approximation of the TDDFT kernel [37, 115].

The system was initially equilibrated in the ground state using Born-Oppenheimer (BO) dynamics, starting from the optimized geometry. The Nose-Hoover thermostat (with coupling frequency 2000 cm^{-1}) was used to keep a constant temperature of 300K.

For the study of the liquid state sulfur dioxide, 443 GAFF [116] SO_2 molecules were placed in a cubic box of 32 Å edge and equilibrated at 300K applying a constant pressure of 4 atm using classical molecular dynamics (Fig. 4.1). Periodic boundary conditions (PBC) were applied in all directions to reproduce the liquid structure and dynamics. Subsequently, one of the SO_2 molecules was selected to be treated quantum mechanically at the DFT/LR-TDDFT level of theory, while the other molecules were treated using classical molecular mechanics. The electrostatic interaction between the classical and quantum subsystems was taken into account through a range-splitting Hamiltonian as described in Ref. [100]. The QM/MM system was then equilibrated using BO dynamics using DFT/PBE as described above for the gas phase simulations.

For the nonadiabatic dynamics, we ran a total of 90 trajectories (50 in gas phase and 40 in the liquid phase) using our combined TSH⊗LZ approach. The starting configurations were taken at random from the (Boltzman) ensemble as sampled from the ground state BO dynamics. The trajectories were started in state the mixed-character S_2 singlet state, which includes some $^1B_1$ bright state character, using the velocities associated to the selected ground state frame.

The trajectories were computed with a time step of 0.121 fs while the SOC matrix element were evaluated every 4 time steps. As mentioned in the Theory section, our algorithm only requires the calculation of the SOC-ME in the neighborhood of a crossing between a singlet and triplet state. However, due to the small size of the system investigated, we decided to monitor the time-evolution of SOC-ME all along the trajectories. Finally, the ISC transition probabilities were evaluated in the vicinity of each crossing point between singlet and triplet states using Eq. (5.14). These crossing points are detected by monitoring the signs of the energy differences between the running state and all the other states of different spin-multiplicity. When a sign change is detected, it means that a crossing point occurred in the previous time-step. This implies a time uncertainty of 0.06 fs (half a time-step), which, in our system, corresponds to a root-mean-square deviation of about 0.00025 Å between the structure at which the transition probability is computed and the actual position of the crossing. This simple algorithm provides good accuracy at moderate computational cost, and can be improved by controlling the time-step as a function of the absolute value of the energy difference between the coupled states.

4.3.2 Electronic structure of SO_2

We start by assessing the performance of LR-TDDFT/PBE by computing vertical excitation spectra for the geometry optimized SO_2 structure. In Table 4.1, we compare LR-TDDFT/PBE

excitation energies for the first three singlet and triplet states with those obtained from a high level MRCI calculations and with available experimental values (obtained in gas phase).

state	excitation	symmetry	DFT/PBE	MRCI (1) [117]	MRCI (2) [98]	MRCI (3) [102]	Exp. [117]
Singlets							
S_1	$n_a \rightarrow \pi^*$	$^1B_1$	3.46	3.87	4.19	4.46	3.46
S_2	$n_b \rightarrow \pi^*$	$^1A_2$	3.82	4.17	4.61	4.85	3.95
S_3	$n_\pi \rightarrow \pi^*$	$^1B_2$	6.23	5.82	–	6.81	5.28
Triplets							
T_1	$n_a \rightarrow \pi^*$	$^3B_1$	2.44	2.94	3.33	3.65	3.20
T_2	$n_b \rightarrow \pi^*$	$^3A_2$	3.22	3.80	4.37	4.63	3.26
T_3	$n_\pi \rightarrow \pi^*$	$^3B_2$	3.30	3.64	–	4.48	–

Table 4.1 – Vertical excitation energies.

Vertical excitation energies (in eV) of the first three singlet and triplet states, at the optimized geometry. The states' characters are ordered according to out PBE/TDDFT calculations. The three different MRCI calculations were performed with different settings; for more informations we refer to the original publications.

The states were assigned an electronic character according to the main single-electron excitation contributing to the transition. The singlets S_1, S_2 and S_3 had (n_a,π^*), (n_b,π^*) and (n_π,π^*) character, respectively (see Fig4.1). The same characters in the same order apply to the triplet states as well.

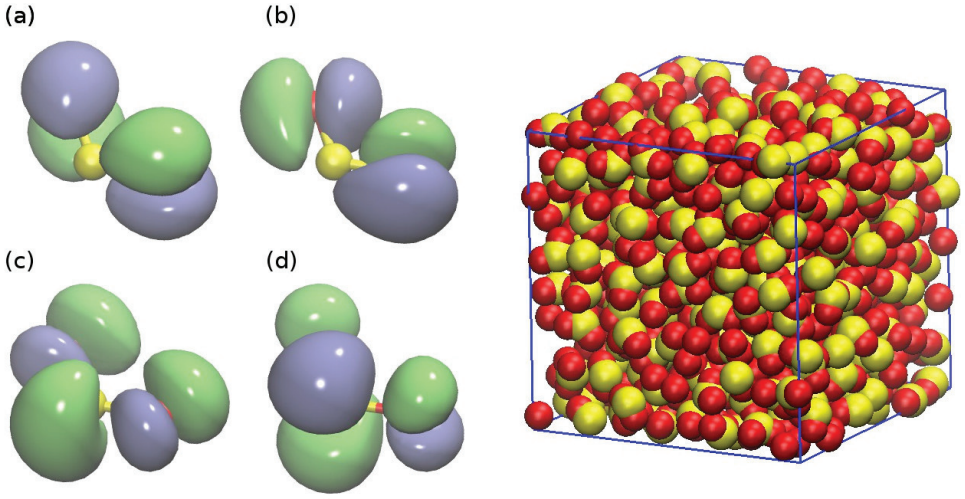

Figure 4.1 – Kohn-Sham orbitals of SO_2 and simulation box.

Kohn-Sham orbitals of SO_2 computed at the optimized geometry. (a) n_π, (b) n_b, (c) n_a and (d) π^*. Naming convention taken from [118]. (Right) Setup for the QM/MM calculation. The SO_2 molecule at the center of the box is treated at DFT/LR-TDDFT level of theory, while the remaining molecules are modeled at a classical molecular mechanics level.

Since the geometry optimization was done while enforcing C_{2v} symmetry, it is also possible to assign the symmetries B_1, A_2 and B_2 to these states. The corresponding molecular orbitals are shown in Figure 4.1. The results reported in Ref. [117] and [102] show that triplet B_2 has lower

energy than triplet A_2, whereas we and the authors of Ref. [98] find the opposite order. In experimental literature [117, 119] the $^3A_2$ state is referred to as the "second triplet", although there is no experimental evidence of the origin of a third triplet in this region of the SO_2 absorption spectrum. Evidence for $^3B_2$ comes from simulations only, so it is not possible to tell which calculation should be trusted better. Nonetheless, both experimental [117, 119] and theoretical evidence seems to point to $^3A_2$ and $^3B_2$ being very close in energy, which could explain the discrepancy. It is important to note that although the first two singlet states have well defined characters at the optimized C_{2v} geometry , this was not the case for the geometries sampled from the ground-state BO dynamics, where they had mixed character. This is in agreement with the fact that a conical intersection is found at the Franck-Condon region [117, 102, 98]

Our excited state energies are systematically red-shifted with respect to the calculations at MRCI level of theory. However, the energy difference between the states, crucial for surface hopping dynamics, are consistent. In particular, unlike what is reported in refs. [117, 102] but in accordance with the results of ref. [98], we found that at the optimized geometry, state $^3B_2$ has a higher energy than state $^3A_2$.
Since we work in the adiabatic representation (of the PESs), the electronic character of the different states (S_i or T_i) can vary during the dynamics, eventually acquiring a mixed character (especially when close to avoided crossings). Moreover, even though during the dynamics the geometries do not strictly belong to the original C_{2v} point group, we can still assign, based on the nature of the orbitals involved, the corresponding electronic character (B_1, A_2 or B_2) to the different excitations.

The first UV absorption band of SO_2 is known as Clement's band [117, 120], which upon excitation gives rise to the excited state dynamics of SO_2 that we describe in this work. From the analysis of the topology of the different energetically accessible PESs (S_1, S_2, but also T_1, T_2, and T_3) we expect a very rich dynamics characterized by NT near regions of strong nonadiabatic couplings and ISC events between singlet and triplet states. Fig. 4.2 shows two-dimensional cuts of the PESs for the states S_1, T_2, and T_3 with the corresponding crossing lines

For the sake of completeness, we also investigated the topology of S_3 or S_4 by running a number of short trajectories in these states starting from geometries sampled at the Franck-Condon (FC) region. However, in this case we could not identify any important region of strong SOC coupling with other triplet states with energy higher than T_3. In addition the large energy gap between S_2 and S_3 prevents any sizable population transfer (mediated by NT or ISC) between the manifolds of states lying below S_2 and above S_3.

For this reason, in this work we will limit our investigation to the dynamics involving the states S_1, S_2, T_1,T_2 and T_3. The number of potential NT and ISC points present in this sub-manifold of states makes this simple system an ideal candidate for testing our extended TSH⊗LZ nonadiabatic molecular dynamics scheme.

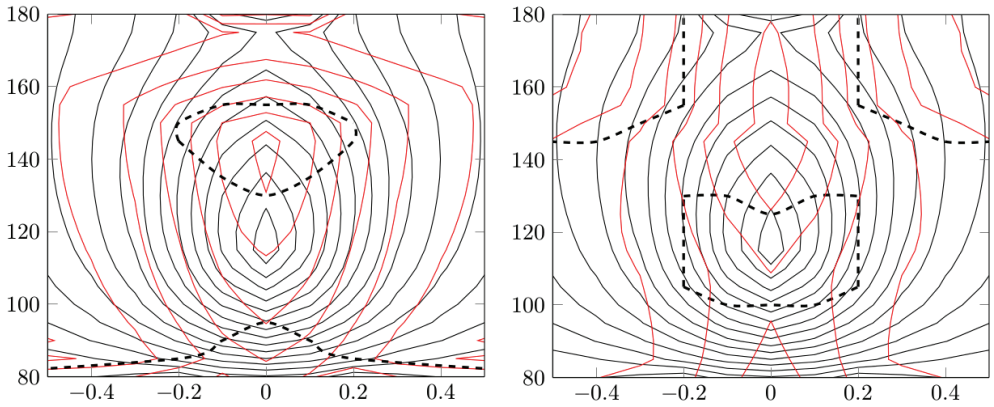

Figure 4.2 – Contour plots of PES.

Energy contour plots of the S_1 and T_2 PESs (left) and of the S_1 and T_3 PESs (right) in the plane defined by the $\angle$OSO angle (y-axes, in degrees) and the difference between the two SO bond lengths (x-axes, in Å). The dotted lines describe the crossing lines between the depicted states, and correspond therefore to the regions where ISCs are possible.

We would also like to point out that the main purpose of this work is to illustrate a development for the simulation of dynamics including ISC formulated within the framework of LR-TDDFT. It is beyond the scope of this work to investigate the approximations inherent to LR-TDDFT, which can always be systematically improved by choosing functionals from higher lying tiers of Perdew's ranking [121]. We also judged the one-electron Breit-Pauli SOC combined with the the TSH⊗LZ algorithm to be sufficiently accurate for this illustrative example on the photophysics of sulfur-dioxide, in gas and liquid phases. As mentioned above, the method developed in this work is independent from the accuracy of the SOC-ME, which can be improved, when necessary, beyond the one-electron approximation.

4.3.3 Nonadiabatic dynamics with intersystem crossings: the TSH⊗LZ algorithm

The state $^1B_1$ is responsible for the UV absorption in the Clement's band. In the Franck-Condon region these states correspond to S_1 and S_2. This means that one possible strategy for choosing the initial conditions for the dynamics, would be to distribute initial trajectories among both states as done in [102]. Another, strategy would be to populate S_2 exclusively, knowing that a conical intersection is present at the Franck-Condon region, and that any trajectory in S_2 will fall into S_1 through said intersection. In this study, we decided to start all trajectories from state S_2, which according of our calculations has the largest oscillator strength.

Figure 4.3 (upper panel) shows the energies of the different states involved in the dynamics (S_1, S_2, T_1, T_2, and T_3) in a time window ranging from 20 to 75 fs, for a typical trajectory selected from our ensemble. After around 30 fs, a region of strong nonadiabatic coupling between S_1 and S_2 is encountered, which leads to a surface hop (NT) from S_2 to S_1. This hop is due to

Tully's algorithm, as presented in Eqns. (**??**) and (5.13). This observation is consistent with the fact that a conical intersection between states $^1B_1$ and $^1A_2$ is known to exist close to the FC region [102]. The ultrafast S_2 to S_1 transition is observed in all trajectories of the ensemble, and leads to the fast decay of the S_2 population during the first 30-50 fs of dynamics (Fig. 4.4). Along the same trajectory represented in Fig. 4.3, the first ISC occurs shortly after S_1 crosses T_3 for the first time (at time $t = 43$ fs). From the analysis of the entire ensemble of trajectories we noticed that ISC can also occur, with similar frequency, between states S_1 and T_2 (although this did not occur in the example reported in Fig. 4.3). This is possible for those trajectories that explore the regions of the nuclear configuration space where S_1 and T_2 cross. Finally, at about 50 fs, we observe an avoided crossing that brings the dynamics directly from state T_3 to state T_1. This event recurs often in the trajectory ensemble and, along with the two step mechanism involving first a transition to T_2, followed by a surface hop in T_1, constitute the only population transfer mechanisms leading to the final decay into T_1 (See eq. (4.8) and Fig, 4.2).

The middle panel in Fig. 4.3 displays the calculated Landau-Zener surface hopping probabilities for an ISC to occur (Eq. (5.14)) together with the sequence of generated random numbers. We observe that the ISC event occurs when the probability peaks at around 43 fs. Other peaks appear along the trajectory, but no hops occur because at these instants of time the singlet and triplet PESs do not cross. The lower panel of Fig. 4.3 shows the time series of the two quantities involved in the calculation of the the Landau-Zener ISC probability, namely the value of the spin-orbit coupling and the derivative of the energy difference between the electronic states concerned. Interestingly, the SOC-ME values (only the SOC-ME values between states S_1 and T_3 are shown here) are overall quite small with an average value of about 77 cm^{-1} (see Table 4.2), which is not unusual for organic and inorganic molecules composed by light elements. However, variations can also be quite important, with values that range from 0 to 186 cm^{-1} in the ensemble of trajectories. This fact emphasizes the importance of frequent calculation of the SOC matrix elements between the different singlet and triplet states involved in the photophysics of this system. As expected from the analysis of Eqs. (5.14) and (5.15), the peaks in the Landau-Zener ISC probability are also due to sharp drops in the value of the derivative of the energy difference (Fig. 4.3, lower panel).

While this analysis was performed for the gas phase trajectories, the same description is also valid in the liquid phase with the only difference that the time scales for the different processes (NT and ISC) vary slightly. We will discuss this point when presenting the population dynamics for the different states.

From the analysis of the complete set of trajectories, we can derive the following kinetic model for the description of the different reaction channels that bring the system from the

photoexcited bright state S_2 to the low energy T_1 state:

$$\begin{array}{ccccc} S_2 & \xrightarrow{k_1} & S_1 & \underset{k_{-2}}{\overset{k_2}{\rightleftharpoons}} & T_2 \\ & & {\scriptstyle k_{-3}}\uparrow\downarrow{\scriptstyle k_3} & {\scriptstyle k_6}\nearrow & {\scriptstyle k_4}\downarrow \\ & & T_3 & \xrightarrow{k_5} & T_1 \end{array} \tag{4.8}$$

which shows that, despite the simplicity of the system, its photophysics is very rich and therefore it constitute a valid test for our nonadiabatic dynamics scheme.

In order to shed light on the differences between the gas phase and the liquid phase dynamics, we have analyzed the time evolution of the population of each state involved. The state population is computed as the percentage of the total number of trajectories that evolve on a given state. The upper panels of Fig. 4.4 show the time series of these populations for all singlet and triplet electronic excited states independently (left: gas phase; right: liquid), while the lower panels report the total populations of all singlet (S_1 and S_2) and triplet states (T_1, T_2, and T_3).

During the first few fs of dynamics ($\sim$ 5 fs) we observe an ultrafast exchange of the S_2 and S_1 populations due to the presence of the conical intersection between these two states in the neighborhood of the FC region. This process occurs in both gas and liquid phases, however in this last case we observe a residual population of the initial S_2 at longer times. As soon as S_1 gets populated, we observe a rise in the population of the triplet states starting from T_3 and followed by T_2 and T_1. The ISC occurs exclusively through the $S_1 \rightarrow T_2$ and the $S_1 \rightarrow T_3$ pathways, the $S_1 \rightarrow T_1$ path being excluded due to the fact that S_1 and T_1 never cross each other.

Qualitatively, the population dynamics in the gas and liquid phases are therefore very similar. However, there are important differences in the rates at which these processes occur.

Whereas in the gas phase the population of S_2 is completely depleted after 50 fs, this process is slower in the liquid phase, and a residual S_2 population persist for times longer than 400 fs. However, the major difference between the gas phase and liquid phase dynamics lies in the nature and rates of the ISC processes and of the following NTs within the family of triplet states. In gas phase, we observe a sequential population transfer from S_1 to T_3 or T_2, and then to T_1, with the population of the lowest triplet state becoming complementary to the one of S_1 at longer times. This is made possible by the very efficient $T_2 \rightarrow T_1$ population transfer. On the other hand, in the liquid phase this mechanism is slowed down, and a larger population of T_2 compared to T_1 is observed for times larger than 0.5 ps. Even more interesting is what we can learn from the dynamics of the collective triplet and singlet populations reported in Fig. 4.4 (lower panel). In fact we observe a clear slowdown of the overall ISC process in going from the gas to the liquid phase. A simple exponential fit of the first part of the dynamics gives an

intersystem crossing rate constant of $4.2\,10^{-3}$ fs^{-1} in gas phase and of $1.9\,10^{-3}$ fs^{-1} in solution; a difference of about a factor ~2.

What is the source of this difference? A possible explanation is that the SOC for the transitions $S_1 \rightarrow T_2$ and $S_1 \rightarrow T_3$ can be influenced by the presence of the surrounding molecules. To check this hypothesis, we computed the average SOC for these two transitions over the entire ensemble of gas phase and liquid phase trajectories. The results are reported in table 4.2.

	Gas phase	Liquid phase
$\langle S_1 \vert \hat{H}^{SO}_{1el} \vert T_2 \rangle$	80.05	81.05
$\langle S_1 \vert \hat{H}^{SO}_{1el} \vert T_3 \rangle$	77.40	65.92

Table 4.2 – Averaged spin-orbit coupling matrix-elements (in cm^{-1}) for the gas phase and liquid phase simulations.

We observe that the average coupling between S_1 and T_2 is practically the same in both the gas and liquid phases. On the the other hand, the S_1/T_3 SOC is, on average, larger in the gas phase than in the liquid phase. Although this is an interesting result since it proves that the solvent can have an effect on the size of the SOC-ME, the change is rather small, and thus we do not think it can explain the different kinetics observed in the two setups.

A second main difference lies in the transition frequencies between states, T_3/T_1 and T_2/T_1, which are about a factor two more frequent in gas phase than in solution. The trajectories that remain either on T_2 or T_3 can cross back to S_1, and in fact these triplet-to-singlet events occur twice as often in the liquid phase, slowing down the effective rate at which the triplet states are populated. This effect is mainly due to the 'compression' of the configuration space induced by the high pressure (see Fig. 4.5), which reduces the excursions of the trajectories in the regions where the crossings between the S_1 and T_2 states occur (gas phase trajectories can reach S_1/T_2 crossing points at angles around 80°, while these configurations are not sampled in solution). In addition, and probably most importantly, the interaction with the surrounding molecules induces an energy shift between the different PESs; decreasing, in particular, the number of NT points between states T_3/T_1 and T_2/T_1. All these effects contribute first to a slower increase of the population of the intermediate T_2 state and, subsequently, to a less efficient population transfer to T_1. In fact, as given in Eq. (4.8), the only way to populate the final state T_1 is through an NT from the other triplet states.

4.3.4 Discussion

To our knowledge, there is no direct experimental observation of ISC in the SO_2 molecule. Nevertheless, there has been strong indirect evidence for the ISC pathways [122, 123, 124, 125]. This has been explored more recently and in more detail by Wilkinson *et al.* [101]. Their work consisted in the study of the dynamics of SO_2 after excitation to the Clements band, using time-resolved photoelectron and time-resolved photoelectron-photoion spectroscopy. They

suggest that certain quadruplet excited states of the SO^+ ion, obtained through photodissociation of SO_2, can only be accessed by starting from a triplet state of the SO_2 molecule. They also point out that the lifetimes of other excited states of the ionic species (SO^+ and SO_2^+) obtained in their experiments, could be better explained if ISC does occur after excitation of SO_2 into the Clements band. This led them to strongly suggest the presence of ultrafast ISC in the dynamics of SO_2 starting from the Clements band, with an estimated ISC timescale varying between 145 to 775 fs, all of which is consistent with our results.
Our results are also similar to those obtained by the computational work of Mai *et al.* [102], with the noticeable differences that they do not observe significant population transfer to T_1 whereas we do, and that we observe a faster population of the triplet states through ISC, roughly twice as fast as what is observed in their study. Nevertheless both ISC timescales are estimated to be sub-picosecond ($\sim$ 240 fs in our case and $\sim$ 540 fs in theirs). Xie *et al.* [98] have performed quantum dynamics simulations using a model Hamiltonian which includes one (diabatic) triplet state and SOC, and have also found that ultrafast ISC occurs.
It is reassuring to see that our results are consistent with previous work (experimental and theoretical), despite the differences between electronic structure methods used, not to mention the differences methods used to describe ISC.

4.4 Conclusions

We have presented an extension of our previously developed TDDFT-based nonadiabatic molecular dynamics scheme, which allows for the treatment of both nonadiabatic transitions and intersystem crossing transitions between electronic states. To this end, we combined TSH with an accurate and efficient method for the calculation of the SOC-MEs based on the evaluation of the Breit-Pauli Hamiltonian by means of the AMEW [7] associated to the relevant states.

We proposed two alternative solutions to the problem of extending conventional TSH to a more general approach capable of describing ISC events. Both approaches are formulated in the spin-diabatic representation of the molecular states (however, an extension to the spin-adiabatic case is quite straightforward, even though it requires a different, variational, SOC Hamiltonian). The first one, named TSH⊗TSH, consists in the extension of the conventional TSH equation of motion for Tully's coefficients (Eq. (4.2)) to explicitly include the spin-orbit coupling term. The main drawback of this approach consists in the numerical costs associated to the propagation of the coefficients, which requires an update of the SOC-MEs at every time step. In the second, computationally more advantageous approach named TSH⊗LZ, the spin part does not contribute explicitly to the time-evolution of the TSH coefficients, which evolve according to the spin-free Hamiltonian. In the spin-space, we evaluated the ISC probabilities using the Landau-Zener formula at the surface crossings between states of different spin-multiplicity. In this way we are able to restrict the calculations of the SOC-MEs to the points in the neighborhood of the surface crossings with a clear computational advantage. Nonetheless, in order to trace the time evolution of the SOC-MEs one can also compute these quantities

during the whole dynamics with the desired frequency. We applied the TSH⊗LZ scheme to the investigation of the photophysics of SO_2 in gas phase and in solution (meaning liquid SO_2). In the second case, we adopted a QM/MM approach in which one molecule is treated at a DFT/LR-TDDFT level of theory and the surrounding molecules within a molecular-mechanics (MM) description.

Despite its small size, this system displays a very rich photophysics; after excitation to the first singlet absorption band, the system undergoes several NTs and ISCs until it reaches the lower triplet state. We analyzed the dynamics and compared the results with the available experimental and computational data, obtaining good agreement.
The comparison between the gas and liquid phase dynamics is of particular interest, as it reveals the effects of the surrounding molecules on the photophysics of the system. We observe that the main effect of the solvent is to perturb the sampling of the configuration space, therefore modifying the accessibility to the surface crossing points, with a clear consequence on the overall NT and ISC transition rates. On the other hand, we did not observe any direct effect of the surrounding molecules on the electronic structure and in particular on average magnitude of the SOC-MEs, which does not mean that this possibility should also be ruled out in the case of other systems. Furthermore, we estimate that the effect due to compression of the configuration space should be independent of the approximations used for the xc-functional and for the SOC operator, and constitutes an interesting physical aspect of the dynamics in its own right.

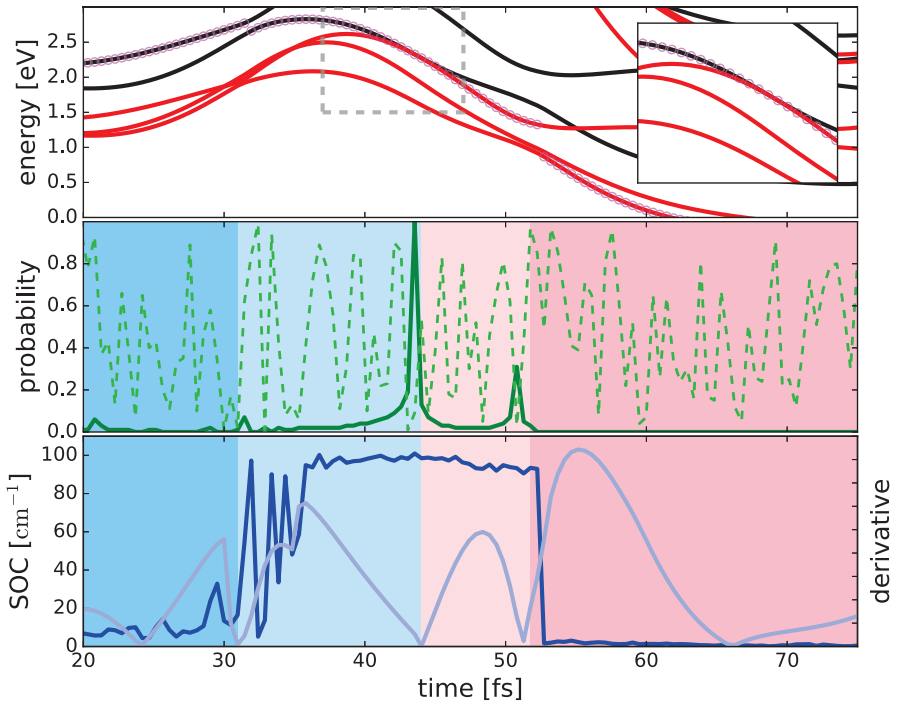

Figure 4.3 – Evolution of the energy of SO_2

(Upper panel): evolution of the energies of states S_1 and S_2 (black) , T_1, T_2, T_3 (red). The purple dots indicate the state driving the dynamics. (Middle panel): Time evolution of the Landau-Zener probability (dark green) and the random number belonging to $[0,1]$. (Lower panel): the dark blue curve shows the time series of the SOC-ME computed along the same trajectory. Due to the presence of NTs and ISCs, the SOC-ME refer to different singlet/triplet pairs in time windows highlighted in different colors: S_2/T_3 in the time interval [20 fs, 30 fs], S_1/T_3 in the time interval [30 fs, 43 fs], T_3/S_1 in the time interval [43 fs, 52 fs], and finally S_1/T_1 after 52 fs. The light-blue line corresponds to the value of the derivative in the denominator of Eq. (5.14). Notice that when the ISC event occurs, the singlet state (in black) approaches the triplet state (in red), then two states touch and remain parallel to one another and finally separate again, leading to a minimum in the derivative. The inset is a close-up of the region delimited by the dashed grey line.

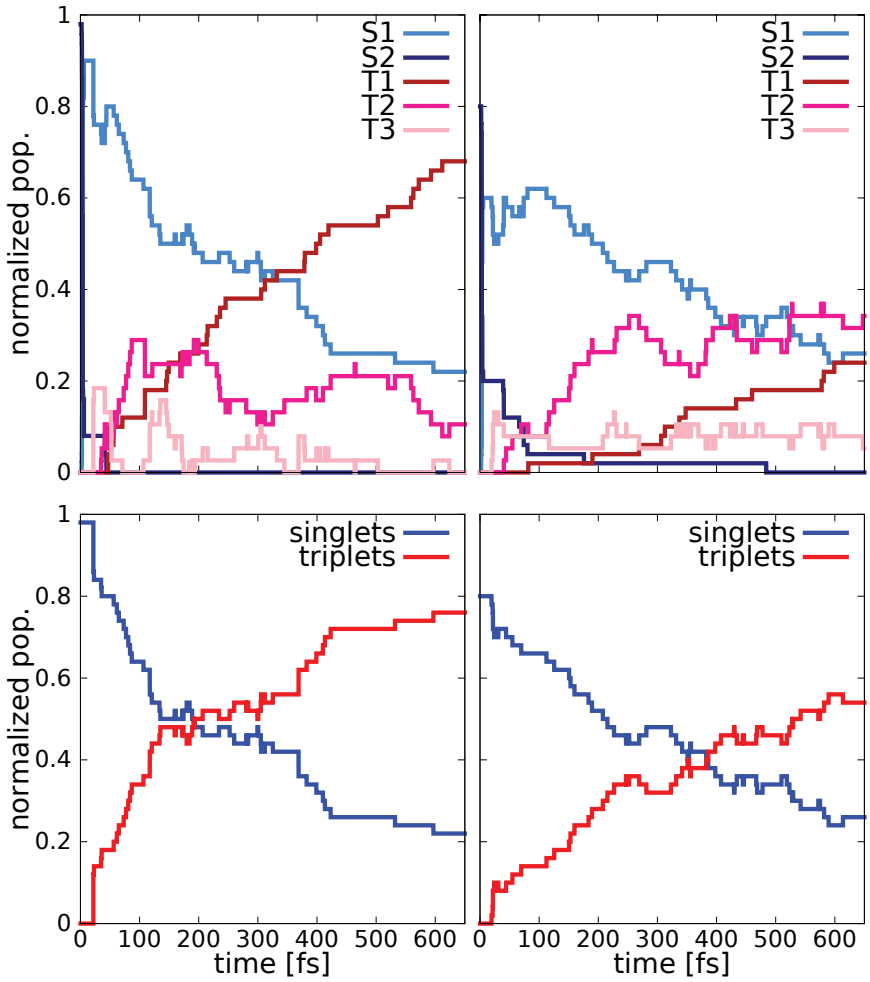

Figure 4.4 – Populations of the SO_2 dynamics

(Upper panel) gas phase (left) and liquid phase (right) normalized trajectory populations as a function of time for each single state involved in the dynamics. (Lower panel) Collective singlet and triplet populations time series (left: gas phase, right: liquid phase).

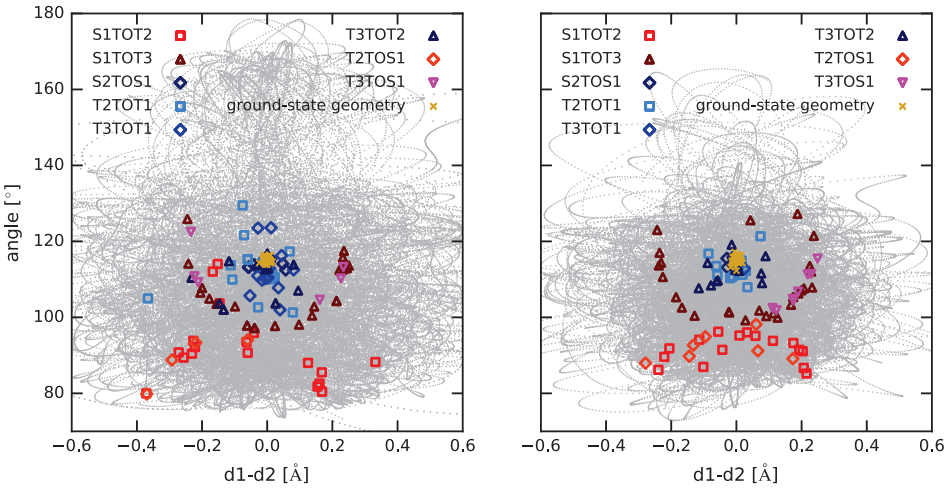

Figure 4.5 – Projection of the TSH trajectories for SO_2

Projection of the TSH trajectories on the plane defined by the ∠OSO angle (y-axes) and the difference between the two SO bond lengths (x-axes). Left: gas phase; Right: liquid phase. The different colored symbols label the points where NT and ISC events take place.

5 TDDFT-based spin-orbit couplings of 0D, 1D, and 2D carbon nanostructures

5.1 Introduction

Graphene has emerged in the last decade as one of the most promising two-dimensional (2D) materials with outstanding mechanical and physico-chemical properties [126, 127, 128, 129]. Among the most interesting properties are ballistic electron transport, heat conduction, anomalous quantum Hall effect, and the ability to sustain very high current densities. Of particular interest is the possibility to tune the electronic properties of graphene by means of chemical functionalizations and doping with other elements, formation of defects [130] and generation of zero-dimennsional (0D) and one-dimensional (1D) nanostructure derivatives like carbon dots, graphene nanoflakes, and carbon nanotubes. While the absence of an electronic band gap limits the efficiency of graphene-based electronic devices [131, 132], 0D and 1D carbon nanostructures are very promising semiconductors thanks to the lateral electron confinement. In addition to their unique properties, graphene-based carbon nanostructures also share other important characteristics including low production costs, low toxicity, chemical stability and biocompatibility, among others [127].

0D carbon-based quantum dots (CQD) are grouped in two main classes: graphene quantum dots (GQDs) and carbon quantum dots (C-dots). GQDs consist of single- and multiple-layered graphene flakes of a size between 10 and 40 nm. Thanks to their unique electronic and magnetic properties such as photoluminescence, quantum confinement and edge effects, GQDs have already found many promising applications in optoelectronics, spintronics, and photoenergy conversion as absorbing dyes in dye-sensitized solar cell devices. On the other hand, C-dots mainly refer to discrete quasi-spherical nanoparticles with a radius smaller than 5 nm. They are usually surface passivated by organic ligands and display light absorption and emission in the visible region, therefore becoming interesting materials for photovoltaics and optoelectronics in general.

Just as the 0D carbon dots, 1D carbon nanostructures can be grouped into two main classes: 1D graphene nanostructures (also known as graphene nanoribbons, GNRs) and carbon nanotubes (CNTs). GNRs have attracted much interest due to their semiconducting behavior and the

possibility of tuning their properties by engineering their size (width) and the topology of their edges [133, 134, 135]. Among the CNTs, single-walled CNT (SWCNT) are composed of a single graphene sheet rolled into a seamless cylinder. Depending on the way the wrapping is achieved the SWCNT can display very different properties. In particular, the band gap can vary from zero to about 2 eV resulting in a metallic or semiconducting behavior. Thanks to their peculiar physical and electronic properties, SWCNTs are very promising candidates for miniaturized electronics; this was demonstrated for the first time in 2001 with the realization of the first intermolecular logic gate based on SWCNTs field-effect transistors [136]. Despite the relatively small size of these systems and their simple chemical compositions, their electronic properties show important variations depending on the nature of the edges and on their chemical functionalization, thermal distortions (conformational changes), and on the overall molecular topology. In the case of CNTs, the bandgap shows a nontrivial dependence on the diameter [137], which strongly reflects the relation between electronic structure properties and the wrapping topology.

Thanks to their electronic properties, these carbon nanostructures are ideal materials for optoelectrical devices. Current applications range from ultrafast photoresistors [138, 139] to photodetectors [133, 134] and light harvesting [135, 140]. In particular, the optical properties of carbon nanostructures can be easily tuned by controlling their size. In this way it is possible to engineer nanostructures with bandgaps in the visible range for applications in organic, single-junction, solar cell devices.

Of particular importance for these applications is a thorough understanding of the photophysical processes that govern the excited state dynamics of 0D and 1D carbon nanostructures. The absorption of a photon induces an electronic transition from the molecular ground state into a resonant excited singlet state. At this point the system can either decay into the lowest singlet state through internal conversion (IC) and emit a photon (fluorescence), or it can relax into a triplet state through inter-system crossing (ISC), which is usually a long-lived state that decays over slower time scales (phosphorescence). In molecular systems like polycyclic aromatic hydrocarbons (0D and 1D carbon nanostructures), this second deactivation channel is usually less populated than the first one for two main reasons. First, the energy spacing between singlet and triplet states is typically of the order of an eV and therefore crossings are rare in the case of rigid structures. In addition, due to the absence of heavy elements, the spin-orbit coupling (SOC) matrix elements that govern the ISC are also relatively small (~ 1 cm^{-1} or even smaller). However, in extended polycyclic aromatic hydrocarbons such as graphene the energy levels spacing reduces substantially through the delocalization of the photoexcited electron over a large surface, opening the possibility for new photophysical effects. In addition, molecular distortions induced by thermal fluctuations can also contribute to the enhancement of the ISC rates between singlet and triplet states through an increase of the SOCs. This is particularly true in the case of relatively large carbon nanostructures, which show a large degree of flexibility. Recent experimental studies have confirmed the occurrence of ISC transitions in carbon nanostrutures [128, 129] and more specifically, in graphene nanoflakes (single-layer carbon nanostucture). These phenomena have a significant

relevance for many technological applications of carbon nanostructures in photovoltaics and nanotechnologies in general, since triplet states have longer diffusion lengths and longer lifetimes than singlets, favoring long-range charge separation and hampering charge carrier recombination.

While ISC events in CQDs are hard to investigate experimentally because of the 'forbidden' nature of these transitions, numerical simulations based on tight-binding (TB) and DFT can provide an accurate description of these phenomena. In particular, both methods can successfully reproduce the characteristic electronic structure properties of graphene and CNT, namely the electron-hole symmetry and the linear dispersion relation at the K and K' points in reciprocal space. Among the two approaches, TB is the simplest one and it is based on a model Hamiltonian that expanded in the basis of the 4 p_z electrons at the 2 inequivalent carbon atoms of the fundamental lattice (labelled A and B, respectively). This model can also be used to obtain numerical estimates for the SOCs [141, 142, 143, 144] when the p_x, and p_y orbitals are included in the minimal basis. Despite the success of TB, a quantitative description of the electronic structure properties of graphene and carbon nanostructures that also takes into account geometrical aspects like, conformational changes, asymmetrical distortions, curvature effects, and chirality in CNT, requires the use of first-principles (FP) calculations. Among the most successful FP approaches, DFT and its time-dependent extension (TDDFT) for the calculation of excited states dynamics [105, 106, 145, 19, 10] and properties [146, 96, 147] offer a well balanced compromise between accuracy and efficiency. In this work we will apply TDDFT for the calculation of the photophysical properties of several 0D and 1D carbon nanostructures, with particular attention to all structural and dynamical effects that influence the ISC rates.

The chapter is organized as follows. Section 5.2 describes the methods used for the calculation of the SOC using tight-binding and DFT/TDDFT with a short summary of the basic theory of nonadiabatic dynamics with ISCs. In Section 5.3 we will briefly summarize the computational details, while in Section 5.4 we will report all results for 0D (C60 and nanoflakes) and 1D (nanotubes) carbon nanostructures, and for graphene. In particular, in subsections 5.4.4 and 5.4.2 we will describe the effects of room-temperature dynamics and structural distortions on the size of the SOC values and corresponding ISC rates for a prototypical carbon nanoflake and a carbon nanotube. Section 5.5 summarizes and concludes.

5.2 Theory and Methods

5.2.1 Electronic structure and SOC of carbon nanostructures: tight binding model

Carbon atoms arranged in a hexagonal lattice have a unique electronic structure that arises from the formation of a very neat and regular arrangement of π bonds. In particular, these structures show a very symmetric electron-hole (valence-conduction bands) linear dispersion behavior at the K and K' points in the reciprocal lattice [148, 149]. Due to the lack of nuclear

spins (for pure ^{12}C compositions) the spin-orbit interactions occur exclusively between the electron spin and angular momentum, which are often suppressed because of symmetries. The principal aim this work is to investigate topological properties (e.g. chirality in nanotubes), finite size effects (like the formation of nanoflakes), and distortions induced by thermal fluctuations and captured by means of ground state and excited state molecular dynamics.

Atomic carbon with electronic configuration $(1s^2, 2s^2, 2p^2)$ has an estimated atomic spin-orbit splitting of about 6-10 meV ($\sim 48-81\ cm^{-1}$) [150, 151]. However, as mentioned above, several factors can influence the magnitude of this interaction.

Before addressing these issues, we give a very brief introduction about the electronic properties of the two representative carbon structures for which a simple tight-binding model already give a good qualitative description: graphene and nanotubes.

Graphene

Within tight-binding, graphene can be fully described by the p_z-orbitals coupled through nearest neighbor interactions. Considering the fundamental basis units made of two inequivalent carbon atoms (A and B defining two inequivalent sub-lattices), the electronic structure of graphene can be described by the basis set $B = \{p_z^A(\uparrow), p_z^A(\downarrow), p_z^B(\uparrow), p_z^B(\downarrow)\}$. A detailed account of the band-structure of graphene within tight-binding in absence of SOC can already be found in the literature (see for instance Ref. [152]) and therefore we will not develop further on this issue.

When SOC are included, the picture becomes slightly more complex. In fact, SOC induce interactions between all p-orbitals at each carbon atom, therefore allowing for the physical coupling between next-nearest-neighbours atoms. This process can be enhanced by doping and/or distortion from planarity, which induce a $\sigma-\pi$ rehybridization at the carbon sites with consequent increase of the SOC. To account for this effect, the tight-binding basis needs to be further extended to include the p_x-orbitals and p_y-orbitals at each carbon site and the σ-orbitals in the graphene plane.

SOCs have two effects on the electronic structure of graphene. The most evident one is that it allows the ISC between states of different spin multiplicity, which is the main topic of this investigation. However, SOCs also have a direct effect on the band structure introducing k-dependent shift of the electronic bands through a second order mechanism, which can be summarized as follows: the $p_z^A(\uparrow)$ electron of atom A can hop onto a $p_x^A(\downarrow)$ electron through the effect of the SOC; then the interaction is 'transported' through σ-couplings from this A-center to a second one in its neighborhood passing through a B-center and, finally, interact with the $p_z^A(\uparrow)$ electron of the second A-carbon through a second SOC. This effect was investigated by Min et al [144] using tight-binding. They arrived at the following interesting second order

correction for the band energies

$$\Delta E^{(2)}_{SOC} = \frac{|s|}{18(sp\sigma)^2}\Delta^2_{SOC} \tag{5.1}$$

where $|s| = 8.87$ eV is the energy splitting between carbon s and p orbitals, and $sp\sigma$ is the band parameter used in Min's model [144]. Using an average value of $\Delta_{SOC} = 10meV$ for the atomic SOC one gets an average effect of about 1.6 μeV.

Another interesting effect on the magnitude of the SOC in graphene is induced by the curvature. By bending the carbon sheet uniformly one produces a lowering of the symmetry of the orbitals with a consequent increase of the overlap between atomic orbitals sitting on different carbon atoms. In particular, through bending one can achieve overlap between p_z and p_x-orbitals of neighbor atoms on different A and B sub-lattices contributing therefore to an increase of the overall SOC (whose main contribution is intra-atomic). Huertas-Hernando and co-workers [153] estimated this contribution to be

$$\Delta^{\text{curv}}_{SOC} = \frac{V_{pp\sigma} - V_{pp\pi}}{V_1}\left(\frac{a}{R_1} + \frac{a}{R_2}\right)\frac{V_1^2}{V_2^2}\Delta_{SOC} \tag{5.2}$$

where $a = 1.42$ Å is the carbon-carbon bond length, R_i are the curvature radii in x and y directions, and $V_1 = 2.47$ eV, $V_2 = 6.33$ eV, $V_{pp\sigma} = 2.47$ eV, $V_{pp\pi} = -2.24$ eV and $V_1 = 2.47$ eV are the band parameters of the model Hamiltonian [153]. Using a standard value for the intra-atomic SOC energy of about 10 meV one gets $\Delta^{(\text{curv})}_{SOC} \sim 0.08$ meV (0.64 cm^{-1}) for an average curvature radius $R = 5$ Å, which grows up to 3.4 meV (27.4 cm^{-1}) for $R = 10$ Å.

Nanotubes

Carbon nanotubes have different topologies, each one characterized by a couple of numbers (n, m), with $n \geq m$ which indicate how a graphene sheet is rolled up. Picturing an unrolled carbon nanotube on a graphene sheet with primitive lattice vectors $\mathbf{a_1}$ and $\mathbf{a_2}$ the circumferential vector

$$\mathbf{C}_h = n\mathbf{a}_1 + m\mathbf{a}_2\,, \tag{5.3}$$

connects equivalent atoms of the nanotube (5.1) and defines its diameter $d = \frac{||\mathbf{C}_h||}{\pi}$ and curvature

$$\kappa = \frac{2\pi}{a\sqrt{n^2 + nm + m^2}} \tag{5.4}$$

where $a = ||\mathbf{a}_1||$. Figure 5.1 is a schematic depiction of how to build the $(4,2)$ nanotube; the grey area represents the surface of the unrolled nanotube superposed on a graphene lattice. For completeness, we also mention that nanotubes can also be classified according to their chirality, which is also a function of the pair of indices (n, m) and defined by the chiral angle θ

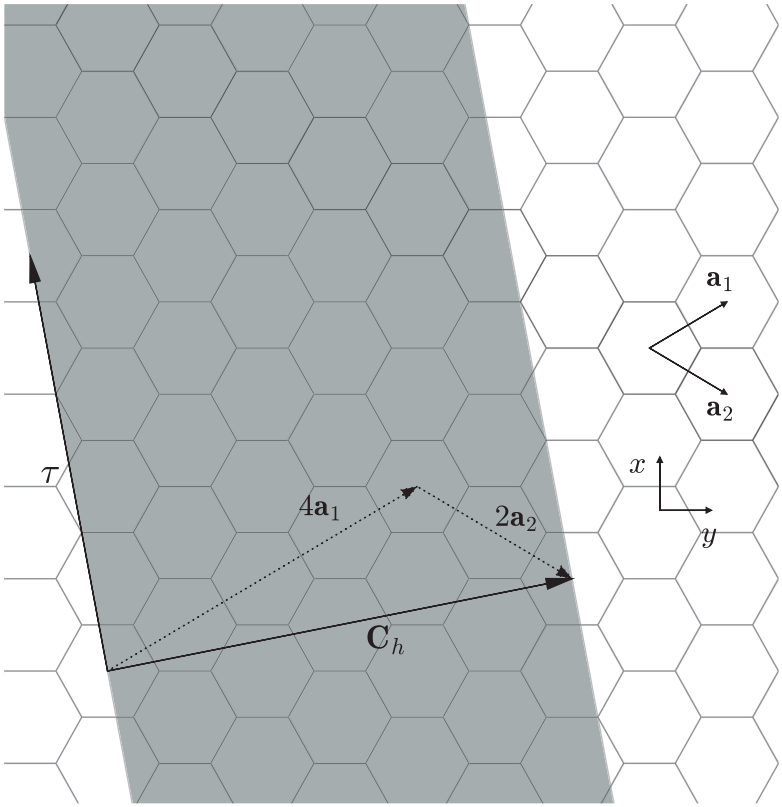

Figure 5.1 – Unrolled nanotube.

Graphene sheet with lattice vectors $\boldsymbol{a}_1$ and $\boldsymbol{a}_2$. The grey area represents the surface area of an unrolled $(4,2)$ nanotube. The vector $\mathbf{C}_h = 4\mathbf{a}_2 + 2\mathbf{a}_2$ becomes circumference of the nanotube, while the τ runs along its axis.

with

$$\cos\theta = \frac{\mathbf{C}_h \cdot \mathbf{a_1}}{||\mathbf{C}_h||||\mathbf{a_1}||} = \frac{2n+m}{2\sqrt{n^2+nm+m^2}} \tag{5.5}$$

Achiral nanotubes are those with $(n,0)$ or $(0,m)$ (called *zig-zag*) and those with $n = m$ (called *armchair*); all others are chiral nanotubes. More important for us is to investigate the relation between the topology of the nanotube and their electronic structure properties.

According to the tight binding model in the zone-folding approximation, the electronic properties of the nanotubes can also be easily classified in terms of the topology indices (n,m). Due to the constrained induced by the periodicity of the CNT along its circumference and differently form the graphene case, the CNT molecular wavefunctions are described by a

discrete set of electronic momenta (**k**) that satisfy the relation

$$\mathbf{k}\cdot\mathbf{C_h} = 2\pi l\,, \tag{5.6}$$

for integer l, which is equivalent to confine the **k** in discrete planes in the Brillouin zone that intersect the 2D graphene band-structure into a set of discrete subbands.

Metallic CNT. When one of the subband includes the K-point at the Dirac cone, the CNT is metallic [148, 154, 155, 156, 157]. This condition is achieved when $\mathbf{K}\cdot\mathbf{C_h} = 2\pi l$, which can be translated into the simple relation $n-m = 3l$. According to this model, all armchair (n,n) CNT, the zig-zag CNT with the topology $(3n,0)$, and a good subset of chiral CNT with indices or $(3l-m,m)$ are metallic.

Semiconducting CNT. In the case the subbands do not include the K-point, for $n-m = 3l\pm 1$, the CNT will present an energy gap and becomes therefore a semiconductor. According to tight binding, the gap opening amounts to

$$E_g = \frac{2\pi a t_0}{\sqrt{3}||\mathbf{C_h}||} \tag{5.7}$$

and is therefore inversely proportional to the CNT diameter (and proportional to the curvature κ). In Eq. (5.7) t_0 corresponds to the tight-binding *transfer integral* between nearest neighbor carbon atoms.

Concerning the estimation of the SOC, Huertas-Hernando et al., developed a model based on and extended tight- binding two-component spinor Hamiltonian [153]. However, the effect of the spin-orbit interaction enters merely as an effect of the CNT curvature and therefore it is insensitive to the specific electronic properties of the CNT that depend on the topological indices (n,m). Using the result for graphene (Eq. (5.2)) and considering a single curvature along the circumference of the CNT, one gets

$$\Delta_{SOC}^{\mathrm{CNT}} = a\frac{V_{pp\sigma}-V_{pp\pi}}{V_1}\frac{V_1^2}{V_2^2}\frac{\Delta_{SOC}}{d} \tag{5.8}$$

where d is the diameter of the CNT. While this formula is very useful for a rationalization of the dependence of the SOC as a function of the CNT dimensions, its quantitative predictions are in many cases unsatisfactory. This is mainly due to the limits of the assumptions in the tight binding model for CNT, which, as mentioned above, does not take in fully account the dependence of the electronic structure from the topological properties of the CNT. In particular, the map: $(n,m)\rightarrow d$, is non-injective and therefore Eq. (5.8) cannot unambiguously describe the SOC of the different CNT topologies.

5.2.2 Electronic structure and SOC of carbon nanostructures: DFT calculations

Electronic structure of graphene and CNT with DFT

While successful in many aspects, the tight binding model also shows some important deficiencies. In particular, the assumptions used to evaluate electronic structure properties (such as SOC) introduce notable discrepancies that mask the complex dependence on the topological structure of the carbon nanostructures of interest. As a consequence, CNTs with similar curvature may have strikingly different electronic structure properties, which cannot be captured by these models.

In order to shed new light on this issue, we plan to investigate the electronic structure of CNT using DFT and TDDFT, focusing our attention on the magnitude of the SOC and their dependence on the topology indices (n, m) and the curvature κ (Eq.(5.4)).

The main advantage of DFT/TDDFT approach compared to tight binging can be summarized in the following points: *(i)* DFT is a *first-principle* approach that can be considered parameter-free. This is particularly true in case of the use of the PBE [113] functional that, for the purpose of this study, offers a very favorable compromise between accuracy and computational costs. In particular, DFT/PBE does not require any system specific parametrization for the study of carbon nanostructures. *(ii)* DFT can naturally account for effects like σ-π-rehybridization [158], which are difficult to capture using tight-binding based approaches. In fact, tight-binding assumes no interaction between the p_z-orbitals and the σ bands (or subbands in CNT). While this is the case in perfectly flat graphene, curvature will induce coupling between the σ and the π/π^* manifolds, especially for CNT with relatively short diameters (< 1 nm). *(iii)* Contrary to TB, DFT/TDDFT calculations can account for the asymmetry between the valence and conducting π/π^* that arise form overlaps between p_z orbital not included in the model Hamiltonians. *(iv)* DFT/TDDFT can describe without further modeling the complex dependence of the electronic structure of CNT from the topological indices (n, m). As mentioned in the previous section, tight binding can encounter severe problems to capture some important electronic structure differences in CNTs with similar curvature but different topological indices.

5.2.3 SOC and nonadiabatic dynamics within the TDDFT framework

In this section we review the method for the calculation of SOCs within the linear TDDFT framework in the linear-response regime (LR-TDDFT) and present the basic scheme used to model nonadiabatic dynamics with intersystem crossings.

SOC calculations in LR-TDDFT. The computation of SOC within linear-response TDDFT (LR-TDDFT) involves the use of the many-electron auxiliary wavefunction (AMEWF) intro-

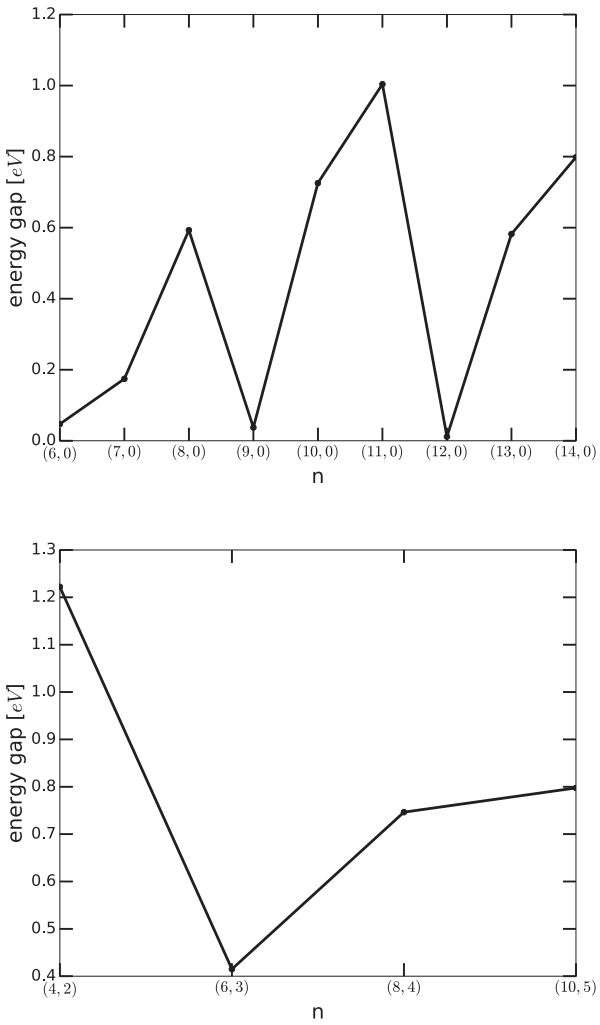

Figure 5.2 – LR-TDDFT/PBE bandgaps for a series of nanotubes.

duced in [7, 6, 19],

$$|\tilde{\Psi}_I\rangle = \sum_{i}^{N} \sum_{\xi=\{\alpha,\beta\}} \hat{r}_{i\xi}^{\dagger I}\, \hat{a}_{i\xi} |\tilde{\Psi}_0\rangle \,, \tag{5.9}$$

where $|\tilde{\Psi}_0\rangle$ is the Slater determinant of all the occupied KS orbitals, N is the number of electrons, $\hat{a}_{i\xi}$ is the annihilator operator for the occupied KS orbital $\phi_i(\boldsymbol{r})$ with spin ξ and $\hat{r}_{i\xi}^{\dagger I}$ is the creator operator for the corresponding linear-response (LR) orbital $\varphi_i^I(\boldsymbol{r})$ associated to the excited state I within the Sternheimer formulation of LR-TDDFT [59, 60] . The LR KS-orbitals satisfy therefore the Sternheimer equations

$$[\epsilon_k - \omega_I - H^{KS}]\varphi_k^I(\mathbf{r}) = \mathscr{Q}[\delta V(\mathbf{r}) + \delta V^{SCF}(\omega)]\phi_k(\mathbf{r}) \,, \tag{5.10}$$

where H^{KS} is the KS Hamiltonina, ϵ_k is the KS orbital energy associated to $\phi_k(\boldsymbol{r})$, ω_I is the excited state energy of state I, and $\mathscr{Q} = 1 - \sum_{i=1}^{N} |\varphi_i\rangle\langle\varphi_i|$ is the projector onto the subspace of virtual KS orbitals.

It is important to mention that the concept of AMEWF also applies to the Casida's formulation of LR-TDDFT [6, 7, 8, 55]. However, the Sternheimer approach has the advantage of describing each individual excitation in the subspace of N linear independent LR KS orbitals, making therefore the calculation of a large number of KS virtual orbitals unnecessary. The AMEWF of Eq. (5.9) is a linear combination of singly-excited Slater determinants and is specific for each electronic excited state I. We emphasize that these auxiliary wavefunctions have no direct physical meaning (they are not eigenstate of the electronic Hamiltonians), but when used in the calculations of matrix elements of one-body operators $\langle\tilde{\Psi}_0|\mathscr{O}|\tilde{\Psi}_I\rangle$, they provide the exact linear response quantity [7] (within the approximations used in the TDDFT calculations). Recently, we also proved that the same procedure can be used to approximate second-order response quantities of the form $\langle\tilde{\Psi}_I|\mathscr{O}|\tilde{\Psi}_J\rangle$ between pairs of excited states wavefunctions $|\tilde{\Psi}_I\rangle$ and $|\tilde{\Psi}_J\rangle$ [9].

Of particular relevance for this study is the calculation of the SOC matrix elements between a pair of singlet and triplet excited state wavefunctions. To this end, we use the Breit-Pauli one-electron description of the SOC operator of Eq. (2.132) evaluated for 2-component KS-spinors and LR KS-spinors with α and β components [159].

Mixed-quantum classical dynamics with ISC. Excited state dynamics is performed using a mixed quantum-classical approach based on LR-TDDFT for the solution of the electronic structure problem at each nuclear configuration [6]. For this study, we use a recent extension of the algorithm [47], which can compute *on-the-fly* nonadiabatic transitions between states with the same spin multiplicity (internal conversions) as well as between singlet and triplet states (intersystem crossings). The method, named TSH⊗LZ algorithm [47], evaluates nonadiabatic transition probabilities using the Tully's surface hopping algorithm [25] in the spin-free part of the electronic Hilbert space, while ISC probabilities in spin space are computed using the

Landau-Zener formalism [110, 111].

Nuclear trajectories are therefore propagated *on-the-fly* using Newton's equation of motion with forces derived at LR-TDDFT level of theory. In parallel, a set of amplitude coefficients C_K (one for each electronic state K) associated to each nuclear trajectory are propagated according to

$$\dot{C}_K(t) = -iC_K(t)\omega_K - \sum_I C_I(t)\sigma_{IK}(t)\,, \tag{5.11}$$

where $\sigma_{IK}(t)$ are the nonadiabatic coupling coefficients obtained from the scalar product between the nuclear velocities and the nonadiabatic coupling vectors for the adiabatic states I and K [6, 9]. The probability for a nuclear trajectory to hop from state I to state K in the time interval $[t, t+\delta]$ is given by

$$p_{KI} = -2\int_t^{t+\delta} \frac{Re\left[C_K(\tau)C_I^*(\tau)\sigma_{KI}(\tau)\right]}{C_I(\tau)C_I^*(\tau)}d\tau\,. \tag{5.12}$$

meaning that it occurs when the inequalities

$$\sum_{L\leq K-1} p_{LI} < \zeta < \sum_{L\leq K} p_{LI}\,, \tag{5.13}$$

hold for a random number ζ generated in the interval $[0,1]$.

In the spin space, ISC probabilities between two states I and J of different spin multiplicity are computed *on-the-fly* using the Landau-Zener expression

$$p_{IJ}^{LZ} = 1 - e^{-2\pi\Gamma_{IJ}}\,, \tag{5.14}$$

where the Landau-Zener parameter is approximated with [160, 161]

$$\Gamma_{IJ} = \frac{|\langle\Psi_I|H_{1el}^{SO}|\Psi_J\rangle|^2}{d\omega_{IJ}/dt}\,. \tag{5.15}$$

In Eq. (5.15) the energy difference $\omega_{IJ} = |\omega_I - \omega_J|$ is the absolute value of the energy gap between the two states evaluated in the spin-diabatic representation [159, 47]. According to this formulation, a ISC occurs stochastically at the crossing point between states I and J, when the probabilities p_{IJ}^{LZ} is larger than a random number generated in the interval $[0,1]$.

5.3 Computational details

All calculations were performed with the plane-wave-pseudopotential code CPMD [56], which uses the Sternheimer formulation for LR-TDDFT [59, 60] within the Tamm-Dancoff approximation (TDA) [40, 60]. The PBE approximation [113] to the exchange-correlation functional functional was used in all calculations together with the adiabatic approximation [37, 115] for

the LR-TDDFT kernel. The Trouiller-Martins norm-conserving pseudopotentials [75] were used for both carbon and hydrogen atoms, and the chosen plane-wave cutoff value was 40 Ry. For the molecular dynamics simulation on the single-layer graphene dot a time-step of 5 a.u. (0.121 fs) was used. The molecule, composed of 38 carbon atoms and capped by 16 hydrogen atoms, was placed in a box of size 18Å × 10Å × 18Å and periodic images were screened using the Martyna/Tuckerman algorithm [114]. The system was equilibrated using Born-Oppenheimer dynamics MD in the ground state at room temperature (300 K). A random frame was selected as a starting point for the excited state nonadiabatic dynamics started in the first singlet excited state S_1. Spin-orbit couplings were calculated every 10 time-steps of dynamics (approximately 1.2 fs) and the intersystem crossing transition probability were evaluated using the approach described in Ref [47]. All static calculations on nanotubes were performed using periodic boundary conditions in the three dimensions with box sizes that were adapted to the particular structure considered.

5.4 Results and Discussion

5.4.1 0D carbon nanostructures

C_{60} Buckminsterfullerene

The best known fullerene-type carbon nanostructure is the C_{60} molecule. The molecule is composed of 60 carbon atoms arranged in 20 hexagons and 12 pentagons (unlike the other nanostructures, which are only composed of hexagons). It is worth mentioning that C_{60} is not an aromatic molecule, despite the large number of carbon-carbon π-bonds. C_{60} can exist either as a molecular compound or as a van der Waals fcc solid. In this work we have performed SOC calculations on a single C_{60} molecule for which tight-binding spin-orbit coupling results are available in literature. The DFT/PBE optimized structure shows C-C bond lengths of 1.45 Å between two hexagons and 1.40 Å between a hexagon as well as a pentagon and a nucleus-to-nucleus diameter of 7.12 Å, in good agreement with experimental measurements. The LR-TDDFT/PBE SOC values obtained for C_{60} range between 0.03 and 4.95 cm^{-1} and are all reported in table 5.1.

These values fall within the range of SOC values that we obtained for bent graphene flakes (1-3 cm^{-1}) and nanotubes with rather small curvature (see section 5.4.2 below). Comparing the curvature of the C_{60} molecule (~ 0.28 Å^{-1}) with that of a nanotube with similar transverse curvature, we could have expected a larger SOC value (see figure below). However, this does not come as a surprise. First, the chemical composition of C60 and CNT is different (pentagons and hexagons in the C60, and only hexagons in CNT), and, second, in CNT there is no curvature along the main longitudinal axis. LR-TDDFT/PBE allows access to higher excited states than TB. Huertas *et. al.* reported TB values for the SOC-induced splitting of triplet states in C_{60} of the order of only 10^{-2} cm^{-1}, which are in good agreement with the values we obtained for the coupling between low lying excited states. At higher in energy, we observe an enhancement of

	T_1	T_2	T_3	T_4	T_5	T_6	T_7	T_8
S_0	0.01	3.77	1.72	1.72	0.00	0.00	0.00	0.00
S_1	21.21	0.01	0.02	0.02	1.27	0.00	0.00	0.00
S_2	0.24	3.70	1.47	1.49	0.02	0.00	0.00	0.03
S_3	1.27	21.49	0.00	0.00	20.50	0.00	0.00	0.00
S_4	0.09	1.52	12.91	31.54	0.00	0.02	0.00	0.06
S_5	0.00	1.53	17.41	27.60	0.00	0.01	0.00	0.05
S_6	0.00	0.00	0.00	0.00	0.00	0.01	3.73	0.00
S_7	0.00	0.00	0.14	0.09	0.00	20.50	0.01	2.18
S_8	0.00	0.00	0.02	0.13	0.00	1.98	0.00	20.18

Table 5.1 – SOC values for C_{60}

LR-TDDFT/PBE SOC values for the lowest 8 singlet and triplet states of C_{60}.

the SOC between singlet and triplet states that may play an important role in determining the photophysical properties of C60, especially in optoelectronics.

For completeness, we have also performed a SOC calculation with the ADF software package [81] (using the DFT/LR-TDDFT and the PBE functional), which uses the ZORA Hamiltonian [53, 54], and find good agreement with our results (values within 10^{-2} cm^{-1} and 1 cm^{-1}).

Nanoflake

As a second example of CQD (0D structure) we consider a graphene nanoflake composed of 38 carbon atoms saturated at the edges with hydrogen atoms. This structure can also be seen as a constituent unit (a 'supercell') of a larger 1D molecule (like CNTs) and of 2D graphene. While flat in its optimized ground-state structure, this system undergoes important conformational changes during ground state as well as excited state dynamics at room temperature. In this section, we will start by investigating the electronic properties of the nanoflake in its perfectly flat geometry; the excited state dynamics of the same system, including transitions mediated by ISCs, will be addressed in section 5.4.4.

Table 5.2 reports the excited state energies, oscillator strengths and corresponding assignments of the first three excited singlet and triplet states of the nanoflake, evaluated at the ground state optimized geometry. The oscillator strength of the S_1 is much larger than those of all other excited singlet states (S_2 and S_3, as well as S_4 and S_5 not shown in the table), and it is therefore the state most likely populated upon photoexcitation. Concerning the triplet states, T_1 is significantly lower in energy than S_1 (of about 1 eV) and we do not expect it to play any important role in photophysics of the system. On the other hand, T_2 and T_3 are energetically very close to S_1 (around 0.1 and 0.2 eV, respectively) and therefore, for sufficiently large values of the SOCs, there is a sizable probability of an ISC between S_1 and one of these triplets.

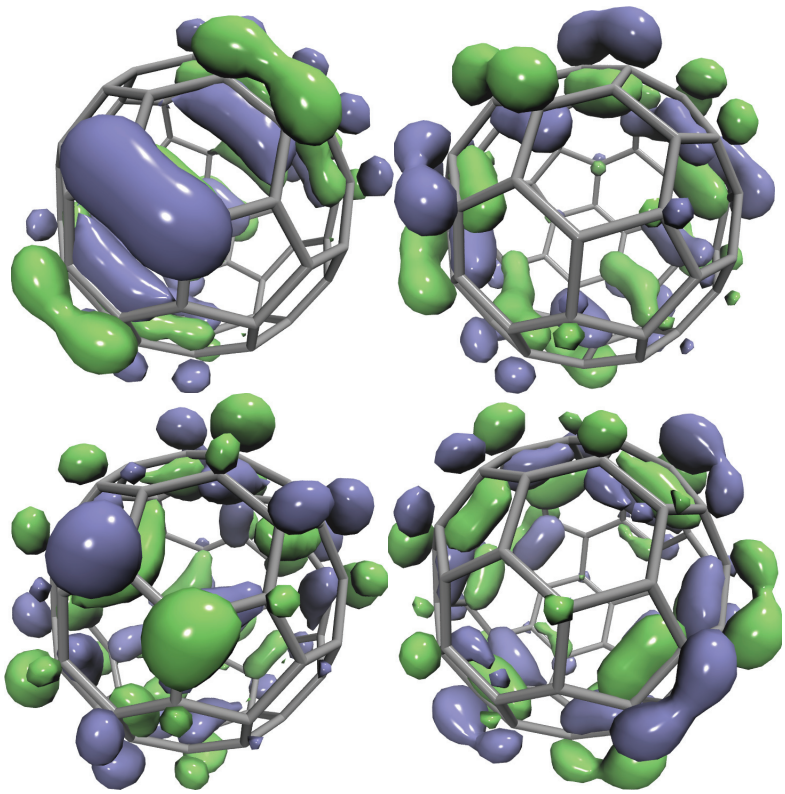

Figure 5.3 – Kohn-Sham orbitals of the C_{60} molecule

From left-to-right, top-to-bottom: HOMO-1, HOMO, LUMO, LUMO+1.

Concerning the character of these transitions, we observe that both S_1 and T_1 are well described by 'pure' HOMO to LUMO transitions, while the other two states (S_1, S_2, and the corresponding triplets) involve transitions from the three highest occupied orbitals (HOMO-2, HOMO-1, and HOMO) to three lowest unoccupied orbitals (LUMO, LUMO+1, and LUMO+2). Six of these orbitals are shown in Fig. 5.4 and they display, as expected, a clear π character for the occupied frontier orbitals and a mixture of π and π^* character for the unoccupied ones. As confirmed by our LR-TDDFT/PBE calculations (see table 5.2), the SOC between these states is around 1/10 of the atomic carbon SOC between p-orbitals, which is therefore much lower than what expected for organic molecules with heteroatoms (nitrogen, oxygens or other heavier atoms) in which El-Sayed $(n,\pi^*)/(\pi,\pi^*)$-type of transitions induce large SOCs. The situation changes when thermal effects are included. Dynamics induces conformational distortions that affect the curvature of the nanoflake with a consequent increase of the SOCs (thanks to a larger overlap between p-type orbitals), as discussed in Section 5.2.3. A detailed analysis of the ISC dynamics in this compound will be given Section 5.4.4.

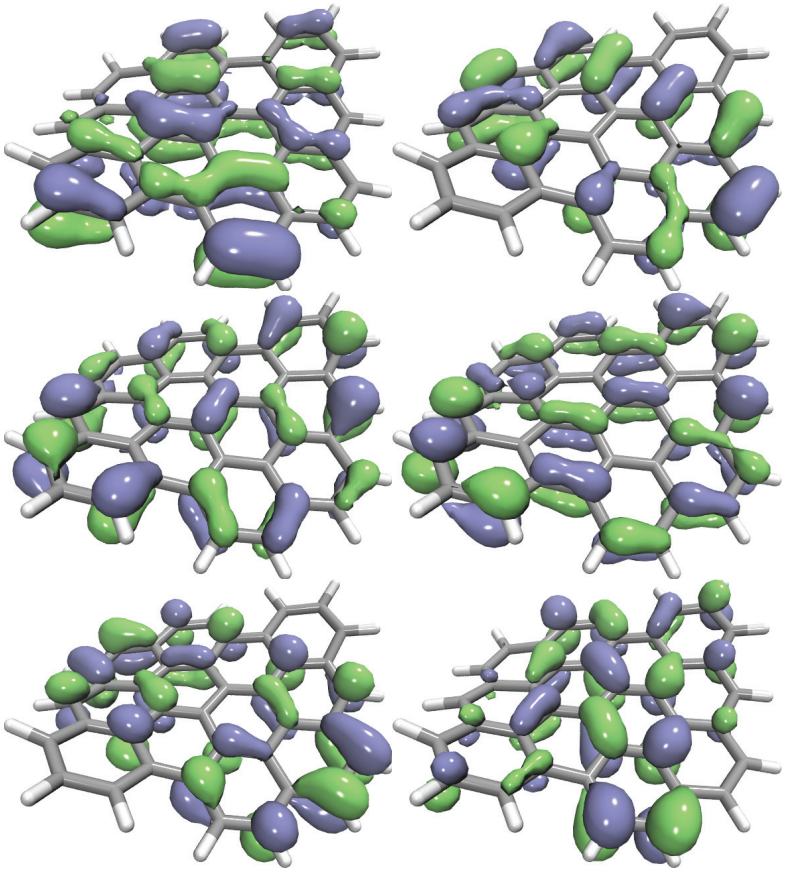

Figure 5.4 – Kohn-Sham orbitals of the nanoflake.

From left-to-right, top-to-bottom: HOMO-2, HOMO-1, HOMO, LUMO, LUMO+1, LUMO+2.

5.4.2 1D: Carbon Nanotubes

As described in Section 5.2.1, the physical properties of CNTs depend in a non trivial manner from the topological indices (n, m), which determine both their size (diameter and curvature) and their electronic properties (metallic vs. semiconducting) including the magnitude of the SOCs. TB predicts a dependence of the SOC on the curvature of the CNT without however, providing a detailed picture of the phenomena in terms of electronic structure properties valid for all points of the Brillouin zone. In this study, we investigate the dependence of the SOC on the topological indices (n, m) using first-principle LR-TDDFT/SOC calculations on 13 different CNTs that sample a good portion of the (n, m) space for $4 \leq n \leq 14$ and $0 \leq m \leq 5$ (see table 5.3) including zig-zag and chiral structures.

We computed SOCs between the first 9 singlet states (including the ground state) and first 8 triplet excited states, for a total of 72 values for each CNT. All calculations are performed at the Γ point using a supercell periodically replicated in the three spatial dimensions. Along the CNT principal axis the supercell comprises a multiple of the primitive translation vector τ,

State	Excitation energy [eV]	Oscillator strength	Assignement
S_1	1.973	0.23785	HOMO → LUMO (86.9%)
S_2	2.213	0.00029	HOMO → LUMO + 1 (50.7%)
			HOMO − 1 → LUMO (48.2%)
S_3	2.384	0.00111	HOMO → LUMO + 2 (47.3%)
			HOMO − 2 → LUMO (42.4%)
			HOMO → LUMO + 1 (5.0%)
			HOMO − 1 → LUMO (4.4%)
T_1	1.013	—	HOMO → LUMO (98.7%)
T_2	1.980	—	HOMO − 1 → LUMO (52.8%)
			HOMO → LUMO + 1 (42.4%)
T_3	2.185	—	HOMO → LUMO + 1 (52.5%)
			HOMO − 1 → LUMO (43.1%)
			HOMO → LUMO + 2 (2.4%)
			HOMO − 2 → LUMO (1.8%)

Table 5.2 – Excited states of the nanoflake.

Characterization of the lowest electronic excited states of the nanoflake at LR-TDDFT/PBE level of theory.

namely $3\|\tau\| = 12.78$ Å in the case of the zigzag CNTs and $\|\tau\| = 11.27$ Å for the chiral CNTs in order to guarantee a similar length along for all structures. The other two edges of the supercell (perpendicular to the principal axis) are fixed at 10 Å plus the diameter of the tube for all CNTs.

All the 72 values of SOC calculated for the $(6,0)$ nanotube are given in Table 5.4, while for the other CNTs the results are summarized in the SI. In order to visualize the dependence of the SOC on the nature and the topology of the different CNTs, we decided to report the value of the maximum SOC for each structures as a function of the curvature and of the topological indices (n,m). In fact, due to the large variety of the structures considered it is not possible to select a characteristic pair of singlet and triplet states to analyze across the entire series of CNT considered in this study. The maximum SOC values give a good description of the trends; however, the mean values over the 72 SOC values calculated for each CNT also reproduces the same scenario (see SI).

Fig. 5.5 and 5.6 report all the maximum SOC values considered in this study organized according to their electronic properties (metallic vs. non-metallic, Fig. 5.5) and topology (chiral vs. non-chiral, Fig.5.6). In Fig. 5.5 the red symbols represent the non-metallic CNTs (with nonvanishing band gaps), while the green ones describe the metallic structures. As predicted from the TB model, we observe a linear increase of SOC values as a function of the curvature, which is particularly conspicuous for metallic nanotubes. However, we also observe an important modulation related to the topology of the CNTs, which induces a particularly important spread for the non-metallic structures. Fig. 5.6 features the same data, but colored according to the topology of the CNTs; the blue dots correspond to the chiral structures, whereas the orange ones correspond to achiral ones. Also in this case, we confirm a similar trend as a function of

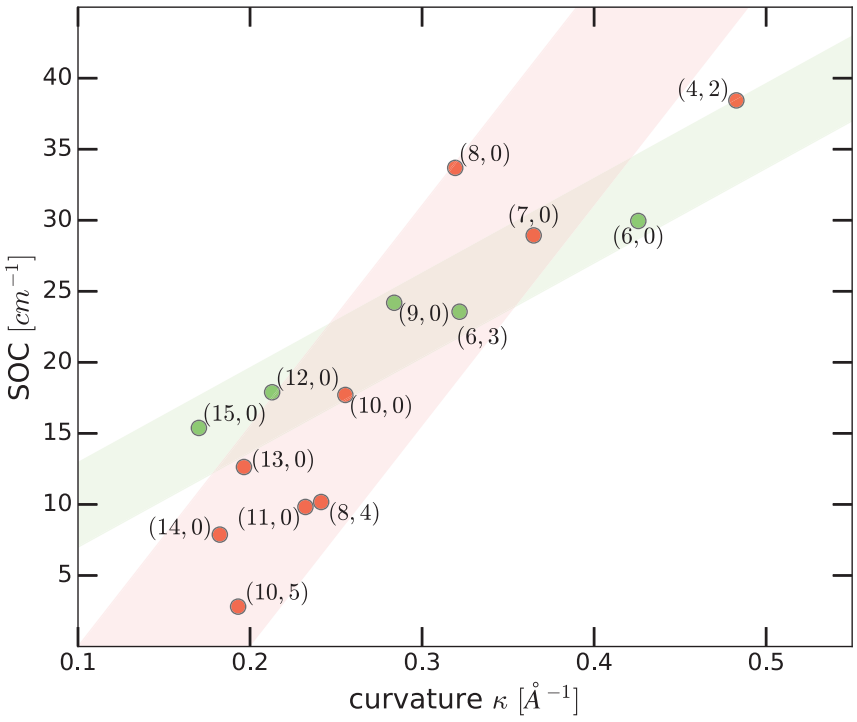

Figure 5.5 – SOC values for nanotubes (i)

Maximum values among the first 8 excited states of the different CNTs plotted against their curvature, κ. Green dots represent metallic nanotubes, while red dots represent non-metallic ones. The colored bands are added as a guide for the eyes.

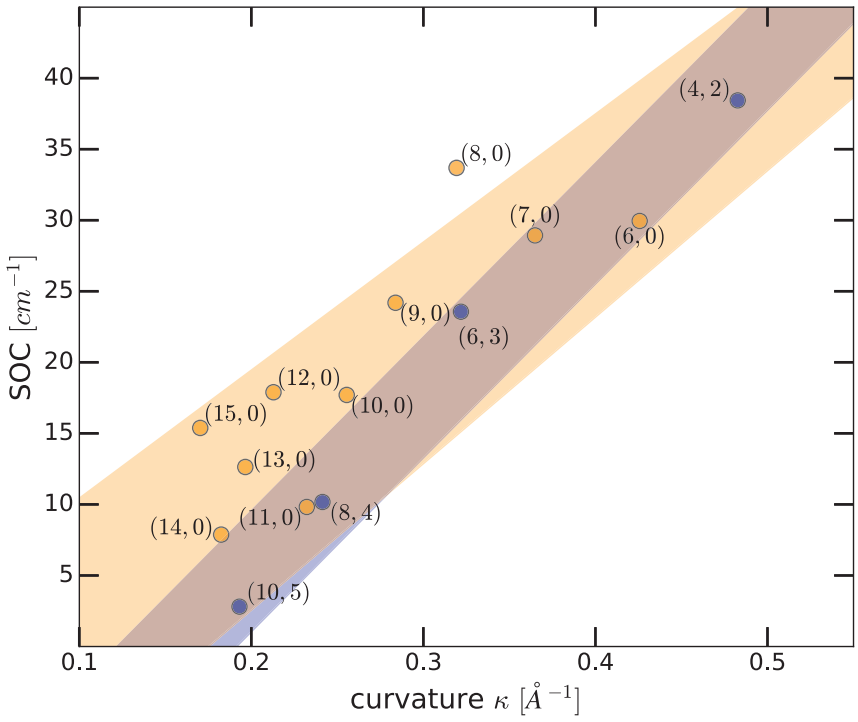

Figure 5.6 – SOC values for nanotubes (ii)

Maximum among the first 8 excited states of the different CNTs plotted against their curvature, κ. Orange dots represent achiral nanotubes, while blue dots represent chiral ones. The colored bands are added as a guide for the eyes.

the curvature even through the slope of the curves is different for the two families (larger of the chiral CNT) and the modulation induced by the topological indices is also quite strong especially in the case of the achiral structures.

In summary, our LR-TDDFT results confirm the existence of a correlations between the curvature of the CNTs and the intensity of the SOC. However, the picture that emerges from first-principle calculations is more complex showing different 'linear' dependences for different families of CNTs, as well as important modulations related to the topology of the structures.

zigzag			
structure	diameter [Å]	curvature [1/Å]	n. atoms
(6,0)	4.69825392	0.2378500	72
(7,0)	5.48129624	0.36487720	84
(8,0)	6.26433856	0.31926755	96
(9,0)	7.04738088	0.28379337	108
(10,0)	7.83042320	0.25541404	120
(11,0)	8.61346552	0.23219458	132
(12,0)	9.39650784	0.21284503	144
(13,0)	10.17955016	0.19647234	156
(14,0)	10.96259248	0.18243860	168
chiral $n = 2m$			
(4,2)	4.14347049	0.48268716	56
(6,3)	6.21520573	0.32179144	104
(8,4)	0.24134358	8.28694098	112
(10,5)	10.35867622	0.19307486	140

Table 5.3 – Characteristic properties of the CNTs investigated.

	T_1	T_2	T_3	T_4	T_5	T_6	T_7	T_8
S_0	0.01	3.77	1.72	1.72	0.00	0.00	0.00	0.00
S_1	20.63	0.01	0.02	0.02	1.27	0.00	0.00	0.00
S_2	0.24	3.70	1.47	1.49	0.02	0.00	0.00	0.03
S_3	1.27	0.00	0.00	0.00	20.50	0.00	0.00	0.00
S_4	0.00	1.52	12.91	29.95	0.00	0.02	0.00	0.06
S_5	0.00	1.53	17.41	27.60	0.00	0.01	0.00	0.05
S_6	0.00	0.00	0.00	0.00	0.00	0.01	3.73	0.00
S_7	0.00	0.00	0.14	0.09	0.00	20.50	0.01	2.18
S_8	0.00	0.00	0.02	0.13	0.00	1.98	0.00	20.18

Table 5.4 – SOCs for the (6,0) CNT.

LR-TDDFT/PBE SOC values for the lowest 8 singlet and triplet states of the (6,0) CNT.

Finally, we also investigated the effects of thermal fluctuations on the magnitude of SOCs. To

this end, we performed ground-state Born-Oppenheimer MD at room temperature (300K) on a prototypical (6,0) CNT and analyzed the SOCs between singlet and triplet states for different configurations sampled along the trajectory. Fig. 5.7 shows the results for 12 MD frames separated from each other by ~ 230 fs. We observe that, compared to the optimized geometry (whose SOC value is indicated by the dashed line), the SOCs of the 'thermalized' structures are systematically lower by about 5-20 %, showing that temperature can have a considerable effect on SOCs. This suggests that, while the perfect curvature of the optimized structure gives rise to an increase of the SOCs (compared to flat graphene), the asymmetric distortions induced by thermal vibrations cause a deterioration of the orbital overlaps and the consequent decrease of the SOC.

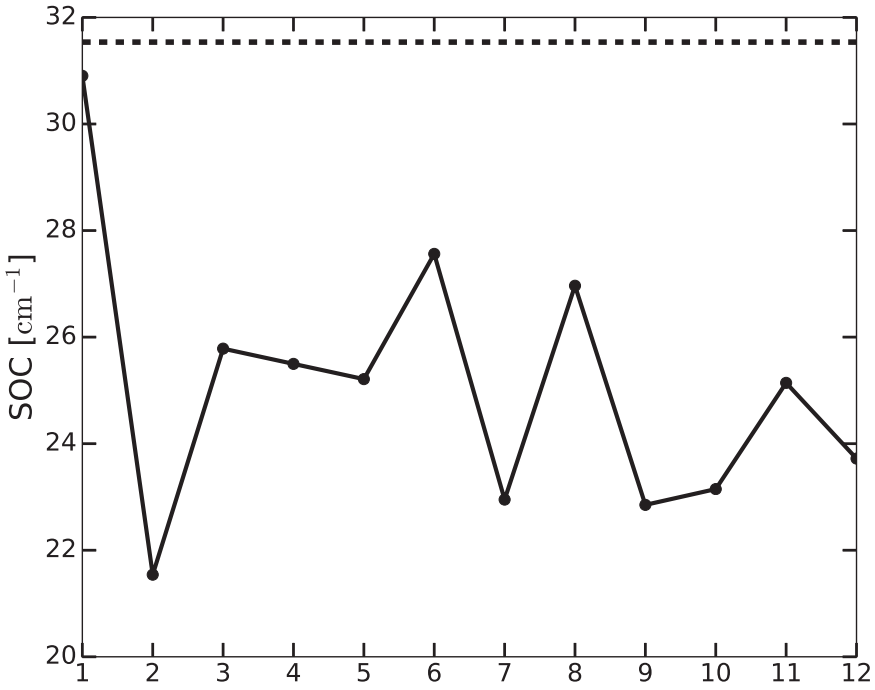

Figure 5.7 – SOC values for the (6,0) CNT.

LR-TDDFT/PBE SOC values (maximum over the fist 8 single and triplet states) for different geometries of the (6,0) CNT collected along the dynamics. The dashed line indicates the SOC value for the optimized geometry.

5.4.3 2D: Graphene

Graphene is the most extraordinary two-dimensional carbon material. For a perfectly flat graphene sheet, the TB model predicts very small SOC values in the order of the atomic spin-orbit splitting of isolated carbon atoms (~ 6 meV). However, the SOC in graphene differs for different positions (k-vectors) of the Brillouin zone and in particular it is greatly reduced at the

degeneracy point of the Dirac cones (the K-points) for which TB predicts values below 1 μ eV.

In this study we applied a supercell description of graphene generated from the fundamental hexagonal unit cell characterized by a lattice parameter $a = 2.46$ Å. The calculation were done on two types of supercells, both with hexagonal symmetry. The first supercell has dimensions 3x3 and composed by 18 carbon atoms. This is a peculiar choice characterized by the back-folding of the K-points onto Γ in reciprocal space, therefore offering the possibility to compute the electronic properties at the Dirac cone using a supercell calculation at the Γ point. Due to the degeneracy of the K-points we expected and obtained the first 4 LR-TDDFT transitions to be nearly zero, while the second tier of excitations (with finite energy gaps) corresponds to transitions between the π and σ^* KS states, which have notoriously large SOC contributions (see Fig. 5.8). The second supercell considered has a dimension 7x7 and is composed by 98 carbon atoms. In this case, the surface of the corresponding Brillouin zone in reciprocal space shrinks further, meaning that more points of the electronic bands fold back at Γ, including points of the Π and $\Pi*$ bands with, however, the exception of the K-points, which are not sampled in this case. For this supercell, the π and $\pi*$ states (sampled in the vicinity of the Dirac cone) dominate the density of states at the gap in Γ, therefore making the calculations of $\pi\sigma^*$, $\sigma\pi^*$ and $\sigma\sigma^*$ SOC calculations computationally very expensive, since a large number of solutions of the LR-TDDFT equations is required.

For the 3x3 supercell, the obtained a maximum SOC value of 68.65 cm^{-1} (8.51 meV), which falls within the 6 – 12 meV range evaluated with TB between σ and π bands at the Γ [143]. On

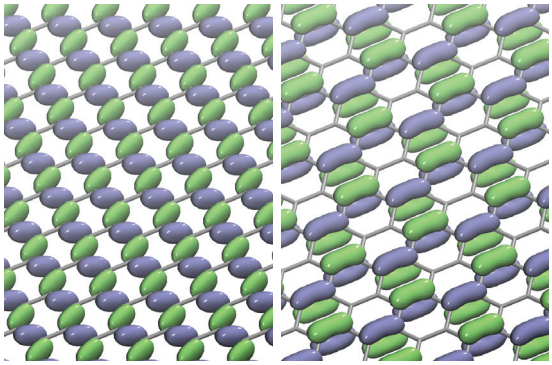

Figure 5.8 – KS-orbitals of graphene.

σ (left) and π (right), computed for the 3x3 supercell of graphene.

the other hand, the SOC between π and π^* bands at the K-point (for vanishing energy gaps) is of the order of 0.001 cm^{-1} (0.00012 meV), which, again, is in good agreement with TB the second-oder perturbation theory. In fact, as discussed in Section 5.2.1 due to symmetry arguments [153]TB predicts a vanishing SOC, that becomes finite only if second-nearest neighbor couplings between equivalent carbon atoms (AA or BB) are considered. It is important to stress that LR-TDDFT is able to reproduce this result without the need of introducing any modification of the functional, while second-order TB relies on a number of adjusted parameters.

The results obtained for 7x7 supercell are also in good agreement with the TB predictions. All SOC values fall in the range 0.000 - 0.001 cm^{-1}, meaning that the vanishing of the couplings extends to the entire π and π^* bands and is not limited to the K-points.

In summary, the calculations for flat graphene show a good agreement with the known experimental and TB results, validating therefore our LR-TDDFT/PBE implementation, which is able to capture quantitatively the different physical mechanisms at the origin of the SOC level splitting, without the need of any correction to the theory. A further topic of interest, is the characterization of the effect of the curvature on the SOC in corrugated graphene. However, due to the size of the supercell required for this type of investigation we will not address this issue directly. On the other hand, in the next Section we will explore the effect of the curvature on the value of SOCs by investigating the gas phase dynamics of a graphene GQD.

5.4.4 ISC dynamics of a graphene quantum dot

It is a well established result that ISCs in CQDs are in general less efficient than ICs due to large energy spacings between singlet and triplet states and weak SOCs. However, as shown in section 5.4.1, topological features and structural modifications (in particular changes of the curvature) can influence the strength of the SOCs and increase the ISC rates. In this section, we investigate the excited state nonadiabatic dynamics of the 0D nanoflake described in section 5.4.1 with the aim of shedding new light on the mechanism of ISC in a prototypical carbon nanostructure.

Description of the dynamics

After a ground state equilibration dynamics at 300K, the system is excited into the first singlet excited state, S_1 and propagated according to the LR-TDDFT based TSH⊗LZ nonadiabatic MD scheme described in section 5.2.2. This choice is motivated by the magnitude of the corresponding oscillator strength and by the fact that, due to the relatively small SOCs of CQDs, ISCs occur when the system is relaxed (through IC) in the lowest singlet state. Fig. 5.9 shows the time evolution of the energies of the states involved in the dynamics, namely S_1, S_2, together with T_2 and T_3. T_1 lies lower in energy and never interferes with the dynamics during the entire time span of our simulation. During the dynamics, the force state S_1 approaches the two triplet states T_2 and T_3, however it actually only intersects T_2 in several points. The time evolution of SOCs between S_1 and the triple states T_2 and T_3 is reported in Fig. 5.10. Both curves shows a very similar behavior, which is not surprising considering that both triplets share a very similar electronic character (note that the energy profiles, even though separated by about 0.2 eV, run almost parallel to each other). Since T_3 never crosses S_1 during the first 1ps of dynamics, ISC between these two states has negligible probability to occur. On the other hand, in the same time interval S_1 and T_2 intersect about 50 times; at each crossing point the the computed SOCs are small, but clearly measurable (between 0.1 and 2.5 cm^{-1}) giving rise to non-vanishing ISC probabilities.

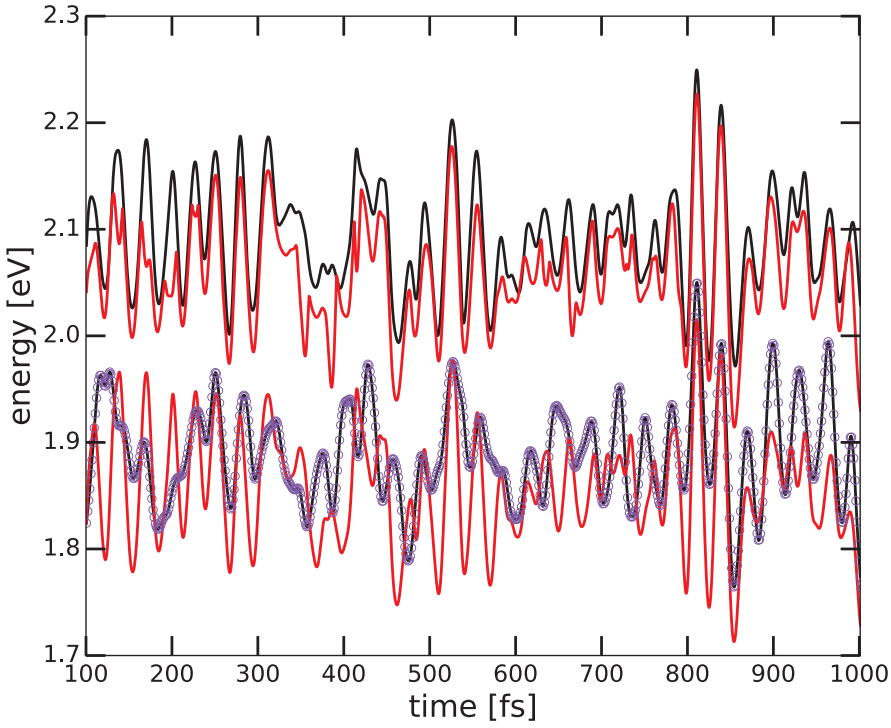

Figure 5.9 – Nanoflake dynamics (i).
Time evolution the singlet S_1, S_2 (black), and triplet T_2, T_3 (red) excited state energies evaluated during 1 ps of dynamics. Shown are the energy differences with respect to the ground-state (the excitation energy). The purple circles indicate the force state (i.e. the state that drives the dynamics in the TSH algorithm).

Of particular interest is the comparison of the time evolution of the S_1-T_2 SOCs with that of a structural parameter such as the overall curvature of the flake. These results are shown in Fig. 5.11. As a measure of the curvature we considered the distance between two hydrogen atoms at opposite ends of the molecule (see red lines in the insets in Fig. 5.11). This quantity is inversely proportional to the curvature, since this end-to-end distance decreases as the curvature increases. Notice that since the structure always bends along the same axes, only the selected distance gives a correct estimate of the curvature (with oscillations between 12.5 Å and 14.5 Å). The other, orthogonal, end-to-end distance varies less during the dynamics, oscillating fast around its mean value. Just as what we observed in the static calculations, there is a clear correlation between the magnitude of the SOC and the curvature of the sheet during the dynamics. As a consequence we expect an increase of the ISC probability every time the structure bents into a bowl shape. These results show that the effect of the curvature on magnitude of SOC is valid not only for extended carbon nanostructures such as graphene sheets and carbon nanotubes, but also holds for a finite-sized, low-symmetry molecules.

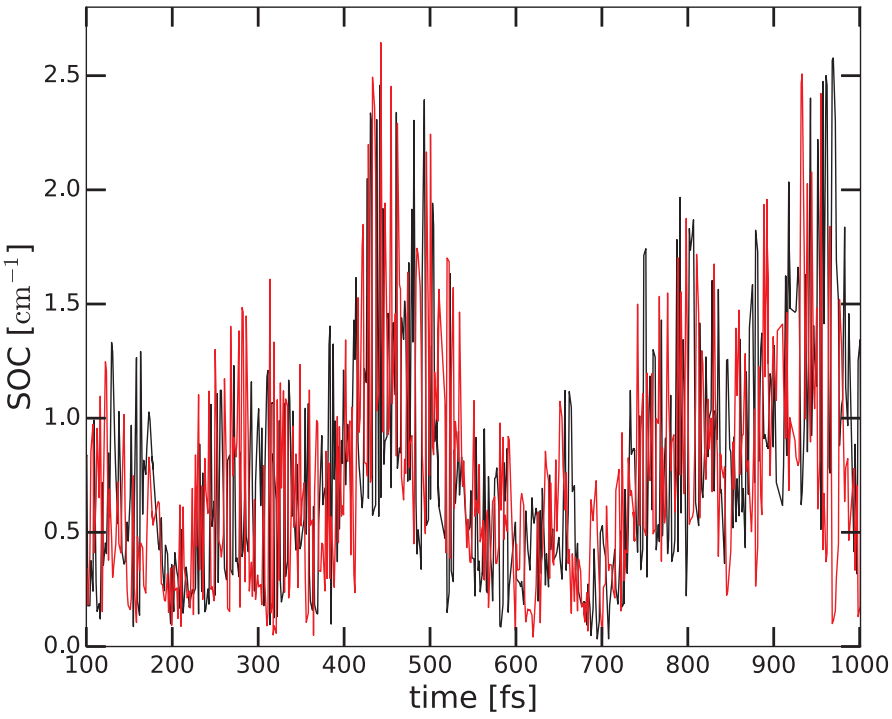

Figure 5.10 – Nanoflake dynamics (ii).

Time evolution of the SOC values between S_1 and T_2 and S_1 and T_3 evaluated during 1 ps of dynamics.

Estimation of the ISC rate

From the dynamics described in the previous section it is possible to derive a quantitative estimate of the ISC rate. As described in section 5.2.3, the probability for a singlet-to-triplet transition at a crossing point is given by the Landau-Zener formula in Eq. (5.14). In the most general case, the effective ISC rate calculation would require the average over an ensemble of trajectories. However, due to the relatively small values of SOCs, we do not expect any appreciable transition within the affordable time scale (1 ps) and therefore a single trajectory can become representative of the dynamics of the ensemble, which will behave as an homogeneous trajectory bundle. The total probability P_{ISC} of an ISC to occur (al least once) in a given time interval T is given by

$$P_{\mathrm{ISC}}(T) = 1 - \prod_{0}^{T} (1 - p_{LZ}(t)) \,, \tag{5.16}$$

where $p_{LZ}(t)$ is the Landau-Zener probability of a singlet-to-triplet ISC at time t (which is 0 away from the crossing points). As expected, the probability $P_{\mathrm{ISC}}(T)$ start from zero at $t = 0$ and converges to 1 as the final time T approaches infinity. Fig. 5.12 (black curve) reports the

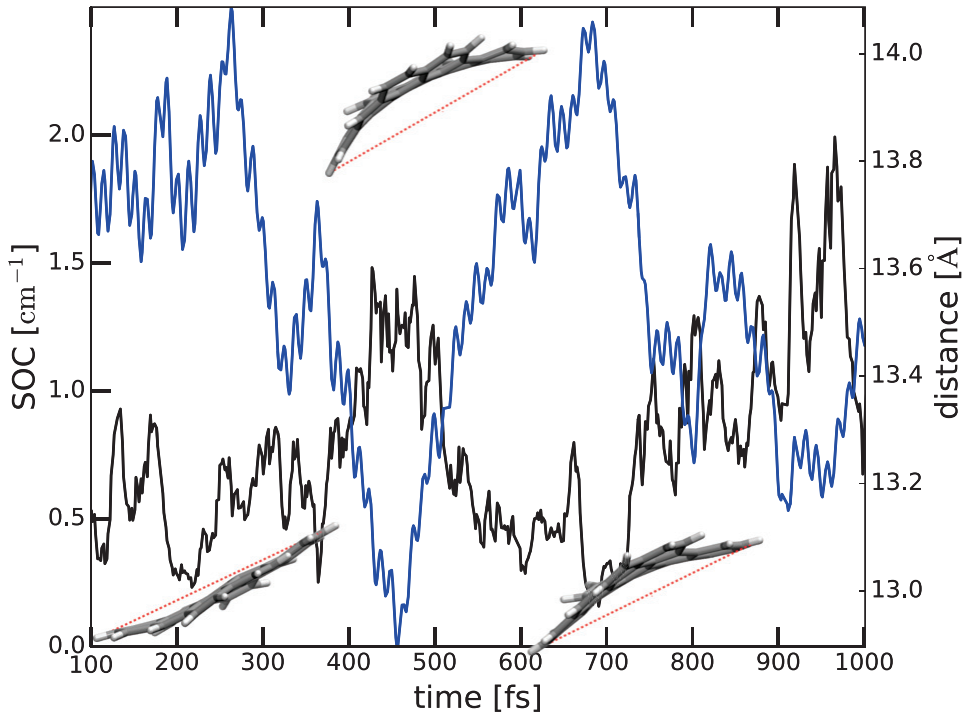

Figure 5.11 – Nanoflake dynamics (iii).

Time evolution of the SOC values for states S_1 and T_2 (black curve as in Fig. 5.10) and of the distance between two hydrogen atoms at opposite extremes of the nanoflake (dashed red lines in the insets). The insets show the structures of the nanoflake that correspond to the maxima and minima of the distance profile.

time evolution of $P_{\mathrm{ISC}}(T)$ in the time interval the [0, 1 ps]. Notice that $P_{\mathrm{ISC}}(T)$ undergoes two main "steps" at around 400 and 900 fs. These coincide with point along the trajectory where crossing occurs at relatively large values of the SOC matrix elements.

Considering the $S_1 \rightarrow T_2$ transition as a first-order process, we fitted the curve $P_{\mathrm{ISC}}(T)$ with an exponential function of the form $1 - e^{-k_{ISC}T}$, where k_{ISC} corresponds to the ISC rate constant, i.e. the inverse of the ISC lifetime τ_{ISC}. The fit (red line in Fig. 5.12) performed using the least squares routine of SciPy library [162] gives an estimation for k_{ISC} of about 2.1×10^{-6} fs^{-1} with a standard deviation of 8.5×10^{-8} fs^{-1}.

A direct comparison with experiments is not possible. However, the study of a similar but larger graphene nanoflake by Mueller *et al.* [128] revealed that, even though the SOCs are in average small (< 1 cm^{-1}), the measured phosphorescence rates are relatively fast with a rate constant in the order of the 1μ s. Interestingly enough, the authors explained this effect with an increase of the SOCs between singlet and triplet states induced by thermal structural distortions, which also favor singlet-triplet curve crossings. Our results confirm these predictions, highlighting

the importance of the curvature of the nanoflake.

Another interesting compound that share some similarities with our system is anthracene. This is a well studied carbon molecule composed of 3 benzene rings for which – as is the case of many smaller aromatic hydrocarbons – k_{ISC} is available from experiments. Unlike other aromatic hydrocarbons, which display mostly $S_1 \rightarrow T_1$ ISC, anthracene has $S_1 \rightarrow T_2$ ISC, just as in the case of the molecule of this study. This is an important factor that determines the relatively high ISC rate of anthracene; in fact, the small energy gap between S_1 and T_2 [3] induces many surface crossings that enhance the rate. The k_{ISC} for anthracene is of $5.0 \times 10^8 s^{-1}$, not far from what we estimated for the nanoflake ($2.1 \times 10^9 s^{-1}$). The difference of about one order of magnitude can be explained by the different sizes of the two systems.

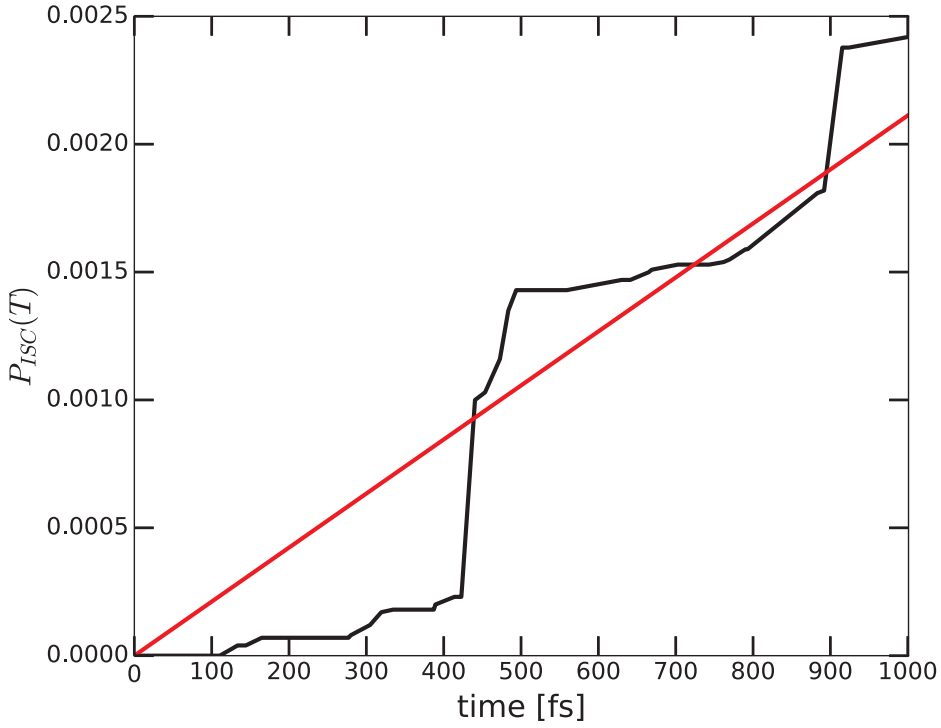

Figure 5.12 – Nanoflake dynamics (iv).

Time evolution of the total probability for ISC, $P_{\mathrm{ISC}}(T)$, calculated according to the formula (5.16) (black curve) together with the mono-exponential fit (red curve).

5.5 Conclusions

In this work, we applied the recently developed LR-TDDFT scheme for the calculation of SOC **??** to a series of carbon nanostructures in 0D (C60 and graphene nanoflakes), 1D (CNTs with different topologies), and 2D (graphene sheet). The results obtained for all measured electronic

structure properties including energy gaps, oscillator strengths, KS-orbital characters, and SOCs are in very good agreement with experiments and parameterized TB calculations. In the case of CNTs, LR-TDDFT is able to reproduce the gap closure in metallic systems as well as the dependence on the topological indices (n,m). Concerning the magnitude of the SOC, we observe vanishing small values at the K-points and a clear dependence on the CNT curvature, κ. However, differently form the TB predictions, the overall increase of the SOC values as a function of κ is strongly modulated by the topological nature of the CNT; in particular, chiral/achiral and metallic/semiconducting structures have different linear dependences (slopes). Finally, we observed that thermal distortions in CNTs produce a systematic decrease of the magnitude of the SOC by perturbing the optimal orbital overlap between σ and π electronic bands.

This finding also applies to other carbon nanostructures. In particular we investigated the dependence of the SOC values on the curvature for a prototypical 0D graphene nanoflake. Excited state dynamics at room temperature reveals a clear correlation between the magnitude of the SOC and the flake curvature measured along one of the main molecular axis. This has a significant impact on the ISC rate; when a singlet state crosses a triplet state at a maximally curved geometry the Landau-Zener transition probability becomes large, contributing significantly to the overall transition rate. As a consequence, while the SOC in a flat graphene nanoflake is in general very small (~ 0.25 cm^{-1}), in dynamics the ISC rate becomes appreciable ($\sim 2\times 10^9$ s^{-1}). This has important implications for applications in nanotechnology, as for instance in the realization of graphene based organic photovoltaic devices. In fact, large ISC rates allow for an efficient transfer of the photoexcited population into a triplet state, protecting the system from electron-hole back recombination and favoring therefore charge separation at the interface between the donor (the carbon nanoflake) and the acceptor (a polymer).

The proposed LR-TDDFT-based nonadiabatic dynamics scheme [47] has the necessary accuracy and computationally efficiency to become one of the most promising tools for the simulation of IC and ISC processes in medium to large carbon nanostructures, as well as other organic and inorganic chromophores in gas phase and in solution [146, 163, 96, 147, 164, 165].

6 Conclusion and Outlook

In recent years much progress has been made in the description of the photophysics of molecules, including nonadiabatic phenomena. Nonetheless, several obstacles remain to the accurate[1] simulation of molecules of even moderate size. The main bottleneck remains the calculation of electronic structure including excited state.
Very accurate electronic structure methods such as Full CI and CASSCF+MP2[2] run into what is known as the "exponential barrier", since their computational cost scales exponentially with the number of electrons in the system. This limits them to single-point calculations of relatively small molecules. Even when it is possible to perform dynamics using accurate wavefunction-based methods, they usually require that an active space be chosen, i.e. the "space" of molecular orbitals and the number of electrons that will be included in the calculation. As a consequence, these methods require that the computational chemist posses at least some knowledge of the results he wants to obtain. In other words, they cannot be totally predictive. These methods are especially tricky to use in dynamics, where the active space might change as the nuclei move.
DFT and TDDFT have a softer scaling [167, 33, 168, 41, 35, 36], but do not achieve the same level of accuracy. Moreover LR-TDDFT has limitations when dealing with certain systems of chemical interest, such as open-shell molecules, dissociation reactions, charge-transfer states and biradicals [36, 35, 169, 67]. Still, solving these problems is an active area of research and progress has been made, be it in the form of new xc-functionals [170, 171], the development of "spin-flip" LR-TDDFT methods [67, 169, 172] or even ideas on how to have frequency-dependent xc-kernels [173, 174, 175, 176, 177, 178]. Improving TDDFT methods in general is important not only to the description of ISC dynamics, but for excited-states dynamics and properties calculations in general, especially if we wish to treat large systems. Furthermore, the solution to these problems is necessary if we want to actually describe photochemistry and not only photophysical events preceding or following photochemical reactions, since many interesting photochemical reactions involve radicals and homolytic bond-breaking.

[1] Methods that achieve so-called "chemical accuracy" of 4.2 kJ/mol, allow to make quantitative prediction of chemical phenomena.

[2] Second-oder perturbation theory based on a complete active-space self-consistent field wavefunction [166].

Challenges more specific to this thesis and to the description of SOC and ISC are the inclusion of 2-electron SOC and the calculation of SOC for atoms with large cores, for which the calculation of SOC for all the electrons is limited by computational costs and the use of pseudopotentials. We have already worked to some extent on these problems, and inexpensive solutions, such as the use of effective SOC operators – containing a parametrized effective nuclear charge Z_{eff} that takes into account both the effects of the core and of the two-electron operator – can be implemented, but the cost to accuracy is unknown.
Moreover, it is very likely that in certain cases SOC must be included in Hamiltonian to be diagonalized, even in systems containing light atoms [92]. In systems containing heavy metal atoms, where SOC becomes very important, the perturbational treatment of relativistic effects quickly runs into its limits. Thus, research into including SOC and other relativistic effects into the Hamiltonian to be solved becomes necessary if molecular photophysics and photochemistry are to be explored in their most interesting cases using theoretical methods.
Despite all these challenges, this thesis has shown that it is indeed possible to use LR-TDDFT to perform excited-state dynamics simulations that include both ISC and, thanks to previous work, IC as well. Moreover, LR-TDDFT remains a very attractive method for excited-state calculations, because of its moderate cost and simplicity of use. The AMEW as method for calculating SOC has been shown to be reliable and it is therefore confirmed as promising method for the calculation of excited-states properties using LR-TDDFT.
For these reasons we hope to use our method to explore systems with interesting possible applications, especially in the domain of energy production and storage. The carbon nanostructures which we are currently studying are indeed examples of such system, since, as mentioned in the introduction of chapter 5 they have several prospective applications, including organic photovoltaics. Future studies may include metal complexes present in dye-sensitized solar cells or those found in organic light-emitting diodes, in which SOC and ISC play important roles.

A An appendix

Most of the derivations contained in this appendix are based on references [46] [45] [179] and [11].

A.1 Pauli reduction of the Dirac equation

We start by considering the hamiltonian given by equation (2.156):

$$H^{UESC} = T + V + (\boldsymbol{\sigma}\cdot\mathbf{p})\frac{(V-E)}{4m^2c^2}(\boldsymbol{\sigma}\cdot\mathbf{p})\,. \tag{A.1}$$

$$\psi^N = N\psi^L\,, \tag{A.2}$$

where ψ^N is the normalized wavefunction and N is the operator that normalizes ψ^N,

$$1 = \int \mathrm{d}\mathbf{r}\,\psi^{N\dagger}\psi^N = \int \mathrm{d}\mathbf{r}\,\psi^{L\dagger}N^\dagger N\psi^L = \int \mathrm{d}\mathbf{r}\,\psi^{L\dagger}\psi^L + \psi^{S\dagger}\psi^S\,, \tag{A.3}$$

we know that (see equations (2.146) and (2.148)):

$$\psi^S = K(E,\mathbf{r})\frac{(\boldsymbol{\sigma}\cdot\mathbf{p})}{2mc}\psi^L\,, \tag{A.4}$$

and substituting for ψ^S gives:

$$\int \mathrm{d}\mathbf{r}\, \psi^{L\dagger} N^\dagger N \psi^L = \int \mathrm{d}\mathbf{r}\, \psi^{L\dagger}\psi^L + \psi^{L\dagger}\left[(\boldsymbol{\sigma}\cdot\mathbf{p})\frac{K(E,\mathbf{r})^2}{4m^2c^2}(\boldsymbol{\sigma}\cdot\mathbf{p})\right]\psi^L$$
$$= \int \mathrm{d}\mathbf{r}\, \psi^{L\dagger}\left[1 + (\boldsymbol{\sigma}\cdot\mathbf{p})\frac{K(E,\mathbf{r})^2}{4m^2c^2}(\boldsymbol{\sigma}\cdot\mathbf{p})\right]\psi^L ,$$

we have:

$$N^\dagger N = \left[1 + (\boldsymbol{\sigma}\cdot\mathbf{p})\frac{K(E,\mathbf{r})^2}{4m^2c^2}(\boldsymbol{\sigma}\cdot\mathbf{p})\right] , \tag{A.5}$$

and by requiring that N be hermitian, equation (A.5) is solved simply by taking the square-root,

$$N = \left[1 + (\boldsymbol{\sigma}\cdot\mathbf{p})\frac{K(E,\mathbf{r})^2}{4m^2c^2}(\boldsymbol{\sigma}\cdot\mathbf{p})\right]^{1/2} , \tag{A.6}$$

in order to obtain a better expression for N, we expand the square root in a power series[1] :

$$N = 1 + \frac{1}{8m^2c^2}(\boldsymbol{\sigma}\cdot\mathbf{p})K(E,\mathbf{r})^2(\boldsymbol{\sigma}\cdot\mathbf{p}) + \dots , \tag{A.7}$$

now, expanding $K(E,\mathbf{r})^2$ in a power series as well gives:

$$N = 1 + \frac{1}{8m^2c^2}(\boldsymbol{\sigma}\cdot\mathbf{p})\left[1 + \frac{2(V-E)}{2mc^2}\right](\boldsymbol{\sigma}\cdot\mathbf{p}) + \dots$$
$$= 1 + \frac{1}{8m^2c^2}\mathbf{p}^2 + O(c^{-4}) . \tag{A.8}$$

Notice we need only use the first term of the expansion of $K(E,\mathbf{r})^2$ (i.e.: $K(E,\mathbf{r})^2 = 1$). This is acceptable, because in (A.8), all terms beyond $\frac{1}{8m^2c^2}\mathbf{p}^2$ are $O(c^{-4})$, and we only want terms that are up to $O(c^{-2})$.

The next step is to find how N affects the Hamiltonian H^{UESC}.

[1] The MacLaurin series for $\sqrt{1+x}$ is $1 + \frac{1}{2}x^2 + \dots$, here we take $(\boldsymbol{\sigma}\cdot\mathbf{p})K(E,\mathbf{r})^2(\boldsymbol{\sigma}\cdot\mathbf{p}) = x$

$$H^{UESC}\psi^L = E\psi^L \iff \tag{A.9}$$
$$H^{UESC}N^{-1}N\psi^L = E\psi^L \iff \tag{A.10}$$
$$H^{UESC}N^{-1}\psi^N = E\psi^L\,, \tag{A.11}$$

premultiplying by N,

$$NH^{UESC}N^{-1}\psi^N = NE\psi^L \iff \tag{A.12}$$
$$NH^{UESC}N^{-1}\psi^N = E\psi^N\,. \tag{A.13}$$

Evaluation of $NH^{UESC}N^{-1}\psi^N$ would yield the operator for ψ^N we are looking for. However, this operator would still contain "E". The "trick" here is to multiply (from the left) both sides of the last equation by N^{-2}. This will give:

$$N^{-1}H^{UESC}N^{-1}\psi^N = N^{-2}E\psi^N\,. \tag{A.14}$$

Let us first evaluate the LHS of this equation (keeping in mind that all terms above $O(c^{-2})$ are neglected!)[2]:

$$\begin{aligned}
&N^{-1}H^{UESC}N^{-1}\psi^N \qquad\qquad (A.15)\\
&=\left(1-\frac{1}{8m^2c^2}\mathbf{p}^2\right)\left[T+V+\frac{1}{4m^2c^2}\left((\boldsymbol{\sigma}\cdot\mathbf{P})(V-E)(\boldsymbol{\sigma}\cdot\mathbf{P})\right)\right]N^{-1}\psi^N\\
&=\left\{T+V+\frac{1}{4m^2c^2}\left[(\boldsymbol{\sigma}\cdot\mathbf{P})(V-E)(\boldsymbol{\sigma}\cdot\mathbf{P})-\frac{1}{2}(\mathbf{p}^2T+\mathbf{p}^2V)\right]\right\}N^{-1}\psi^N\\
&=\left\{T+V+\frac{1}{4m^2c^2}\left[(\boldsymbol{\sigma}\cdot\mathbf{P})(V-E)(\boldsymbol{\sigma}\cdot\mathbf{P})-\frac{1}{2}(\mathbf{p}^2T+V\mathbf{p}^2+T\mathbf{p}^2+\mathbf{p}^2V)\right]\right\}\psi^N\,,
\end{aligned}$$

knowing that $\mathbf{p}^2T = T\mathbf{p}^2 = \frac{\mathbf{p}^4}{2m}$, we get:

$$\begin{aligned}
&N^{-1}H^{UESC}N^{-1}\psi^N \qquad\qquad (A.16)\\
&=\left\{T+V+\frac{1}{4m^2c^2}\left[(\boldsymbol{\sigma}\cdot\mathbf{P})(V-E)(\boldsymbol{\sigma}\cdot\mathbf{P})-\mathbf{p}^2T-\frac{1}{2}(V\mathbf{p}^2+\mathbf{p}^2V)\right]\right\}\psi^N\,. \qquad (A.17)
\end{aligned}$$

[2] We obtain N^{-1} by taking the inverse square root of (A.5) and expanding it up to $O(c^{-2})$ and then expanding $K(E,\mathbf{r})$ as well, just like we did to obtain N.

In order to compute the first and last terms inside the brackets we have to remember that **p** is a differential operator. By denoting compound operators with parentheses and an arbitrary function by f:

$$\begin{aligned}&\mathbf{p}^2 V f = \mathbf{p}\mathbf{p} V f = \mathbf{p}[\mathbf{p}(Vf)] = \mathbf{p}[(\mathbf{p}V)f + V(\mathbf{p}f)] = (\mathbf{p}^2 V)f + 2(\mathbf{p}V)(\mathbf{p}f) + V\mathbf{p}^2 f \\ &\Rightarrow \mathbf{p}^2 V = (\mathbf{p}^2 V) + 2(\mathbf{p}V)\mathbf{p} + V\mathbf{p}^2 \,, \end{aligned} \tag{A.18}$$

now we can evaluate:

$$\frac{1}{2}(\mathbf{p}^2 V + V\mathbf{p}^2) = -\hbar^2(\frac{1}{2}(\nabla^2 V) + (\nabla V)\cdot\nabla + V\nabla^2) \,, \tag{A.19}$$

and by noting that:

$$\mathbf{p}V\mathbf{p} = \frac{1}{2}[\mathbf{p}V\mathbf{p} + \mathbf{p}V\mathbf{p}] \tag{A.20}$$

$$= \frac{1}{2}[(\mathbf{p}V)\mathbf{p} + V\mathbf{p}^2 + (\mathbf{p}V)\mathbf{p} + V\mathbf{p}^2 - (\mathbf{p}^2 V) + (\mathbf{p}^2 V)] \,, \tag{A.21}$$

$$\tag{A.22}$$

and using (A.18) we get:

$$= \frac{1}{2}[V\mathbf{p}^2 + \mathbf{p}^2 V - (\mathbf{p}^2 V)] \,, \tag{A.23}$$

which allows us to evaluate:

$$(\boldsymbol{\sigma}\cdot\mathbf{P})(V-E)(\boldsymbol{\sigma}\cdot\mathbf{P}) = -\hbar^2((\nabla V)\cdot\nabla + V(\nabla^2) + \hbar\boldsymbol{\sigma}\cdot(\nabla V)\times\mathbf{p} - E\mathbf{p}^2 \,, \tag{A.24}$$

so the LHS of (A.14) is:

$$N^{-1}H^{UESC}N^{-1}\psi^N \tag{A.25}$$

$$=\left\{T+V-E\mathbf{p}^2-\frac{1}{8m^3c^2}\mathbf{p}^4+\frac{\hbar^2}{8m^3c^2}(\nabla^2V)+\frac{\hbar}{8m^3c^2}\boldsymbol{\sigma}\cdot(\nabla V)\times\mathbf{p}\right\}\psi^N\,. \tag{A.26}$$

Now, the RHS is simply:

$$EN^{-2}\psi^N=\left(E-\frac{E}{4m^2c^2}\mathbf{p}^2\right)\psi^N\,. \tag{A.27}$$

The two $\frac{E}{4m^2c^2}\mathbf{p}^2$ terms (on each side (A.14) of cancel out, which leads us to our final result:

$$\left\{T+V-\frac{1}{8m^3c^2}\mathbf{p}^4+\frac{\hbar^2}{8m^2c^2}(\nabla^2V)+\frac{\hbar}{4m^2c^2}\boldsymbol{\sigma}\cdot(\nabla V)\times\mathbf{p}\right\}\psi^N=\quad H^{Pauli}\psi^N=E\psi^N\,. \tag{A.28}$$

As stated in the main text, this can be written as:

$$H^{Pauli}=H^{Schrödinger}+H^{mass-velocity}+H^{Darwin}+H^{SO}\,, \tag{A.29}$$

so let us take a closer look at the relativistic corrections other than spin-orbit coupling.

The energy of a particle of rest mass m in classical relativistic terms is:

$$E-V=c\sqrt{\mathbf{p}^2+m^2c^2}=mc^2\sqrt{1+\left(\frac{\mathbf{p}}{mc}\right)^2}\,, \tag{A.30}$$

if we take the McLaurin series of this expression, with $\frac{\mathbf{p}}{mc}$ as the variable, we get:

$$E-V=mc^2+\frac{1}{2}\frac{\mathbf{p}^2}{m}-\frac{1}{8}\frac{\mathbf{p}^4}{m^3c^2}\,, \tag{A.31}$$

the first term on the RHS of the above equation is the rest mass, the second term is the kinetic energy and the last term can be identified as the mass-velocity term, the first relativistic

correction to the (kinetic) energy due to the fact that mass increases with velocity.

The Darwin term does not have a straightforward classical interpretation, but is often interpreted as being due to the non-locality of the interaction between the electrostatic field V and the electron due to "Zwitterbewegung" [48]. This term can be recast by knowing that[3]:

$$\nabla^2(1/r) = -4\pi\delta(\mathbf{r})\,, \tag{A.32}$$

considering $-V = \frac{Z}{r}$, we have:

$$H^{Darwin} = \frac{\pi\hbar^2 Z}{2m^2c^2}\delta(\mathbf{r})\,. \tag{A.33}$$

A.2 The Breit equation

The Dirac equation describes one electron interacting with an electromagnetic field. In the case of a single-electron atoms, the electromagnetic field is created by the nucleus. Moreover, in the frame-of-reference of the nucleus, we need only consider the electrostatic interaction ($\mathbf{A} = \mathbf{0}$). How to generalize the Dirac equation to a two-electron (or multi-electron) system? Let us consider one Dirac equation for each electron separately:

$$\left[-E_1 + c\boldsymbol{\alpha}_1\cdot(\mathbf{p}_1 - e\mathbf{A}^{(2)}) + \beta_1 mc^2 + e\phi^{(2)} + V_1\right]\psi_1(\mathbf{r}_2) = 0 \tag{A.34}$$

$$\left[-E_2 + c\boldsymbol{\alpha}_2\cdot(\mathbf{p}_2 - e\mathbf{A}^{(1)}) + \beta_1 mc^2 + e\phi^{(1)} + V_2\right]\psi_2(\mathbf{r}_2) = 0\,, \tag{A.35}$$

where the subscripts indicate if the quantity relates to electron 1 or 2. V_i is the electrostatic potential generated by the (single) nucleus. Notice the superscripts on the vector potentials $\mathbf{A}^{(i)}$ and electrostatic potentials $\phi^{(i)}$; they are there to emphasize that electron 1 interacts with electron 2 via the potential generated by the latter and vice-versa. So although each one of these equations describes the interaction of a given electron with an electromagnetic field, this field is generated (in part) by the other electron, which means the equations are coupled. We now note that one can write an equation for the two electron system by taking the Kronecker product of each single electron Hamiltonian with the 4-by-4 identity matrix and adding them up to generate the Hamiltonian for the two-electron system:

[3] In spherical coordinates, the part of the Laplacian that acts on r is $\frac{1}{r^2}\frac{\partial}{\partial r}\left(r^2\frac{\partial}{\partial r}\right)$

$$\Big\{\left[-E_1 + c\boldsymbol{\alpha}_1 \cdot (\mathbf{p}_1 - e\mathbf{A}^{(2)}) + \beta_1 mc^2 + e\phi^{(2)} + V_1\right] \otimes I_4 + \tag{A.36}$$

$$\otimes I_4 \left[-E_2 + c\boldsymbol{\alpha}_2 \cdot (\mathbf{p}_2 - e\mathbf{A}^{(1)}) + \beta_1 mc^2 + e\phi^{(1)} + V_2\right]\Big\}\psi(\mathbf{r}_1, \mathbf{r}_2) \tag{A.37}$$

where $\psi(\mathbf{r}_1, \mathbf{r}_2) = \psi_1(\mathbf{r}_2) \otimes \psi_2(\mathbf{r}_2)$. We do this, because the states (spinors) of electron 1 live in $\mathscr{H}_1$, a Hilbert space inhabited by square-integrable 4-spinors. The same holds for electron 2, so the states of the 2-electron system live in $\mathscr{H}_1 \otimes \mathscr{H}_2$, which means that the operators acting on this space have a 16-by-16 matrix structure (instead of 4-by-4), and the wavefunction $\psi(\mathbf{r}_1, \mathbf{r}_2)$ is a 16-component spinor. We will therefore have 16 equations to solve, the equations for the the large and small components (for each electron) are coupled through the action of the α matrices and the equations for each electron (large and small components) are coupled as a consequence of the fact that the potentials acting on each electron are generated by the other electron. This means that if in theory we could solve the set of equations for electron one exactly, then we would know the exact form of the potentials acting on electron two (without even having to reference the source) and we would also be able to solve the set of equations for electron two. In this case the components of the wavefunction describing the two-electron system could be factorized into products of functions depending individually on the coordinates for just one electron (although the product of these single-electron functions would depend on the coordinates for both electrons). This is analogous to the problems found in solving the electronic SE, but here we cannot even write the Hamiltonian explicitly without making approximations!

Now we need to find an approximate form of $\mathbf{A}^{(1)}$, $\mathbf{A}^{(2)}$, $\phi^{(1)}$ and $\phi^{(2)}$. We will construct a two-electron Hamiltonian of the type:

$$H = H_1 + H_2 + H_{12}\,, \tag{A.38}$$

that is to say, a Hamiltonian that is the sum of the two one electron Hamiltonians plus an interaction term H_{12} containing the interaction potentials. The fastest way to go about this is to take the classical (relativistic) approximate expression for the potential energy resulting from the interaction between two charged particles (electrons, in this case) [48] [45, page 64] [46, pages 243-249]:

$$V_{12} = \frac{e^2}{r_{12}}\left[1 - \frac{1}{2}\frac{\mathbf{u}_1 \cdot \mathbf{u}_2}{c^2} - \frac{(\mathbf{u}_1 \cdot \mathbf{r}_{12})(\mathbf{u}_2 \cdot \mathbf{r}_{12})}{c^2 r_{12}^2}\right] \tag{A.39}$$

This expression for the interaction energy is approximate because in general, within a relativis-

tic framework, $V_{12} \neq V_{21}$ (which means the interaction energy would not be symmetric with respect to the electron indices) and this would pose a an obvious problem for constructing and operator in quantum mechanics. Moreover, in order to arrive to the above expression, it is assumed that interactions between particles are instantaneous (they are not, because the speed of light is finite). Also note that, in the Coulomb gauge, $\mathbf{A} = \mathbf{u}\frac{\phi}{c^2}$, and this was used in the derivation for the expression of V_{12} [45, page 64]. In order to obtain an expression for H_{12} the final step is to interpret the velocities $\mathbf{u}_1$ and $\mathbf{u}_2$ as the Dirac velocity operators $c\boldsymbol{\alpha}_1$ and $c\boldsymbol{\alpha}_2$. This is a heuristic derivation of the Breit equation, a rigorous derivation can be done within the framework of quantum electro-dynamics [45, page 64] [46, page 256]. Now we can write the Breit equation:

$$\left\{ \left[c\boldsymbol{\alpha}_1 \cdot \mathbf{p}_1 + \beta_1 mc^2 + V_1 + c\boldsymbol{\alpha}_2 \cdot \mathbf{p}_2 + \beta_2 mc^2 + V_2 \right] + \right. \tag{A.40}$$

$$\left. \frac{e^2}{r_{12}} \left[1 - \frac{\boldsymbol{\alpha}_1 \cdot \boldsymbol{\alpha}_2}{2} - \frac{(\boldsymbol{\alpha}_1 \cdot \mathbf{r}_{12})(\boldsymbol{\alpha}_2 \cdot \mathbf{r}_{12})}{r_{12}^2} \right] \right\} \psi(\mathbf{r}_1, \mathbf{r}_2) = E\psi(\mathbf{r}_1, \mathbf{r}_2) \,, \tag{A.41}$$

which can be re-written as:

$$[h_1^D + h_2^D + B_{12}]\psi(\mathbf{r}_1, \mathbf{r}_2) = E\psi(\mathbf{r}_1, \mathbf{r}_2) \tag{A.42}$$

where h_1^D, h_2^D are the Dirac one-electron operators and B_{12} is the Breit operator:

$$B_{12} = \frac{e^2}{r_{12}} \left[1 - \frac{\boldsymbol{\alpha}_1 \cdot \boldsymbol{\alpha}_2}{2} - \frac{(\boldsymbol{\alpha}_1 \cdot \mathbf{r}_{12})(\boldsymbol{\alpha}_2 \cdot \mathbf{r}_{12})}{r_{12}^2} \right] \tag{A.43}$$

which includes a Coulomb term $\frac{e^2}{r_{12}}$. The other terms are relativistic corrections to the coulomb potential. There is confusion in the literature about whether or not these corrections arise from retardation effects.

The Breit equation can be generalized to a many-electron system:

$$\left[\sum_i h_1^D + \sum_i h_2^D + \sum_i \sum_{\substack{j \\ j>i}} B_{12} \right] \psi(\mathbf{r}_1, \mathbf{r}_2) = E\psi(\mathbf{r}_1, \mathbf{r}_2) \tag{A.44}$$

with the sums running over all electrons.

A.2.1 The quasi-relativistic Breit equation

The Breit equation approximately describes a two electron system. Now we would like to have the Breit equation in a quasi relativistic form, which will introduce further approximations into the equation. It is important to realize that we will be dealing with two kinds of approximations. The first kind involves writing down an approximate two-electron (or many-electron) Hamiltonian, because the exact form of the Hamiltonian is unknown. The resulting equation (the Breit equation) still has a 4^N-component wavefunction (N is the number of electrons) as its solution. The second kind of approximation that will be introduced is the elimination of the small component in order to obtain a Schrödinger-like (or rather, Pauli-like) equation that involves a 2^N-component wavefunction (only large components). The quasi-relativistic Breit equation can be derived from the original Breit equation through a procedure similar to that used in appendix A.1 . It can also be obtained using the so-called first-order Foldy-Wouthuysen transformations [46, page 484]. Unfortunately this reduction is a lengthy procedure and we will content ourselves with simply showing the result. The so-called Breit-Pauli Hamiltonian for a N electron atom is:

$$H^{BP} = \sum_i \left[\frac{\mathbf{p}_i^2}{2m} - \frac{Z}{r_i} - \frac{\mathbf{p}_i^4}{8m^3c^2} + \frac{\pi\hbar^2 Z}{2m^2c^2}\delta(\mathbf{r_i}) + \frac{Z}{2mc^2r^3}\mathbf{s}_i\cdot\mathbf{l_i} \right] \tag{A.45}$$

$$\sum_i \sum_{\substack{j \\ j>i}} \left[\frac{1}{r_{ij}} - \frac{1}{2m^2c^2}\left(\frac{1}{r_{ij}}\mathbf{p}_i\cdot\mathbf{p}_j + \frac{1}{r_{ij}^3}(\mathbf{r}_{ij}(\mathbf{r}_{ij}\cdot\mathbf{p}_j)\cdot\mathbf{p}_i) \right) - \frac{\pi\hbar^2}{m^2c^2}\delta(\mathbf{r}_{ij}) \right. \tag{A.46}$$

$$- \frac{1}{m^2c^2}\frac{(\mathbf{s}_i + 2\mathbf{s}_j)\cdot(\mathbf{r}_{ij}\times\mathbf{p}_i)}{r_{ij}^3} - \frac{8\pi}{3m^2c^2}(\mathbf{s}_i\cdot\mathbf{s}_j)\delta(\mathbf{r_{ij}}) \tag{A.47}$$

$$\left. + \frac{1}{m^2c^2}\left(\frac{(\mathbf{s}_i\cdot\mathbf{s}_j)}{r_{ij}^3} - \frac{3(\mathbf{s}_i\cdot\mathbf{r}_{ij})(\mathbf{s}_i\cdot\mathbf{r}_{ij})}{r_{ij}^5} \right) \right] \tag{A.48}$$

All the one-electron operators were collected in the first pair of brackets on the RHS of the equation. We can see that this is just the Pauli Hamiltonian. The second pair of brackets include all the two-electron operators, the first one being the coulomb interaction, followed by the so-called orbit-orbit terms (in parenthesis, proportional to $\frac{1}{2m^2c^2}$) and then by the two-electron Darwin term ($\delta(\mathbf{r}_{ij})$). The operator:

$$-\frac{1}{m^2c^2}\frac{(\mathbf{s}_i+2\mathbf{s}_j)\cdot(\mathbf{r}_{ij}\times\mathbf{p}_i)}{r_{ij}^3}=-\frac{1}{m^2c^2}\left[\frac{(\mathbf{s}_i\cdot(\mathbf{r}_{ij}\times\mathbf{p}_i))}{r_{ij}^3}+\frac{2(\mathbf{s}_j\cdot(\mathbf{r}_{ij}\times\mathbf{p}_i))}{r_{ij}^3}\right] \tag{A.49}$$

$$=-\frac{1}{m^2c^2}\left[\frac{(\mathbf{r}_{ij}\cdot(\mathbf{p}_i\times\mathbf{s}_i))}{r_{ij}^3}+\frac{2(\mathbf{r}_{ij}\cdot(\mathbf{p}_i\times\mathbf{s}_j))}{r_{ij}^3}\right] \tag{A.50}$$

Is the two-electron spin-orbit coupling operator. The first term inside the brackets on the RHS of the last equation is referred to as the two-electron spin-own-orbit term. Notice that unlike the spin-own-orbit term appearing in the Pauli Hamiltonian this term involves r_{ij}, and that is why is a two-electron term. The second term known as the spin-other-orbit term, and involves spin and momentum operators of different electrons.

B An appendix

Consider Casida's equation $\Omega \mathbf{F}_I = \omega_I \mathbf{F}_I$. We can write the matrix Ω in block-matrix form by arranging its elements according to their spin index

$$\begin{pmatrix} \Omega_{\alpha\alpha} & \Omega_{\alpha\beta} \\ \Omega_{\beta\alpha} & \Omega_{\beta\beta} \end{pmatrix}, \tag{B.1}$$

and in the case of a closed shell molecule this matrix becomes even simpler because the ground state density is not spin-polarized, thus $\Omega_{\alpha\beta} = \Omega_{\beta\alpha}$ and $\Omega_{\alpha\alpha} = \Omega_{\beta\beta}$.

Starting from

$$\Omega = \begin{pmatrix} \Omega_{\alpha\alpha} & \Omega_{\alpha\beta} \\ \Omega_{\alpha\beta} & \Omega_{\alpha\alpha} \end{pmatrix}, \tag{B.2}$$

and applying the unitary transformation $U = \left(\begin{smallmatrix} 1\!1 & 1\!1 \\ 1\!1 & -1\!1 \end{smallmatrix}\right)$

$$U^\dagger \Omega U = \begin{pmatrix} \Omega_{\alpha\alpha} + \Omega_{\alpha\beta} & 0 \\ 0 & \Omega_{\alpha\alpha} - \Omega_{\alpha\beta} \end{pmatrix}, \tag{B.3}$$

we get a block diagonal matrix, and therefore we can solve the sub-problems separately

$$(\Omega_{\alpha\alpha} + \Omega_{\alpha\beta})\mathbf{f}^S = \omega_S^2 \mathbf{f}^S \tag{B.4}$$

and

$$(\Omega_{\alpha\alpha} - \Omega_{\alpha\beta})\mathbf{f}^T = \omega_T^2 \mathbf{f}^T, \tag{B.5}$$

and use their solutions to find the eigenvectors of $U^\dagger \Omega U$, which are

$$\mathbf{F}^S = \begin{pmatrix} \mathbf{f}^S \\ 0 \end{pmatrix} \text{and } \mathbf{F}^T = \begin{pmatrix} 0 \\ \mathbf{f}^T \end{pmatrix}. \tag{B.6}$$

Using U to get the solutions the original problem, we finally get

$$U\mathbf{F}^S = \begin{pmatrix} \mathbf{f}^S \\ \mathbf{f}^S \end{pmatrix} \text{and } U\mathbf{F}^T = \begin{pmatrix} \mathbf{f}^T \\ -\mathbf{f}^T \end{pmatrix}, \tag{B.7}$$

which shows how the solutions of Casida's equations indeed display the pattern that makes the AMEW be either a singlet or a triplet. The same result also holds within the Sternheimer formulation of LR-TDDFT.

C An appendix

From Eq. (3.8) we observe that for each matrix element evaluated for Slater determinants (SD) we will need to compute $N \times N$ one-electron matrix elements. If we consider a four-electron system with ground state wavefunction $|\Psi_0\rangle = |1\ \bar{1}\ 2\ \bar{2}\rangle$, this means a total $4 \times 4 \times 16$ one-electron matrix elements for $\langle S_1^0|\hat{H}_{1el}^{SO}|T_1^0\rangle$ and $4 \times 4 \times 8$ for $\langle S_1^0|\hat{H}_{1el}^{SO}|T_1^{-1,+1}\rangle$. Fortunately, since the linear-response orbitals are orthogonal to the ground state KS orbitals, it is possible to simplify this task by deriving new rules to compute these matrix elements. Let us first look at $\langle S_1^0|\hat{H}_{1el}^{SO}|T_1^0\rangle$. In our four-electron system, we have

$$
\begin{aligned}
&\langle \psi_S|\hat{H}^{SO}|\psi_T\rangle = \qquad\qquad (C.1)\\
&\langle \phi_1^S\ \bar{1}\ 2\ \bar{2}|\overset{(1)}{\hat{H}^{SO}}|\phi_1^T\ \bar{1}\ 2\ \bar{2}\rangle + \langle \phi_1^S\ \bar{1}\ 2\ \bar{2}|\overset{(2)}{\hat{H}^{SO}}|1\ \bar{\phi}_1^T\ 2\ \bar{2}\rangle + \langle \phi_1^S\ \bar{1}\ 2\ \bar{2}|\overset{(3)}{\hat{H}^{SO}}|1\ \bar{1}\ \phi_2^T\ \bar{2}\rangle +\\
&\langle \phi_1^S\ \bar{1}\ 2\ \bar{2}|\overset{(4)}{\hat{H}^{SO}}|1\ \bar{1}\ 2\ \bar{\phi}_2^T\rangle + \langle 1\ \bar{\phi}_1^S\ 2\ \bar{2}|\overset{(5)}{\hat{H}^{SO}}|\phi_1^T\ \bar{1}\ 2\ \bar{2}\rangle + \langle 1\ \bar{\phi}_1^S\ 2\ \bar{2}|\overset{(6)}{\hat{H}^{SO}}|1\ \bar{\phi}_1^T\ 2\ \bar{2}\rangle +\\
&\langle 1\ \bar{\phi}_1^S\ 2\ \bar{2}|\overset{(7)}{\hat{H}^{SO}}|1\ \bar{1}\ \phi_2^T\ \bar{2}\rangle + \langle 1\ \bar{\phi}_1^S\ 2\ \bar{2}|\overset{(8)}{\hat{H}^{SO}}|1\ \bar{1}\ 2\ \bar{\phi}_2^T\rangle + \langle 1\ \bar{1}\ \phi_2^S\ \bar{2}|\overset{(9)}{\hat{H}^{SO}}|\phi_1^T\ \bar{1}\ 2\ \bar{2}\rangle +\\
&\langle 1\ \bar{1}\ \phi_2^S\ \bar{2}|\overset{(10)}{\hat{H}^{SO}}|1\ \bar{\phi}_1^T\ 2\ \bar{2}\rangle + \langle 1\ \bar{1}\ \phi_2^S\ \bar{2}|\overset{(11)}{\hat{H}^{SO}}|1\ \bar{1}\ \phi_2^T\ \bar{2}\rangle + \langle 1\ \bar{1}\ \phi_2^S\ \bar{2}|\overset{(12)}{\hat{H}^{SO}}|1\ \bar{1}\ 2\ \bar{\phi}_2^T\rangle +\\
&\langle 1\ \bar{1}\ 2\ \bar{\phi}_2^S|\overset{(13)}{\hat{H}^{SO}}|\phi_1^T\ \bar{1}\ 2\ \bar{2}\rangle + \langle 1\ \bar{1}\ 2\ \bar{\phi}_2^S|\overset{(14)}{\hat{H}^{SO}}|1\ \bar{\phi}_1^T\ 2\ \bar{2}\rangle + \langle 1\ \bar{1}\ 2\ \bar{\phi}_2^S|\overset{(15)}{\hat{H}^{SO}}|1\ \bar{1}\ \phi_2^T\ \bar{2}\rangle +\\
&\langle 1\ \bar{1}\ 2\ \bar{\phi}_2^S|\overset{(16)}{\hat{H}^{SO}}|1\ \bar{1}\ 2\ \bar{\phi}_2^T\rangle .
\end{aligned}
$$

Only eight out of these sixteen matrix elements will be non-zero and we are able to distinguish two cases in which this happens. The first one is when the two SDs in the matrix element are created by the same excitation. This happens with matrix elements (1), (6), (11) and (16) in Eq. (C.1). Let us see what happens when we apply Eq. (3.8) to matrix elements (1). The overlap

matrix (Eq. (3.9)) will be

$$S_{ST} = \begin{pmatrix} \langle \phi_1^S | \phi_1^T \rangle & 0 & 0 & 0 \\ 0 & 1 & 0 & 0 \\ 0 & 0 & 1 & 0 \\ 0 & 0 & 0 & 1 \end{pmatrix}. \tag{C.2}$$

Notice that only four of the possible cofactors will give non-zero contributions, namely those defined by the elements along the diagonal. These will give

$$(-1)^{2+2} \begin{vmatrix} \langle \phi_1^S | \phi_1^T \rangle & \square & 0 & 0 \\ \square & \square & \square & \square \\ 0 & \square & 1 & 0 \\ 0 & \square & 0 & 1 \end{vmatrix} = \begin{vmatrix} \langle \phi_1^S | \phi_1^T \rangle & 0 & 0 \\ 0 & 1 & 0 \\ 0 & 0 & 1 \end{vmatrix} = \langle \phi_1^S | \phi_1^T \rangle , \tag{C.3}$$

or

$$(-1)^{1+1} \begin{vmatrix} \square & \square & \square & \square \\ \square & 1 & 0 & 0 \\ \square & 0 & 1 & 0 \\ \square & 0 & 0 & 1 \end{vmatrix} = \begin{vmatrix} 1 & 0 & 0 \\ 0 & 1 & 0 \\ 0 & 0 & 1 \end{vmatrix} = 1 , \tag{C.4}$$

and therefore, using the rule given in Eq. (3.8), the matrix element (1) will become

$$(1) = \langle \phi_1^S | \hat{h}^{SO} | \phi_1^T \rangle + \langle \bar{1} | \hat{h}^{SO} | \bar{1} \rangle \langle \phi_1^S | \phi_1^T \rangle + \\ \langle 2 | \hat{h}^{SO} | 2 \rangle \langle \phi_1^S | \phi_1^T \rangle + \langle \bar{2} | \hat{h}^{SO} | \bar{2} \rangle \langle \phi_1^S | \phi_1^T \rangle .$$

The other case in which a matrix element between SDs will be non-zero is when the determinants are created by different excitations (excitations from different occupied KS orbitals), and the linear-response orbitals have the same spin. This happens with matrix elements (3), (8), (9) and (14) in Eq. (C.1). Let us take a closer look at how to apply Eq. (3.8) to the matrix element (3). First of all, the overlap matrix becomes

$$S_{ST} = \begin{pmatrix} 0 & 0 & \langle \phi_1^S | \phi_2^T \rangle & 0 \\ 0 & 1 & 0 & 0 \\ 0 & 0 & 0 & 0 \\ 0 & 0 & 0 & 1 \end{pmatrix}, \tag{C.5}$$

from which we can clearly see that only one cofactor will be non-zero, namely

$$(-1)^{(1+3)} \begin{pmatrix} \square & 0 & \langle \phi_1^S | \phi_2^T \rangle & 0 \\ \square & 1 & 0 & 0 \\ \square & \square & \square & \square \\ \square & 0 & 0 & 1 \end{pmatrix} = \begin{vmatrix} 0 & \langle \phi_1^S | \phi_2^T \rangle & 0 \\ 1 & 0 & 0 \\ 0 & 0 & 1 \end{vmatrix} = - \begin{vmatrix} \langle \phi_1^S | \phi_2^T \rangle & 0 & 0 \\ 0 & 1 & 0 \\ 0 & 0 & 1 \end{vmatrix} = - \langle \phi_1^S | \phi_2^T \rangle , \tag{C.6}$$

from which we finally get

$$(3) = -\langle 1\,|\hat{h}^{SO}|\,2\,\rangle\langle\phi_2^T|\phi_2^T\rangle\,. \tag{C.7}$$

Matrix elements (2), (4), (5), (7), (10), (12), (13) and (15) will all be zero.
Concerning the triplets $|T_1^{+1}\rangle$ and $|T_1^{-1}\rangle$, only eight matrix elements will have to be computed. As an example, we compute

$$\begin{aligned}
&\langle S_0^0|\hat{H}^{SO}|T^{-1}\rangle = \\
&\langle\phi_1^S\,\bar{1}\,2\,\bar{2}\,|\overset{(1)}{\hat{H}^{SO}}|\bar{1}\,\bar{\phi}_1^T\,2\,\bar{2}\,\rangle + \langle\phi_1^S\,\bar{1}\,2\,\bar{2}\,|\overset{(2)}{\hat{H}^{SO}}|1\,\bar{1}\,\bar{2}\,\bar{\phi}_2^T\,\rangle + \\
&\langle 1\,\bar{\phi}_1^S\,2\,\bar{2}\,|\overset{(3)}{\hat{H}^{SO}}|\bar{1}\,\bar{\phi}_1^T\,2\,\bar{2}\,\rangle + \langle 1\,\bar{\phi}_1^S\,2\,\bar{2}\,|\overset{(4)}{\hat{H}^{SO}}|1\,\bar{1}\,\bar{2}\,\bar{\phi}_2^T\,\rangle + \\
&\langle 1\,\bar{1}\,\phi_2^S\,\bar{2}\,|\overset{(5)}{\hat{H}^{SO}}|\bar{1}\,\bar{\phi}_1^T\,2\,\bar{2}\,\rangle + \langle 1\,\bar{1}\,\phi_2^S\,\bar{2}\,|\overset{(6)}{\hat{H}^{SO}}|1\,\bar{1}\,\bar{2}\,\bar{\phi}_2^T\,\rangle + \\
&\langle 1\,\bar{1}\,2\,\bar{\phi}_2^S\,|\overset{(7)}{\hat{H}^{SO}}|\bar{1}\,\bar{\phi}_1^T\,2\,\bar{2}\,\rangle + \langle\,1\,\bar{1}\,2\,\bar{\phi}_2^S\,|\overset{(8)}{\hat{H}^{SO}}|1\,\bar{1}\,\bar{2}\,\bar{\phi}_2^T\,\rangle\,.
\end{aligned} \tag{C.8}$$

This there will be three cases in which the matrix elements are non vanishing. The first will occur when the two SDs are created by the same excitation but have different spins, as is the case of matrix element (1), for which we have

$$S_{ST=}\begin{pmatrix} 0 & 0 & 0 & 0 \\ 0 & 1 & 0 & 0 \\ 0 & 0 & 1 & 0 \\ 0 & 0 & 0 & 1 \end{pmatrix}. \tag{C.9}$$

This matrix has a row and a column of zeros. Therefore the only non-zero cofactor that can be generated is the one obtained by striking out the first line and the first column

$$(-1)^{1+1}\begin{vmatrix} \square & \square & \square & \square \\ \square & 1 & 0 & 0 \\ \square & 0 & 1 & 0 \\ \square & 0 & 0 & 1 \end{vmatrix} = \begin{vmatrix} 1 & 0 & 0 \\ 0 & 1 & 0 \\ 0 & 0 & 1 \end{vmatrix} = 1\,, \tag{C.10}$$

which leads to the result

$$(1) = \langle\phi_1^S|\hat{h}^{SO}|\bar{\phi_1}^T\rangle\,. \tag{C.11}$$

This case will also apply to matrix element (6),

$$(6) = (-1)^{3+3}\begin{vmatrix} 1 & 0 & 0 \\ 0 & 1 & 0 \\ 0 & 0 & 1 \end{vmatrix}\langle\phi_2^S|\hat{h}^{SO}|\bar{\phi_2}^T\rangle = \langle\phi_2^S|\hat{h}^{SO}|\bar{\phi_2}^T\rangle\,. \tag{C.12}$$

For the matrix elements (3) and (8) we have linear response orbitals that have been created by the same excitation and have the same spin. Therefore

$$(3) = \langle 1|\hat{h}^{SO}|\bar{1}\rangle(-1)^{1+2}\begin{vmatrix}\langle\phi_1^S|\phi_1^T\rangle & 0 & 0\\ 0 & 1 & 0\\ 0 & 0 & 1\end{vmatrix} = -\langle 1|\hat{h}^{SO}|\bar{1}\rangle\langle\phi_1^S|\phi_1^T\rangle \tag{C.13}$$

and

$$(8) = \langle 1|\hat{h}^{SO}|\bar{1}\rangle(-1)^{1+2}\begin{vmatrix}\langle\phi_1^S|\phi_1^T\rangle & 0 & 0\\ 0 & 1 & 0\\ 0 & 0 & 1\end{vmatrix} = -\langle 1|\hat{h}^{SO}|\bar{1}\rangle\langle\phi_1^S|\phi_1^T\rangle\,. \tag{C.14}$$

Finally, when the SDs are created by different excitations but the linear-response orbitals have the same spin, as in the cases of (4) and (7), we have

$$(4) = \langle 1|\hat{h}^{SO}|\bar{1}\rangle(-1)^{1+2}\begin{vmatrix}\langle\phi_1^S|\phi_1^T\rangle & 0 & 0\\ 0 & 1 & 0\\ 0 & 0 & 1\end{vmatrix} = -\langle 1|\hat{h}^{SO}|\bar{1}\rangle\langle\phi_1^S|\phi_1^T\rangle \tag{C.15}$$

and

$$(7) = \langle 1|\hat{h}^{SO}|\bar{1}\rangle(-1)^{1+2}\begin{vmatrix}\langle\phi_1^S|\phi_1^T\rangle & 0 & 0\\ 0 & 1 & 0\\ 0 & 0 & 1\end{vmatrix} = -\langle 1|\hat{h}^{SO}|\bar{1}\rangle\langle\phi_1^S|\phi_1^T\rangle\,. \tag{C.16}$$

Noticing that the matrix elements (2) and (5) are zero, we get to the final result

$$\begin{aligned}&\langle S_0^0|\hat{H}^{SO}|T^{-1}\rangle = \\ &-\langle 1|\hat{h}^{SO}|\bar{1}\rangle\langle\phi_1^S|\phi_1^T\rangle - \langle 2|\hat{h}^{SO}|\bar{2}\rangle\langle\phi_2^S|\phi_2^T\rangle\\ &-\langle 1|\hat{h}^{SO}|\bar{2}\rangle\langle\phi_2^S|\phi_1^T\rangle - \langle 2|\hat{h}^{SO}|\bar{1}\rangle\langle\phi_1^S|\phi_2^T\rangle\\ &+\langle\phi_1^S|\hat{h}^{SO}|\bar{\phi}_1^T\rangle + \langle\phi_2^S|\hat{h}^{SO}|\bar{\phi}_2^T\rangle\\ &+0+0\,.\end{aligned} \tag{C.17}$$

The same type of analysis can be applied to $\langle S_0^0|\hat{H}^{SO}|T^{+1}\rangle$, to give

$$\begin{aligned}&\langle S_0^0|\hat{H}^{SO}|T^{+1}\rangle = \\ &-\langle\bar{1}|\hat{h}^{SO}|1\rangle\langle\phi_1^S|\phi_1^T\rangle - \langle\bar{2}|\hat{h}^{SO}|2\rangle\langle\phi_2^S|\phi_2^T\rangle\\ &-\langle\bar{1}|\hat{h}^{SO}|2\rangle\langle\phi_2^S|\phi_1^T\rangle - \langle\bar{2}|\hat{h}^{SO}|1\rangle\langle\phi_1^S|\phi_2^T\rangle\\ &+\langle\bar{\phi_1^S}|\hat{h}^{SO}|\phi_1^T\rangle + \langle\bar{\phi_2^S}|\hat{h}^{SO}|\phi_2^T\rangle\\ &+0+0\,.\end{aligned} \tag{C.18}$$

Bibliography

[1] Basile F. E. Curchod and François P. Rotzinger. The cause for tremendous acceleration of chloride substitution via base catalysis in the chloro pentaammine cobalt(iii) ion. *Inorganic Chemistry*, 50(18):8728–8740, 2011.

[2] Andrew Gilbert and Jim Baggott. *Essentials of Molcular Photochemistry*. Blackwell Science, 1991.

[3] V. Ramamurthy Nicholas J. Turro and J.C. Scaiano. *Principles of Molecular Photochemistry. An Introduction*. University Science Books, 2009.

[4] M. A. Baldo, S. Lamansky, P. E. Burrows, M. E. Thompson, and S. R. Forrest. Very high-efficiency green organic light-emitting devices based on electrophosphorescence. *Applied Physics Letters*, 75(1):4–6, 1999.

[5] Andrew Gilbert and Jim Baggott. *Highly Efficient OLEDs with Phosphorescent Materials*. Wiley-VCH, 2008.

[6] Enrico Tapavicza, Ivano Tavernelli, and Ursula Rothlisberger. Trajectory surface hopping within linear response time-dependent density-functional theory. *Phys. Rev. Lett.*, 98:023001, Jan 2007.

[7] Ivano Tavernelli, Basile F. E. Curchod, and Ursula Rothlisberger. On nonadiabatic coupling vectors in time-dependent density functional theory. *The Journal of Chemical Physics*, 131(19):196101, 2009.

[8] Ivano Tavernelli, Enrico Tapavicza, and Ursula Rothlisberger. Nonadiabatic coupling vectors within linear response time-dependent density functional theory. *The Journal of Chemical Physics*, 130(12):124107, 2009.

[9] Ivano Tavernelli, Basile F. E. Curchod, Andrey Laktionov, and Ursula Rothlisberger. Nonadiabatic coupling vectors for excited states within time-dependent density functional theory in the tamm–dancoff approximation and beyond. *The Journal of Chemical Physics*, 133(19):194104, 2010.

[10] F. Franco de Carvalho, M.E.F. Bouduban, B.F.E. Curchod, and I. Tavernelli. Nonadiabatic molecular dynamics based on trajectories. *Entropy*, 16(1):62–85, 2013.

[11] Bernard Diu Claude Cohen-Tanoudji and Franck Laloe. *Mecanique Quantique*. Hermann Editeurs des Sciences et de Arts, 1973.

[12] R. Shankar. *Principles of Quantum Mechanics, 2nd Edition*. Blackwell Science, 1991.

[13] A. Abedi, N.T. Maitra, and E.K.U. Gross. Exact factorization of the time-dependent electron-nuclear wave function. *Phys. Rev. Lett.*, 105(12):123002, 2010.

[14] Ali Abedi, Neepa T. Maitra, and E. K. U. Gross. Correlated electron-nuclear dynamics: Exact factorization of the molecular wavefunction. *The Journal of Chemical Physics*, 137(22):22A530, 2012.

[15] P.R. Bunker. The electronic isotope shift in diatomic molecules and the partial breakdown of the born-oppenheimer approximation. *Journal of Molecular Spectroscopy*, 28(4):422 – 443, 1968.

[16] James O. Jensen and David R. Yarkony. On the evaluation of non-born–oppenheimer interactions for born–oppenheimer wave functions. v. a body fixed frame approach. applications to isotope effects on equilibrium geometries and the adiabatic correction for the $x^1\sigma+$ state of lih. *The Journal of Chemical Physics*, 89(2), 1988.

[17] Dominik Marx and Jürg Hutter. *Ab Initio Molecular Dyanmics*. Cambridge University Press, 2009.

[18] John C. Tully. Mixed quantum-classical dynamics. *Faraday Discuss.*, 110:407–419, 1998.

[19] Basile F. E. Curchod, Ursula Rothlisberger, and Ivano Tavernelli. Trajectory-based nonadiabatic dynamics with time-dependent density functional theory. *ChemPhysChem*, 14(7):1314–1340, 2013.

[20] David J. Tannor. *Introduction to Quantum Mechanics: A Time-Dependent Perspective*. University Science Books, 2006.

[21] Hans-Dieter Meyer, Fabien Gatti, and Graham Worth. *Multidimensional Quantum Dynamics*. Wiley-VCH, 2009.

[22] R. P. Feynman. Forces in molecules. *Phys. Rev.*, 56:340–343, Aug 1939.

[23] Hans Hellmann. *Einführung in die Quantenchemie*. Leipzig : F. Deuticke, 1937.

[24] John C. Tully and Richard K. Preston. Trajectory surface hopping approach to nonadiabatic molecular collisions: The reaction of H^+ with D_2. *J. Chem. Phys.*, 55(2):562–572, 1971.

[25] J. C. Tully. Molecular dynamics with electronic transitions. *J. Chem. Phys.*, 93:1061–1071, 1990.

[26] Basile F. E. Curchod and Ivano Tavernelli. On trajectory-based nonadiabatic dynamics: Bohmian dynamics versus trajectory surface hopping. *The Journal of Chemical Physics*, 138(18), 2013.

[27] Attila Szabo and Neil S. Ostlund. *Modern Quantum Chemistry*. Dover Publications, 1982.

[28] Robert G. Parr and Weitao Yang. *Density-Functional Theory of Atoms and Molecules*. Oxford Science Publications, 1982.

[29] P. Hohenberg and W. Kohn. Inhomogeneous electron gas. *Phys. Rev.*, 136:B864–B871, Nov 1964.

[30] L. H. Thomas. The calculation of atomic fields. *Mathematical Proceedings of the Cambridge Philosophical Society*, 23(5):542–548, 001 1927.

[31] S Lundqvist and N H March. *Theory of the Inhomogeneous Electron Gas*. Springer, Springer.

[32] W. Kohn and L. J. Sham. Self-consistent equations including exchange and correlation effects. *Phys. Rev.*, 140:1133, 1965.

[33] Kieron Burke. *The ABC of DFT*. http://dft.uci.edu/research.php, 2007.

[34] Erich Runge and E. K. U. Gross. Density-functional theory for time-dependent systems. *Phys. Rev. Lett.*, 52:997–1000, Mar 1984.

[35] Carsten A Ullrich. *Time-Dependent Density Functional Theory, Concepts and Applications*. Oxford Graduate Texts, 2012.

[36] Miguel A. L. Marques, Neepa T Maitra, Fernando M.S. Nogueira, Eberhard K.U. Gross, and Angel Rubio. *Fundamentals of Time-Dependent Density Functional Theory*. Springer, 2012.

[37] M. E. Casida. Time-dependent density-functional response theory for molecules. In D. P. Chong, editor, *Recent Advances in Density Functional Methods*, page 155. Singapore, World Scientific, 1995.

[38] I. E. Tamm L. I. Mandelshtam. The uncertainty relation between energy and time in nonrelativistic quantum mechanics. *J. Phys. (USSR)*, 9:449, 1945.

[39] S.M. Dancoff. Non-adiabatic meson theory of nuclear forces. *Phys. Rev.*, 78:382, 1950.

[40] So Hirata and Martin Head-Gordon. Time-dependent density functional theory within the tamm-dancoff approximation. *Chemical Physics Letters*, 314(3–4):291 – 299, 1999.

[41] Mark E. Casida. Time-dependent density-functional theory for molecules and molecular solids. *Journal of Molecular Structure: THEOCHEM*, 914(1–3):3 – 18, 2009. Time-dependent density-functional theory for molecules and molecular solids.

[42] Mark E. Casida, Fabien Gutierrez, Jingang Guan, Florent-Xavier Gadea, Dennis Salahub, and Jean-Pierre Daudey. Charge-transfer correction for improved time-dependent local density approximation excited-state potential energy curves: Analysis within the two-level model with illustration for H_2 and LiH. *The Journal of Chemical Physics*, 113(17), 2000.

[43] Michael J. G. Peach, Matthew J. Williamson, and David J. Tozer. Influence of triplet instabilities in tddft. *Journal of Chemical Theory and Computation*, 7(11):3578–3585, 2011. PMID: 26598256.

[44] Pekka Pyykkö. Relativistic effects in chemistry: More common than you thought. *Annual Review of Physical Chemistry*, 63(1):45–64, 2012.

[45] Kenneth G. Dyall and Jr. Knut Faegri. *Introduction to Relativistic Quantum Chemistry*. Oxford University Press, 2007.

[46] M. Reiher and A. Wolf. *Relativistic Quantum Chemistry*. Wiley-VCH, 2009.

[47] F. Franco de Carvalho and I. Tavernelli. Nonadiabatic dynamics with intersystem crossings: A time-dependent density functional theory implementation. *The Journal of Chemical Physics*, 143(22), 2015.

[48] Trond Saue. Relativistic hamiltonians for chemistry: A primer. *ChemPhysChem*, 12(17):3077–3094, 2011.

[49] Jochen Autschbach. Perspective: Relativistic effects. *The Journal of Chemical Physics*, 136(15):150902, 2012.

[50] Györgi Tarczay, Attila G. Császár, Wim Klopper, and Harry M. Quiney. Perspective: Relativistic effects. *The Journal of Chemical Physics*, 136(15):150902, 2012.

[51] A K Rajagopal. Inhomogeneous relativistic electron gas. *Journal of Physics C: Solid State Physics*, 11(24):L943, 1978.

[52] A H MacDonald and S H Vosko. A relativistic density functional formalism. *Journal of Physics C: Solid State Physics*, 12(15):2977, 1979.

[53] Fan Wang, Tom Ziegler, Erik van Lenthe, Stan van Gisbergen, and Evert Jan Baerends. The calculation of excitation energies based on the relativistic two-component zeroth-order regular approximation and time-dependent density-functional with full use of symmetry. *The Journal of Chemical Physics*, 122(20):204103, 2005.

[54] Fan Wang and Tom Ziegler. A simplified relativistic time-dependent density-functional theory formalism for the calculations of excitation energies including spin-orbit coupling effect. *The Journal of Chemical Physics*, 123(15):154102, 2005.

[55] Ivano Tavernelli, Enrico Tapavicza, and Ursula Rothlisberger. Non-adiabatic dynamics using time-dependent density functional theory: Assessing the coupling strengths. *Journal of Molecular Structure: {THEOCHEM}*, 914(1–3):22 – 29, 2009. Time-dependent density-functional theory for molecules and molecular solids.

[56] CPMD. Copyright IBM Corp 1990-2008, Copyright MPI für Festkörperforschung Stuttgart 1997-2001.

[57] Sandro G. Chiodo and Nino Russo. Dft spin–orbit coupling between singlet and triplet excited states: A case of psoralen compounds. *Chemical Physics Letters*, 490(1–3):90 – 96, 2010.

[58] Qi Ou and Joseph E. Subotnik. Electronic relaxation in benzaldehyde evaluated via td-dft and localized diabatization: Intersystem crossings, conical intersections, and phosphorescence. *The Journal of Physical Chemistry C*, 117(39):19839–19849, 2013.

[59] R. Sternheimer. On nuclear quadrupole moments. *Phys. Rev.*, 84(2):244–253, 1951.

[60] Jurg Hutter. Excited state nuclear forces from the tamm–dancoff approximation to time-dependent density functional theory within the plane wave basis set framework. *The Journal of Chemical Physics*, 118(9):3928–3934, 2003.

[61] Giovanni Granucci, Maurizio Persico, and Gloria Spighi. Surface hopping trajectory simulations with spin-orbit and dynamical couplings. *The Journal of Chemical Physics*, 137(22):22A501, 2012.

[62] Philipp Marquetand, Martin Richter, Jesus Gonzalez-Vazquez, Ignacio Sola, and Leticia Gonzalez. Nonadiabatic ab initio molecular dynamics including spin-orbit coupling and laser fields. *Faraday Discuss.*, 153:261–273, 2011.

[63] A. K. Rajagopal and J. Callaway. Inhomogeneous electron gas. *Phys. Rev. B*, 7:1912, 1973.

[64] R. M. Dreizler and E. K. U. Gross. *Density Functional Theory*. Springer, Berlin, 1990.

[65] U von Barth and L Hedin. A local exchange-correlation potential for the spin polarized case. i. *Journal of Physics C: Solid State Physics*, 5(13):1629, 1972.

[66] O. Gunnarsson and B. I. Lundqvist. Exchange and correlation in atoms, molecules, and solids by the spin-density-functional formalism. *Phys. Rev. B*, 13:4274–4298, May 1976.

[67] Yihan Shao, Martin Head-Gordon, and Anna I. Krylov. The spin-flip approach within time-dependent density functional theory: Theory and applications to diradicals. *The Journal of Chemical Physics*, 118(11), 2003.

[68] Fan Wang and Tom Ziegler. Time-dependent density functional theory based on a noncollinear formulation of the exchange-correlation potential. *The Journal of Chemical Physics*, 121(24):12191–12196, 2004.

[69] Fan Wang and Tom Ziegler. The performance of time-dependent density functional theory based on a noncollinear exchange-correlation potential in the calculations of excitation energies. *The Journal of Chemical Physics*, 122(7), 2005.

[70] R. McWeeny. *Methods of Molecular Quantum Chemistry*. Academic Press, 1969.

[71] Per-Olov Löwdin. Quantum theory of many-particle systems. i. physical interpretations by means of density matrices, natural spin-orbitals, and convergence problems in the method of configurational interaction. *Phys. Rev.*, 97:1474–1489, Mar 1955.

[72] Daniel Sebastiani and Michele Parrinello. A new ab-initio approach for nmr chemical shifts in periodic systems. *The Journal of Physical Chemistry A*, 105(10):1951–1958, 2001.

[73] M. A. El-Sayed. Spin—orbit coupling and the radiationless processes in nitrogen heterocyclics. *The Journal of Chemical Physics*, 38(12), 1963.

[74] Michael W. Schmidt, Kim K. Baldridge, Jerry A. Boatz, Steven T. Elbert, Mark S. Gordon, Jan H. Jensen, Shiro Koseki, Nikita Matsunaga, Kiet A. Nguyen, Shujun Su, Theresa L. Windus, Michel Dupuis, and John A. Montgomery. General atomic and molecular electronic structure system. *Journal of Computational Chemistry*, 14(11):1347–1363, 1993.

[75] N. Troullier and José Luís Martins. Efficient pseudopotentials for plane-wave calculations. ii. operators for fast iterative diagonalization. *Phys. Rev. B*, 43:8861–8869, Apr 1991.

[76] Shiro Koseki, Mark S. Gordon, Michael W. Schmidt, and Nikita Matsunaga. Main group effective nuclear charges for spin-orbit calculations. *The Journal of Physical Chemistry*, 99(34):12764–12772, 1995.

[77] C. M. Marian. *Berechnung von Matrixelementen des Spin-Bahn- und Spin-Spin-Kopplungsoperators mit MRD-CI-Wellenfunktionen*. Doctoral Thesis, University of Bonn. 1981.

[78] Yoon S. Lee, Walter C. Ermler, and Kenneth S. Pitzer. Abinitio effective core potentials including relativistic effects. i. formalism and applications to the xe and au atoms. *The Journal of Chemical Physics*, 67(12), 1977.

[79] P Hafner and W H E Schwarz. Pseudo-potential approach including relativistic effects. *Journal of Physics B: Atomic and Molecular Physics*, 11(2):217, 1978.

[80] Christian Teichteil, Michel Pelissier, and Fernand Spiegelmann. Ab initio molecular calculations including spin-orbit coupling. i. method and atomic tests. *Chemical Physics*, 81(3):273 – 282, 1983.

[81] ADF. ADF2013, SCM, Theoretical Chemistry, Vrije Universiteit, Amsterdam, The Netherlands.

[82] Martin Richter, Philipp Marquetand, Jesús González-Vázquez, Ignacio Sola, and Leticia González. SHARC: ab InitioMolecular Dynamics with Surface Hopping in the Adiabatic Representation Including Arbitrary Couplings. *Journal of Chemical Theory and Computation*, 7(5):1253–1258, May 2011.

[83] Basile F. E. Curchod, Ivano Tavernelli, and Ursula Rothlisberger. Trajectory-based solution of the nonadiabatic quantum dynamics equations: an on-the-fly approach for molecular dynamics simulations. *Phys. Chem. Chem. Phys.*, 13:3231–3236, 2011.

[84] Basile F. E. Curchod, Ursula Rothlisberger, and Ivano Tavernelli. Trajectory-based nonadiabatic dynamics with time-dependent density functional theory. *ChemPhysChem*, 14(7):1314–1340, 2013.

[85] N. Troullier and J. L. Martins. Efficient pseudopotentials for plane-wave calculations. *Phys. Rev. B*, 43:1993–2006, 1991.

[86] M. J. Frisch, G. W. Trucks, H. B. Schlegel, G. E. Scuseria, M. A. Robb, J. R. Cheeseman, G. Scalmani, V. Barone, B. Mennucci, G. A. Petersson, H. Nakatsuji, M. Caricato, X. Li, H. P. Hratchian, A. F. Izmaylov, J. Bloino, G. Zheng, J. L. Sonnenberg, M. Hada, M. Ehara, K. Toyota, R. Fukuda, J. Hasegawa, M. Ishida, T. Nakajima, Y. Honda, O. Kitao, H. Nakai, T. Vreven, J. A. Montgomery, Jr., J. E. Peralta, F. Ogliaro, M. Bearpark, J. J. Heyd, E. Brothers, K. N. Kudin, V. N. Staroverov, R. Kobayashi, J. Normand, K. Raghavachari, A. Rendell, J. C. Burant, S. S. Iyengar, J. Tomasi, M. Cossi, N. Rega, J. M. Millam, M. Klene, J. E. Knox, J. B. Cross, V. Bakken, C. Adamo, J. Jaramillo, R. Gomperts, R. E. Stratmann, O. Yazyev, A. J. Austin, R. Cammi, C. Pomelli, J. W. Ochterski, R. L. Martin, K. Morokuma, V. G. Zakrzewski, G. A. Voth, P. Salvador, J. J. Dannenberg, S. Dapprich, A. D. Daniels, O. Farkas, J. B. Foresman, J. V. Ortiz, J. Cioslowski, and D. J. Fox. Gaussian 09 Revision A.1. Gaussian Inc. Wallingford CT 2009.

[87] T. H. Jr. Dunning. Gaussian basis sets for use in correlated molecular calculations. i. the atoms boron through neon and hydrogen. *J. Chem. Phys.*, 90:1007, 1989.

[88] Haruyuki Nakano. Quasidegenerate perturbation theory with multiconfigurational self-consistent-field reference functions. *The Journal of Chemical Physics*, 99(10), 1993.

[89] Dmitri G. Fedorov and James P. Finley. Spin-orbit multireference multistate perturbation theory. *Phys. Rev. A*, 64:042502, Sep 2001.

[90] M A Baldo, D F O'Brien, Y You, A Shoustikov, S Sibley, M E Thompson, and S R Forrest. Highly efficient phosphorescent emission from organic electroluminescent devices. *Nature*, 395(6698):151–154, 1998.

[91] M A Baldo, S Lamansky, P E Burrows, M E Thompson, and S R Forrest. Very high-efficiency green organic light-emitting devices based on electrophosphorescence. *Applied Physics Letters*, 75(1):4–6, July 1999.

[92] Lucilla Favero, Giovanni Granucci, and Maurizio Persico. Dynamics of acetone photodissociation: a surface hopping study. *Phys. Chem. Chem. Phys.*, 15:20651–20661, 2013.

[93] Karunamoy Rajak and Biswajit Maiti. Trajectory surface hopping study of the $O(3P) + C_2H_2$ reaction dynamics: Effect of collision energy on the extent of intersystem crossing. *The Journal of Chemical Physics*, 140(4):–, 2014.

[94] Sebastian Mai, Philipp Marquetand, and Leticia González. A general method to describe intersystem crossing dynamics in trajectory surface hopping. *International Journal of Quantum Chemistry*, 115(18):1215–1231, 2015.

[95] Ganglong Cui and Walter Thiel. Generalized trajectory surface-hopping method for internal conversion and intersystem crossing. *The Journal of Chemical Physics*, 141(12):–, 2014.

[96] G. Capano, M. Chergui, U. Rothlisberger, I. Tavernelli, and T. J. Penfold. A quantum dynamics study of the ultrafast relaxation in a prototypical Cu(I)–phenanthroline. *The Journal of Physical Chemistry A*, 118(42):9861–9869, 2014. PMID: 25275666.

[97] T.J. Penfold and G.A. Worth. The effect of molecular distortions on spin–orbit coupling in simple hydrocarbons. *Chemical Physics*, 375(1):58 – 66, 2010.

[98] Changjian Xie, Xixi Hu, Linsen Zhou, Daiqian Xie, and Hua Guo. Ab initio determination of potential energy surfaces for the first two uv absorption bands of so2. *The Journal of Chemical Physics*, 139(1):–, 2013.

[99] A. Laio, J. VandeVondele, and U. Rothlisberger. D-resp: Dynamically generated electrostatic potential derived charges from quantum mechanics/molecular mechanics simulations. *Journal of Physical Chemistry B*, 106(29):7300–7307, 2002.

[100] A. Laio, J. VandeVondele, and U. Rothlisberger. A hamiltonian electrostatic coupling scheme for hybrid car-parrinello molecular dynamics simulations. *Journal of Chemical Physics*, 116(16):6941–6947, 2002.

[101] Iain Wilkinson, Andrey E. Boguslavskiy, Jochen Mikosch, Julien B. Bertrand, Hans Jakob Wörner, David M. Villeneuve, Michael Spanner, Serguei Patchkovskii, and Albert Stolow. Excited state dynamics in SO_2. i. bound state relaxation studied by time-resolved photoelectron-photoion coincidence spectroscopy. *The Journal of Chemical Physics*, 140(20):–, 2014.

[102] Sebastian Mai, Philipp Marquetand, and Leticia Gonzalez. Non-adiabatic and intersystem crossing dynamics in SO_2. ii. the role of triplet states in the bound state dynamics studied by surface-hopping simulations. *The Journal of Chemical Physics*, 140(20):–, 2014.

[103] C Lévêque, D Peláez, H Köppel, and R Taïeb. Direct observation of spin-forbidden transitions through the use of suitably polarized light. *Nature communications*, 2014.

[104] M. Ben-Nun and Todd J. Martinez. Nonadiabatic molecular dynamics: Validation of the multiple spawning method for a multidimensional problem. *The Journal of Chemical Physics*, 108(17):7244–7257, 1998.

[105] I. Tavernelli, U.F. Röhrig, and U. Rothlisberger. Molecular dynamics in electronically excited states using time-dependent density functional theory. *Mol. Phys.*, 103(6-8):963–981, 2005.

[106] I. Tavernelli. Electronic density response of liquid water using time-dependent density functional theory. *Phys. Rev. B*, 73:094204, 2006.

[107] Martin Richter, Philipp Marquetand, Jesus Gonzalez-Vazquez, Ignacio Sola, and Leticia Gonzalez. Femtosecond intersystem crossing in the dna nucleobase cytosine. *The Journal of Physical Chemistry Letters*, 3(21):3090–3095, 2012.

[108] L. Freitag and L. Gonzalez. Theoretical spectroscopy and photodynamics of a ruthenium nitrosyl complex. *Inorg. Chem.*, 53:6415–6426, 2014.

[109] E. van Lenthe, E. J. Baerends, and J. G. Snijders. Relativistic regular two-component hamiltonians. *The Journal of Chemical Physics*, 99(6):4597–4610, 1993.

[110] L.D. Landau. A theory of energy transfer on collisions. *Phys. Z. Sowjetunion*, 2:46, 1932.

[111] Clarence Zener. Non-adiabatic crossing of energy levels. *Proceedings of the Royal Society of London A: Mathematical, Physical and Engineering Sciences*, 137(833):696–702, 1932.

[112] T. Navaneeth Rao, Susan S. Collier, and Jack G. Calvert. Primary photophysical processes in the photochemistry of sulfur dioxide at 2875 a. *Journal of the American Chemical Society*, 91(7):1609–1615, 1969.

[113] J. P. Perdew, K. Burke, and M. Ernzerhof. Generalized gradient approximation made simple. *Phys. Rev. Lett.*, 77:3865–3868, 1996.

[114] Glenn J. Martyna and Mark E. Tuckerman. A reciprocal space based method for treating long range interactions in ab initio and force-field-based calculations in clusters. *The Journal of Chemical Physics*, 110(6):2810–2821, 1999.

[115] M. A. L. Marques and E. K. U. Gross. Time-dependent density functional theory. *Lect. Notes. Phys.*, 620:144–184, 2003.

[116] Junmei Wang, Romain M. Wolf, James W. Caldwell, Peter A. Kollman, and David A. Case. Development and testing of a general amber force field. *Journal of Computational Chemistry*, 25(9):1157–1174, 2004.

[117] Michael H. Palmer, David A. Shaw, and Martyn F. Guest. The electronically excited and ionic states of sulphur dioxide: an ab initio molecular orbital ci study and comparison with spectral data. *Molecular Physics*, 103(6-8):1183–1200, 2005.

[118] Sebastian Mai. *The Role of Triplet States in the Excited States Dynamics of Sulphur Dioxide*. PhD thesis, University of Jena, 2012.

[119] Ching-Chi Zen, I-Chia Chen, Yuan-Pern Lee, and A. J. Merer. Laser-induced phosphorescence of so2 in solid neon:a direct observation of the $\tilde{b}^3a_2$ state in the $^{16}OS^{18}O$molecule. *The Journal of Physical Chemistry A*, 104(4):771–776, 2000.

[120] Julian Heicklen, Nelson Kelly, and Kenneth Partymiller. The photophysics and photochemistry of so2. *Reviews of Chemical Intermediates*, 3(3-4):315–404, 1980.

[121] John P. Perdew and Karla Schmidt. Jacob's ladder of density functional approximations for the exchange-correlation energy. *AIP Conference Proceedings*, 577(1):1–20, 2001.

[122] Hajime Watanabe, Soji Tsuchiya, and Seiichiro Koda. Rotation-dependent intramolecular processes of so2(a1a2) in a supersonic jet. *Faraday Discuss. Chem. Soc.*, 75:365–376, 1983.

[123] Hajime Watanabe, Soji Tsuchiya, and Seiichiro Koda. Quantum beats in the fluorescence of jet-cooled sulfur dioxide(ã 1a2) under a weak magnetic field. *The Journal of Physical Chemistry*, 87(6):906–908, 1983.

[124] Hajime Watanabe, Soji Tsuchiya, and Seiichiro Koda. Zeeman quantum beat spectroscopy applied to the $\tilde{A}^1a_2 - \tilde{X}^1\ a_1$ transition of so2. *The Journal of Chemical Physics*, 82(12):5310–5317, 1985.

[125] R. Kullmer and W. Demtröder. Subdoppler laser spectroscopy of so2 in a supersonic beam. *The Journal of Chemical Physics*, 81(7):2919–2924, 1984.

[126] Hanjun Sun, Li Wu, Weili Wei, and Xiaogang Qu. Recent advances in graphene quantum dots for sensing. *Materials Today*, 16(11):433 – 442, 2013.

[127] Xiaoming Li, Muchen Rui, Jizhong Song, Zihan Shen, and Haibo Zeng. Carbon and graphene quantum dots for optoelectronic and energy devices: A review. *Advanced Functional Materials*, 25(31):4929–4947, 2015.

[128] Mallory L. Mueller, Xin Yan, John A. McGuire, and Liang shi Li. Triplet states and electronic relaxation in photoexcited graphene quantum dots. *Nano Letters*, 10(7):2679–2682, 2010. PMID: 20575573.

[129] Liang shi Li and Xin Yan. Colloidal graphene quantum dots. *The Journal of Physical Chemistry Letters*, 1(17):2572–2576, 2010.

[130] Oleg V. Yazyev, Ivano Tavernelli, Ursula Rothlisberger, and Lothar Helm. Early stages of radiation damage in graphite and carbon nanostructures: A first-principles molecular dynamics study. *Phys. Rev. B*, 75:115418, Mar 2007.

[131] L. Britnell, R. V. Gorbachev, R. Jalil, B. D. Belle, F. Schedin, A. Mishchenko, T. Georgiou, M. I. Katsnelson, L. Eaves, S. V. Morozov, N. M. R. Peres, J. Leist, A. K. Geim, K. S. Novoselov, and L. A. Ponomarenko. Field-effect tunneling transistor based on vertical graphene heterostructures. *Science*, 335(6071):947–950, 2012.

[132] F. Bonaccorso, Z. Sun, T. Hasan, and A. C. Ferrari. Graphene photonics and optoelectronics. *Nat Photon*, 4(9):611–622, 09 2010.

[133] Philipp Wagner, Christopher P. Ewels, Viktoria V. Ivanovskaya, Patrick R. Briddon, Amand Pateau, and Bernard Humbert. Ripple edge engineering of graphene nanoribbons. *Phys. Rev. B*, 84:134110, Oct 2011.

[134] Caterina Cocchi, Deborah Prezzi, Alice Ruini, Marilia J. Caldas, and Elisa Molinari. Optical properties and charge-transfer excitations in edge-functionalized all-graphene nanojunctions. *The Journal of Physical Chemistry Letters*, 2(11):1315–1319, 2011. PMID: 26295427.

[135] Joost de Graaf, René van Roij, and Marjolein Dijkstra. Dense regular packings of irregular nonconvex particles. *Phys. Rev. Lett.*, 107:155501, Oct 2011.

[136] R. Martel, V. Derycke, C. Lavoie, J. Appenzeller, K. K. Chan, J. Tersoff, and Ph. Avouris. Ambipolar electrical transport in semiconducting single-wall carbon nanotubes. *Phys. Rev. Lett.*, 87:256805, Dec 2001.

[137] H. Kataura, Y. Kumazawa, Y. Maniwa, I. Umezu, S. Suzuki, Y. Ohtsuka, and Y. Achiba. Optical properties of single-wall carbon nanotubes. *Synthetic Metals*, 103(1–3):2555 – 2558, 1999. International Conference on Science and Technology of Synthetic Metals.

[138] Caterina Cocchi, Alice Ruini, Deborah Prezzi, Marilia J. Caldas, and Elisa Molinari. Designing all-graphene nanojunctions by covalent functionalization. *The Journal of Physical Chemistry C*, 115(7):2969–2973, 2011.

[139] Kyoko Nakada, Mitsutaka Fujita, Gene Dresselhaus, and Mildred S. Dresselhaus. Edge state in graphene ribbons: Nanometer size effect and edge shape dependence. *Phys. Rev. B*, 54:17954–17961, Dec 1996.

[140] Veronica Barone, Oded Hod, , and Gustavo E. Scuseria. Electronic structure and stability of semiconducting graphene nanoribbons. *Nano Letters*, 6(12):2748–2754, 2006. PMID: 17163699.

[141] C. L. Kane and E. J. Mele. Quantum spin hall effect in graphene. *Phys. Rev. Lett.*, 95:226801, Nov 2005.

[142] J. C. Boettger and S. B. Trickey. First-principles calculation of the spin-orbit splitting in graphene. *Phys. Rev. B*, 75:121402, Mar 2007.

[143] Yugui Yao, Fei Ye, Xiao-Liang Qi, Shou-Cheng Zhang, and Zhong Fang. Spin-orbit gap of graphene: First-principles calculations. *Phys. Rev. B*, 75:041401, Jan 2007.

[144] Hongki Min, J. E. Hill, N. A. Sinitsyn, B. R. Sahu, Leonard Kleinman, and A. H. MacDonald. Intrinsic and rashba spin-orbit interactions in graphene sheets. *Phys. Rev. B*, 74:165310, Oct 2006.

[145] P. López-Tarifa, M.-A. H. du Penhoat, R. Vuilleumier, M.-P. Gaigeot, I. Tavernelli, A. Le Padellec, J.-P. Champeaux, M. Alcamí, P. Moretto-Capelle, F. Martín, and Politis M. F. Ultrafast nonadiabatic fragmentation dynamics of doubly charged uracil in a gas phase. *Phys. Rev. Lett.*, 107(2):023202, 2011.

[146] M.-E. Moret, I. Tavernelli, M. Chergui, and U. Rothlisberger. Electron localization dynamics in the triplet excited state of $[Ru(bpy)_3]^{2+}$ in aqueous solution. *Chemistry-A European Journal*, 16(20):5889–5894, 2010.

[147] M. Micciarelli, M. Valadan, B. Della Ventura, G. Di Fabio, L. De Napoli, S. Bonella, U. Rothlisberger, I. Tavernelli, C. Altucci, and R. Velotta. Photophysics and photochemistry of a DNA-protein cross-linking model: A synergistic approach combining experiments and theory. *J. Phys. Chem. B*, 118(19):4983–4992, 2014.

[148] Ado Jorio, Gene Dresselhaus, and Mildred Dresselhaus. *Carbon Nanotubes*, volume 111 of *Topics in Applied Physics*. Springer Verlag, 2008.

[149] A. H. Castro Neto, F. Guinea, N. M. R. Peres, K. S. Novoselov, and A. K. Geim. The electronic properties of graphene. *Rev. Mod. Phys.*, 81:109–162, Jan 2009.

[150] G. Dresselhaus and M. S. Dresselhaus. Spin-orbit interaction in graphite. *Phys. Rev.*, 140:A401–A412, Oct 1965.

[151] J Serrano, M Cardona, and T Ruf. Spin-orbit splitting in diamond: excitons and acceptor related states. *Solid State Communications*, 113(7):411 – 414, 2000.

[152] R. Saito, G. Dresselhaus, and M.S. Dresselhaus. *Physical Properties of Carbon Nanotubes*. Imperial College Press, 1998.

[153] Daniel Huertas-Hernando, F. Guinea, and Arne Brataas. Spin-orbit coupling in curved graphene, fullerenes, nanotubes, and nanotube caps. *Phys. Rev. B*, 74:155426, Oct 2006.

[154] A. Loiseau, P. Launois, P. Petit, S. Roche, and J.-P. Salvetat. *Understanding Carbon Nanotubes*, volume 677 of *Lecture Notes in Physics*. Springer Verlag, 2006.

[155] S. Reich, C. Thomsen, and J. Maultzsch. *Carbon Nanotubes*. Wiley-VCH, 2004.

[156] Takashi Yumura, Daijiro Nozaki, Kaori Hirahara, Shunji Bandow, Sumio Iijima, and Kazunari Yoshizawa. Quantum-size effects in capped and uncapped carbon nanotubes. *Annu. Rep. Prog. Chem., Sect. C: Phys. Chem.*, 102:71–91, 2006.

[157] L. Chico, Vincent H. Crespi, Lorin X. Benedict, Steven G. Louie, and Marvin L. Cohen. Pure carbon nanoscale devices: Nanotube heterojunctions. *Phys. Rev. Lett.*, 76:971–974, Feb 1996.

[158] X. Blase, Lorin X. Benedict, Eric L. Shirley, and Steven G. Louie. Hybridization effects and metallicity in small radius carbon nanotubes. *Phys. Rev. Lett.*, 72:1878–1881, Mar 1994.

[159] Felipe Franco de Carvalho, Basile F. E. Curchod, Thomas J. Penfold, and Ivano Tavernelli. Derivation of spin-orbit couplings in collinear linear-response tddft: A rigorous formulation. *The Journal of Chemical Physics*, 140(14):144103, 2014.

[160] G. A. Jones, B. K. Carpenter, and M.N. Paddon-Row. Application of trajectory surface hopping to the study of a symmetry-forbidden intramolecular hole transfer process in bismethyleneadamantane cation radical. *J. Am. Chem. Soc*, 120:5499–5508, 1990.

[161] E. Tapavicza, I. Tavernelli, and U. Rothlisberger. Ab initio excited state properties and dynamics of a prototype σ-Bridged-Donor-Acceptor molecule. *J. Phys. Chem. A*, 113(35):9595–9602, 2009.

[162] Eric Jones, Travis Oliphant, Pearu Peterson, et al. SciPy: Open source scientific tools for Python, 2001–. [Online; accessed 2016-09-21].

[163] I. Tavernelli, B.F.E. Curchod, and U. Rothlisberger. Nonadiabatic molecular dynamics with solvent effects: A LR-TDDFT QM/MM study of Ruthenium (II) tris(bipyridine) in water. *Chem. Phys.*, 391(1):101–109, 2011.

[164] G. Capano, U. Rothlisberger, I. Tavernelli, and T. J. Penfold. Theoretical rationalization of the emission properties of prototypical Cu (I)-Phenanthroline complexes. *J. Phys. Chem. A*, 119(27):7026–7037, 2015.

[165] I. Tavernelli. Nonadiabatic molecular dynamics simulations: Synergies between theory and experiments. *Acc. Chem. Res.*, 48(3):792–800, 2015.

[166] Kerstin Andersson, Per-Åke Malmqvist, and Björn O. Roos. Second-order perturbation theory with a complete active space self-consistent field reference function. *The Journal of Chemical Physics*, 96(2), 1992.

[167] R. O. Jones. Density functional theory: Its origins, rise to prominence, and future. *Rev. Mod. Phys.*, 87:897–923, Aug 2015.

[168] Rustam Z. Khaliullin, Joost VandeVondele, and Jürg Hutter. Efficient linear-scaling density functional theory for molecular systems. *Journal of Chemical Theory and Computation*, 9(10):4421–4427, 2013. PMID: 26589159.

[169] Miquel Huix-Rotllant, Bhaarathi Natarajan, Andrei Ipatov, C. Muhavini Wawire, Thierry Deutsch, and Mark E. Casida. Assessment of noncollinear spin-flip tamm-dancoff approximation time-dependent density-functional theory for the photochemical ring-opening of oxirane. *Phys. Chem. Chem. Phys.*, 12:12811–12825, 2010.

[170] Yan Zhao and Donald G. Truhlar. The m06 suite of density functionals for main group thermochemistry, thermochemical kinetics, noncovalent interactions, excited states, and transition elements: two new functionals and systematic testing of four m06-class functionals and 12 other functionals. *Theoretical Chemistry Accounts*, 120(1):215–241, 2008.

[171] Takeshi Yanai, David P Tew, and Nicholas C Handy. A new hybrid exchange–correlation functional using the coulomb-attenuating method (cam-b3lyp). *Chemical Physics Letters*, 393(1–3):51 – 57, 2004.

[172] Fan Wang and Tom Ziegler. Use of noncollinear exchange-correlation potentials in multiplet resolutions by time-dependent density functional theory. *International Journal of Quantum Chemistry*, 106(12):2545–2550, 2006.

[173] Yasuteru Shigeta, Kimihiko Hirao, and So Hirata. Exact-exchange time-dependent density-functional theory with the frequency-dependent kernel. *Phys. Rev. A*, 73:010502, Jan 2006.

[174] Neepa T. Maitra. Undoing static correlation: Long-range charge transfer in time-dependent density-functional theory. *The Journal of Chemical Physics*, 122(23), 2005.

[175] Neepa T. Maitra, Fan Zhang, Robert J. Cave, and Kieron Burke. Double excitations within time-dependent density functional theory linear response. *The Journal of Chemical Physics*, 120(13), 2004.

[176] M. Petersilka, U. J. Gossmann, and E. K. U. Gross. Excitation energies from time-dependent density-functional theory. *Phys. Rev. Lett.*, 76:1212–1215, Feb 1996.

[177] Oleg Gritsenko and Evert Jan Baerends. Asymptotic correction of the exchange–correlation kernel of time-dependent density functional theory for long-range charge-transfer excitations. *The Journal of Chemical Physics*, 121(2), 2004.

[178] David J. Tozer. Relationship between long-range charge-transfer excitation energy error and integer discontinuity in kohn–sham theory. *The Journal of Chemical Physics*, 119(24), 2003.

[179] R.E. Moss. *Advance Molecular Quantum Mechanics*. Chapman and Hall, London, 1973.

Felipe Miraglia Franco de Carvalho

Education

2012–present **PhD in Theoretical Chemistry**, *EPFL*, Lausanne, Switzerland.

2010–2012 **MSc in Chemistry**, *EPFL*, Lausanne, Switzerland.

2007–2010 **BSc in Chemistry and Chemical Engineering**, *EPFL*, Lausanne, Switzerland.

Languages

English	Fluent
Portuguese	Fluent
French	Fluent
Italian	Fluent
Spanish	Fluent
German	Basic

Computer Skills

Programming	Fortran, C, shell scripting, Python
Chemistry programs	GAMESS, CPMD, Gaussian, ADF
Tools	Matplotlib, gnuplot, LaTeX
Operating Systems	GNU/Linux, Windows,Mac OS

Publications

1. Felipe Franco de Carvalho, Marine EF Bouduban, Basile FE Curchod, Ivano Tavernelli. Entropy **16**, 62-85
2. Felipe Franco De Carvalho, Basile FE Curchod, Thomas J Penfold, Ivano Tavernelli. Derivation of Spin-orbit Couplings in Collinear Linear-response TDDFT: A Rigorous Formulation. The Journal of Chemical Physics **140**, 144103.
3. Felipe Franco de Carvalho, Ivano Tavernelli. Nonadiabatic Dynamics with Intersystem Crossings: A Time-dependent Density Functional Theory Implementation. Journal of Chemical Physics **143**, 224105

Organized Conference

2014 **Co-organizer, CECAM Workshop**, *Recent progress in adiabatic and non-adiabatic methods in quantum dynamics*, CECAM,Lausanne, Switzerland.

Atended

2012 **CECAM Workshop**, *High-dimensional Quantum Dynamics: Challenges and Opportunities*, University of Birmingham, United Kingdom.

felipe.mfdecarvalho@gmail.com

2014 **School**, *6th Time-Dependent Density-Functional Theory: Prospects and Applications*, Centro de Ciencias de Benasque Pedro Pascual, Spain.

✉ *felipe.mfdecarvalho@gmail.com*